Theoretical Analysis and Numerical Simulation of Attosecond Time Delays in Photoionization

by

Jing Su

B.S., University of Science and Technology of China, 2008

M.S., University of Colorado at Boulder, 2013

A thesis submitted to the

Faculty of the Graduate School of the

University of Colorado in partial fulfillment

of the requirements for the degree of

Doctor of Philosophy

Department of Physics

2014

This thesis entitled:
Theoretical Analysis and Numerical Simulation of Attosecond Time Delays in Photoionization
written by Jing Su
has been approved for the Department of Physics

_____

Prof. Andreas Becker

_____

Dr. Agnieszka Jaroń-Becker

Date _____

The final copy of this thesis has been examined by the signatories, and we find that both the content and the form meet acceptable presentation standards of scholarly work in the above mentioned discipline.

Su, Jing (Ph.D., Physics)

Theoretical Analysis and Numerical Simulation of Attosecond Time Delays in Photoionization

Thesis directed by Prof. Andreas Becker

Recent developments in laser technology, in particular the advances in high-harmonic generation, enable the generation of ultrashort extreme ultraviolet (XUV) pulses with attosecond (1 as = 10^{-18} s) duration. Such tools open the opportunity to study electron dynamics in atoms and molecules on its intrinsic time scale. As an example, the attosecond streaking technique was recently applied to time resolve the photoionization process in atomic and solid systems. In this technique, an isolated attosecond XUV pulse, that ionizes the electron in the target system, is superimposed with a few-cycle streaking pulse (usually of near-infrared wavelengths). The streaking pulse modulates the final momentum (or energy) of the photoelectron. The measured streaking trace, i.e., the final momentum (or energy) as a function of the relative delay between these two pulses, contains time information of the photoionization process. By comparing two streaking traces measured for photoionization from the 2s and 2p orbitals in a neon atom, Schultze *et al.* [Science **328**, 1658 (2010)] found a temporal offset of 21 ± 5 as between them and interpreted this value as the time delay between photoionization from the 2s and 2p orbitals. This experiment has initiated a debate among theoreticians, in particular about the origin of the measured time delay. A correct interpretation of the delay is extremely important for our understanding of the attosecond streaking technique and an exact analysis of time resolved measurements of this and other ultrafast processes.

In this thesis we systematically study the attosecond time delays in photoionization using numerical simulations. We first propose a new method, based on the fundamental definition of a time delay, to theoretically study the photoionization process induced by an XUV pulse from a time-dependent perspective. We then turn to analyze the time delays measured in streaking experiments. Our results show that for single-photon ionization the observed streaking time delay arises from

the finite-range propagation of the photoelectron in the coupled field of the ionic potential and the streaking pulse. Consequently, we conclude that the photon absorption occurs instantaneously at the center of the XUV pulse, i.e., with no time delay. Our analysis further reveals that the streaking time delay can be interpreted as a finite sum of piecewise field-free time delays weighted by the relative instantaneous streaking field strength and provides itself as a useful tool for imaging the presence of an additional potential located at a distance from the ionic core. We finally extend our time delay studies to the two-photon ionization process and show that the absorption time delay is significantly different for nonresonant and resonant two-photon ionization. Our results imply that the absorption of two photons in the nonresonant case occurs instantaneously, without time delay, at the center of the XUV pulse. However, in the resonant scenario we find a substantial absorption time delay that changes linearly with the duration of the XUV pulse. Our further theoretical analysis shows that this absorption time delay can be related to the phase acquired by the electron during its transition from the initial ground state to the continuum.

Dedication

To my love and family

Acknowledgements

First and foremost, I would like to thank my advisor Prof. Andreas Becker for his continuous support and help in the last five years. Without his guidance and encouragement I would have no chance to finish my Ph.D. work. A lot of times when I met challenges and problems in our project and did not have confidence about it, he taught and encouraged me with his patience, motivation, enthusiasm, and immense knowledge. He is a very nice and easygoing person, however with very rigorous attitude towards science. I have really learned a lot from him in these years, in particular, the ability of critical thinking and the way of presenting results with logic, which will help me throughout my life.

Next, I would like to thank Dr. Agnieszka Jaroń-Becker, who is like the co-advisor for me in the group. She has a very broad knowledge and also much experience of researches in both Chemistry and Physics, which inspire and bring us many interesting ideas in our project. She is also very warmhearted and always be ready to help others in both research as well as everyday life.

I also owe many of my thanks to some previous members in our group: Dr. Shaohao Chen, Dr. Antonio Picón, and Dr. Norio Takemoto. When I was a freshman in the group they taught me a lot about numerical simulations, parallel computations, mathematical libraries, and many other things. Talking with them was really helpful and always a lot of fun. I still remember how many times I went to disturb Shaohao in one afternoon when I was learning the numerical library of our group. They are also willing to share their experience of research and life with me and taught me how to make a balance between them.

Working in Becker's ultrafast group is really an amazing experience. The atmosphere in the

group is so good that every one has a smiling face almost every day. We discussed not only Physics but also everything interesting. Thanks to these great and humorous people: Hongcheng Ni, Dr. Carlos Hernández-García, Daniel Weflen, Yuqing Xia, Andrew Spott, Michelle Miller, and Cory Goldsmith.

I also would like to take this opportunity to thank the other members of my thesis committee: Prof. Henry Kapteyn, Prof. Steven Cundiff, and Prof. David Jonas. It is my great honor to have them sit on my committee. As experimentalists, they provided me many interesting ideas and useful suggestions from a different perspective during the discussions in my Comps III exam.

The Janus supercomputer and the clusters at JILA have given me continuous computational support during these years. In particular, the Janus supercomputer has enabled me to do a lot of calculations simultaneously, which has greatly reduced the time of my Ph.D. career. So I am very grateful to all the people working for the Janus supercomputer as well as the staff members of the JILA computing group.

Finally, and most importantly, I would like to thank my family and all of my friends for supporting and encouraging me in so many years. My parents and sister have given me their endless support and unconditional love no matter where I am and whether I am successful or not. A special thank goes to my girlfriend Ye Gu, who has been in a long-distance relationship with me for almost ten years. Without her and my family I would never be able to overcome the difficulties and finally accomplish my Ph.D. study.

Contents

Chapter

Tables

Table

Figures

Figure

Chapter 1

Introduction

1.1 Electron dynamics on the attosecond time scale

Understanding of quantum electron dynamics has played an extremely important role in the development of science and technology in the last 100 years. From chemical reactions between different species to physical interactions of atoms and molecules with external fields, electrons participate in nearly every aspect and their dynamics has been shown to be fundamental and essential for all processes. Based on the energy-time uncertainty principle, $\Delta E \Delta t \sim \hbar$, one expects a time scale of tens to hundreds of femtosecond (1 fs $= 10^{-15}$ s) for vibrational motions in molecules and solids (Fig. 1.1), which defines the characteristic time scale for the motion of atoms in these materials. The time scale of electron dynamics is however even smaller since the energy spacing of electronic energy levels is usually of the order of electron volt (eV). An intuitive picture of this time scale is given by the simple Bohr model for a hydrogen atom. Within this model the kinetic energy of the electron in the ground state is $E_k = v^2/2 = 1/2$ and therefore the period of the classical orbital is $T = 2\pi/v = 2\pi$ in Hartree atomic units (a.u.)[1] , which is on the order of 100 attoseconds (1 as $= 10^{-18}$ s and 1 a.u. $= 24.19$ as).

Many interesting physical processes occur in the attosecond time regime, including XUV photoionization [2–4], strong field tunneling ionization [5, 6], molecular orbital rearrangement after ionization [7], and many other examples. In order to time resolve these attosecond processes, it is necessary to use measurement tools with an attosecond resolution (e.g., [1, 8, 9]). For example, if

[1] Hartree atomic units, $e = m = \hbar = 1$, are used throughout this thesis, unless otherwise stated.

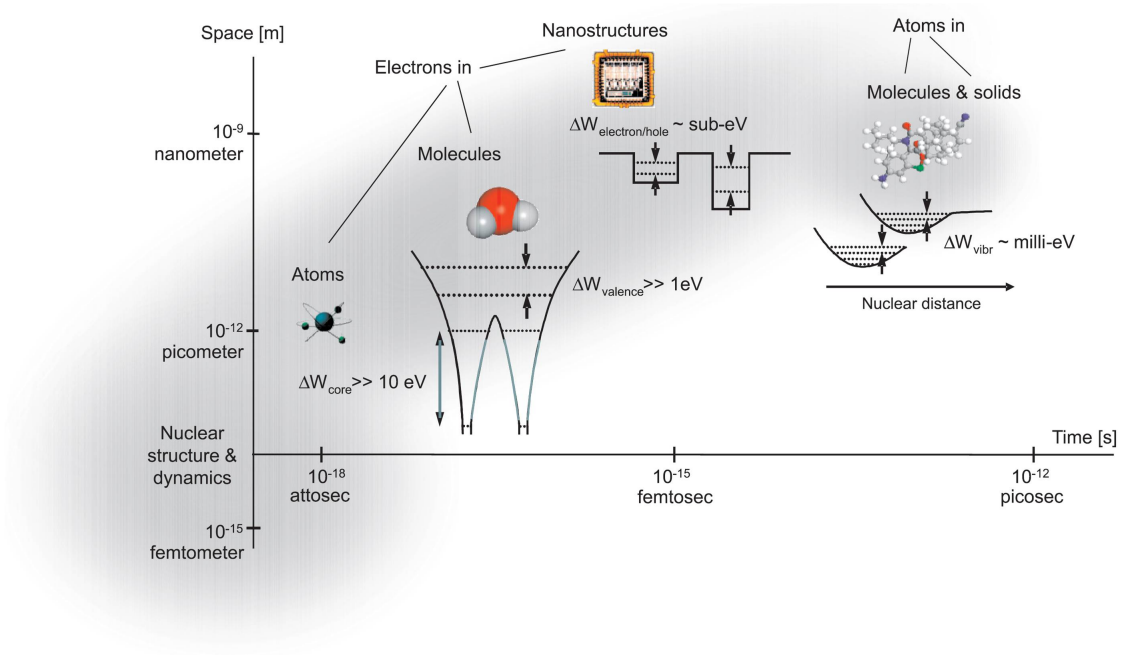

Figure 1.1: Time scales of atomic and electronic motions in atoms, molecules, nanostructures, and solids. Figure captured from Ref. [1].

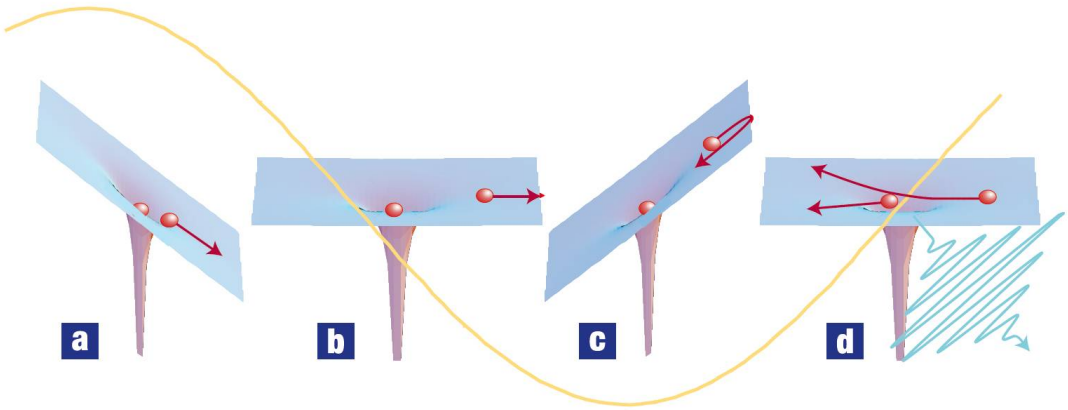

Figure 1.2: Semi-classical description of the HHG process: (a) electron is ionized by the driving laser through tunneling, (b) and (c) electron propagates and accelerates in the laser field, and (d) electron returns and combines with the parent ion by emitting a high-energy photon. Figure captured from Ref. [8].

one wants to study the real-time evolution of electronic orbitals after ionization in a molecule by taking snapshorts of these orbitals, a "camera" with a shutter time on the attosecond time scale is required. Without such a fine resolution, the picture taken will have too much information and the fast motions will be smeared out. The developments of laser technology, in particular the advances in high harmonic generation (HHG) in gases [10–20], have enabled us to generate isolated pulses with attosecond duration, which therefore provide an extremely useful tool for observing attosecond electron dynamics.

1.2 Attosecond pulses generated through high harmonic generation

Strong-field lasers with peak intensities on the order of 10^{13} to 10^{15} W/cm^2 have field strengths comparable to the internal electric field strength in atoms and molecules. Such a strong field hence enables many nonlinear processes to occur, such as the HHG process, which can happen in an atomic or molecular gas medium by focusing an intense laser beam [usually near-infrared (IR)] onto it. The HHG process can be well explained using a semi-classical model [12–14] within three steps (Fig. 1.2): First, an electron initially bound in an atom or molecule is ionized by the strong laser field through the tunneling mechanism. Then the ionized electron propagates and

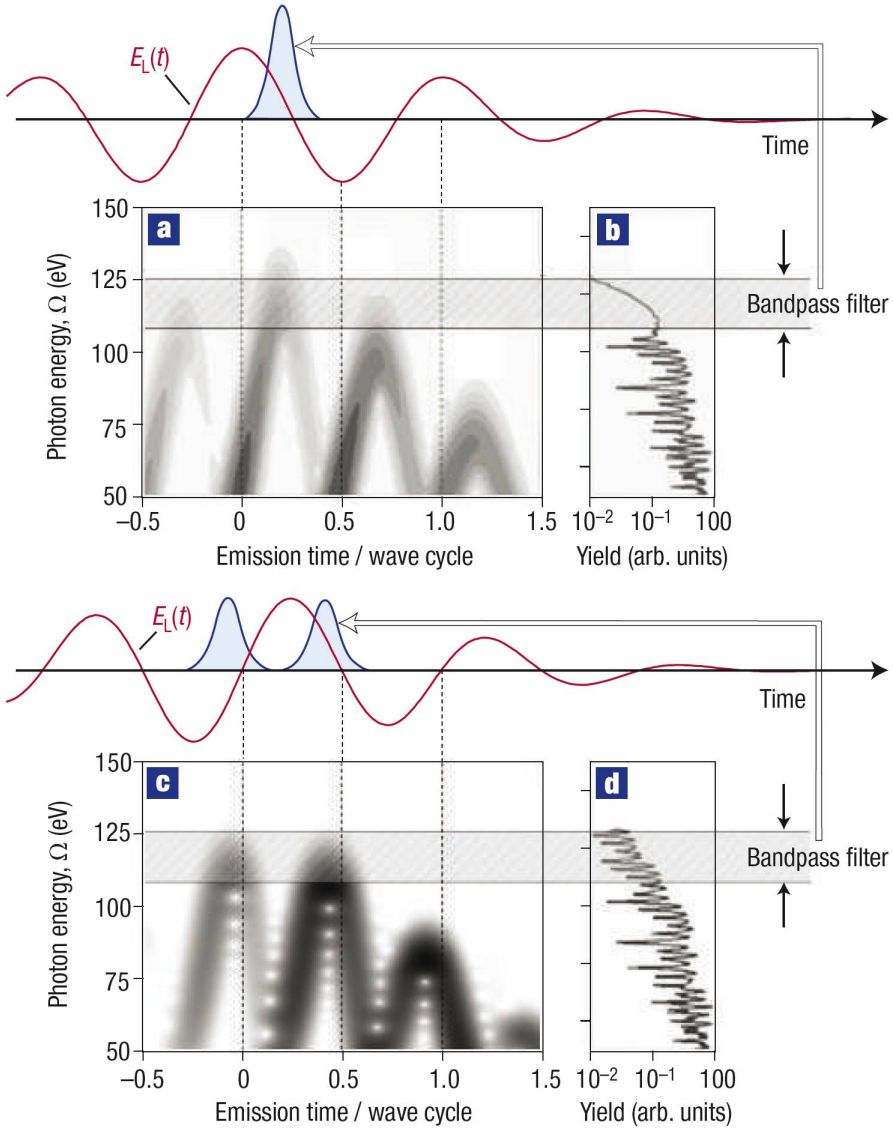

Figure 1.3: Generation of a single- or double-burst attosecond pulse: (a) and (c) The spectrogram (window Fourier transform) of the atomic HHG driven by a 5 fs, 750 nm pulse, (b) and (d) spectra of the emitted high-energy photons. (a) and (b) are calculated for a cosine-shaped driving pulse, while (c) and (d) are for a sine-shaped driving pulse. Filtering out the high-energy part of the HHG spectrum yields a single (a) or double (c) attosecond XUV pulse. Figure captured from Ref. [8].

accelerates under the influence of the strong laser field in the continuum. In the last step, with a certain probability, the electron can be driven back and finally recaptured by the parent atomic or molecular ion. During the recombination of the electron and the parent ion, the electron has to emit an energetic photon in order to conserve the total energy. Classical calculations show that only electrons ionized in the second and fourth quarters of the optical cycle of the laser field can be driven back to the parent ion and then may recombine. This temporal confinement of HHG therefore usually results in the generation of a train of attosecond pulses spaced by half of the optical period of the driving laser pulse.

Classical calculations also reveal that electrons ionized at different phases of the driving laser pulse have different trajectories, returning energies and hence lead to the emission of photons with different energies. A maximum energy of the returning electron occurs for liberation of the electron at 17 ° with respect to the maximum of each half cycle of the driving pulse with the emission of a photon of energy $\Omega = 3.17U_p + I_p$. Here, I_p is the ionization potential of the target system, and $U_p = I/4\omega^2$ is the ponderomotive energy that refers to the cycle-averaged energy of the electron in the driving laser field with I and ω being its intensity and frequency, respectively. The maximum energy of the HHG photon, given by $\Omega = 3.17U_p + I_p$, corresponds to the cutoff energy of the HHG spectrum [e.g., Fig. 1.3(b)]. These conclusions can also be derived within quantum mechanical analysis [15]. As exemplified in Fig. 1.3(a) and (c), a time-frequency analysis [21] of the HHG spectrum clearly shows when different photon frequencies are emitted.

For many applications one prefers to use an isolated attosecond pulse, of which the generation is nowadays possible in a few different ways [19, 22]. Among them, one method is the so-called amplitude gating [18, 23, 24] that makes use of a cosine-shaped laser field comprising merely a few oscillation cycles (Fig. 1.3). In such a case only the electron wave packet ionized in the second quarter of the central half cycle (i.e., the half cycle with largest intensity) has significant contributions to the HHG spectrum, in particular to the high energy part of the spectrum that is around the cutoff energy [Fig. 1.3(a)]. As a result, after filtering out the high energy part of the spectrum, a single, isolated attosecond pulse is generated as illustrated in Fig. 1.3(a) and (b). In

contrast, if one instead uses a sine-shaped laser field, the generated field has two identical bursts after filtering out the same energy region [Fig. 1.3(c) and (d)]. As the first demonstration of this method, experimentalists generated a 650 as pulse with a central frequency of 90 eV by using a 7 fs driving laser at wavelength of 750 nm [23]. Currently, the limit of this method is the generation of a 80 as pulse centered at a photon energy of 80 eV using a 3.5 fs, 720 nm driving laser [24].

Very recently, another very promising method of generating isolated attosecond pulses based on phase matching has been proposed and demonstrated by M.-C. Chen *et al.* [25]. It is well known that electromagnetic fields emitted from different atoms (or molecules) that are phase matched interference constructively and add up coherently [26, 27]. The phase matching condition depends on a few parameters of the experiment, such as the pressure of the gas, the frequency, intensity, and duration of the driving laser pulse [28–30]. In particular, the temporal window over which phase matching occurs shrinks rapidly with increasing driving laser wavelength [25, 30]. In the experimental demonstration a 14-cycle driving laser pulse at a central frequency of 2 μm has been used, which is more stable and easier to generate than few-cycle 800 nm pulses. When the intensity of the driving laser is increased to 1.6×10^{14} W/cm^2 (with a proper pressure of argon gas), the temporal phase matching window is confined to the half peak cycle of the driving pulse and thus a single, isolated soft X-ray pulse is generated. A pulse of duration of 300 as at a central photon energy of 140 eV has been observed. Due to its simple and robust properties, this novel scheme not only provides a new way of generating isolated attosecond pulse but also may make attosecond science and technology accessible to a broader community.

1.3 Attosecond streaking technique and its application to photoionization

The concept of the streak camera has been around for a few decades with the original intention to characterize the temporal structure of a short light pulse [32, 33]. On the left side of Fig. 1.4 a schematic view of a conventional streak camera is shown. In such an apparatus photoelectrons are knocked off a photocathode by a short light pulse. The time-dependent ionization probability is proportional to the temporal intensity of the pulse. During the propagation to the detector screen,

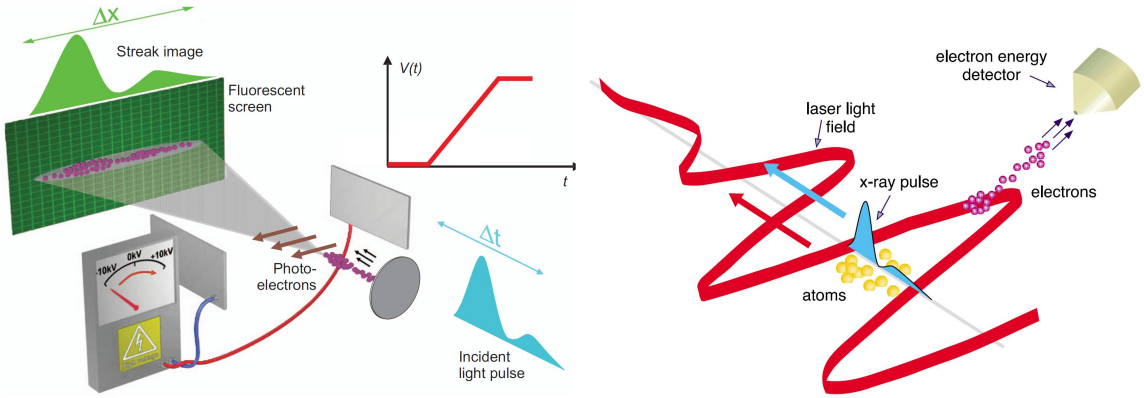

Figure 1.4: Conventional (left, captured from Ref. [1]) and attosecond (right, captured from Ref. [31]) streak cameras. The conventional streak camera uses a transverse voltage ramp to deflect photoelectrons ionized by the incident light pulse. Electrons ionized at different instants have different ionization probabilities and also different horizontal deflections on the detector screen. One can therefore reconstruct the temporal structure of the incident pulse from the electron distribution on the screen. The attosecond streak camera uses an attosecond XUV pulse to initiate an ultrafast process (e.g., ionization) and a few-cycle IR pulse to streak the momentum of the electron. By scanning the XUV pulse at different positions of the streaking pulse, one can measure the momentum as a function of the relative delay between these two pulses, i.e., a streaking trace. The time information of the ultrafast process is stored in the streaking trace.

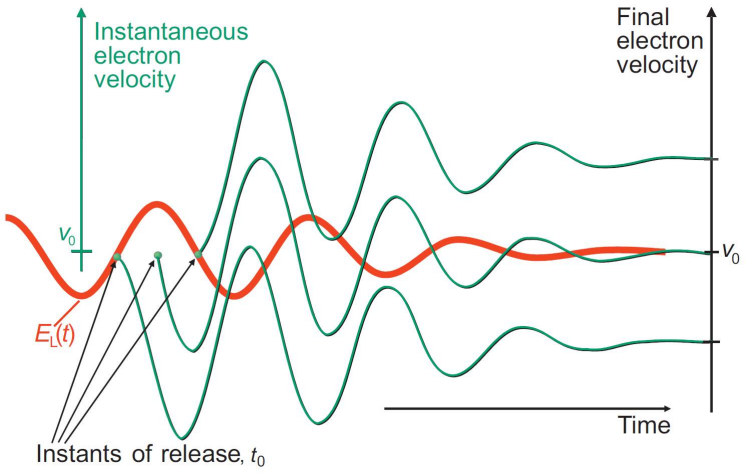

Figure 1.5: Physical principle of the attosecond streak camera. Electrons released by the attosecond XUV pulse at different positions of the streaking pulse have different final momenta, which are approximately given by Eq. (1.1). Figure captured from Ref. [1].

the electrons are deflected by a transverse microwave voltage ramp $V(t)$ and the degree of deflection is directly related to the release instants of the electrons. Therefore the spatial distribution of the photoelectrons on the screen can be converted to the temporal structure of the incident pulse. Such a conventional streak camera setup can reach a subpicosecond (1 ps = 10^{-12} s) resolution for a voltage ramp that is within a fraction of a nanosecond (1 ns = 10^{-9} s).

The attosecond streak camera shares the concept with the conventional one and was originally introduced to measure the temporal structure of an attosecond XUV pulse [23, 34–36]. It consists of two laser pulses: an attosecond XUV pulse that initiates an ultrafast process (e.g., ionization of the electron in atoms and molecules), and a few-cycle streaking pulse (usually an IR pulse) that is used to modulate the final momentum of the photoelectron according to its release instant (see the right side of Fig. 1.4). Photoelectrons ionized by the XUV pulse at different phases of the streaking field have different final asymptotic momenta, which can be easily estimated using classical mechanics by neglecting the Coulomb potential of the parent ion. Assuming that the electron is released at instant t_i and then propagates in the streaking field $\boldsymbol{E}_s(t)$, the final momentum is given within this approximation by

$$\boldsymbol{k}_f \simeq \boldsymbol{k}_0 - \int_{t_i}^{T} \boldsymbol{E}_s(t)dt = \boldsymbol{k}_0 - \boldsymbol{A}_s(t_i), \tag{1.1}$$

where $\boldsymbol{k}_0 = \sqrt{2(\omega - Ip)}$ is the field-free asymptotic momentum with ω being the XUV photon energy and I_p being the ionization potential of the system and $\boldsymbol{A}_s(t)$ is the vector potential of the streaking pulse with duration T and $\boldsymbol{A}_s(T) = 0$. As illustrated in Fig. 1.5, the final momentum clearly depends on the ionization instant and therefore temporal information of the ionization (as well as the XUV pulse) is mapped onto the momentum space. By scanning the application of the XUV pulse as a function of the phase of the streaking pulse, one can obtain a so-called streaking trace (Fig. 1.6), which shows the final energy (or momentum) of the photoelectron as a function of the relative delay between the two pulses. As we will discuss in this thesis such a streaking trace records useful information about the ultrafast process initiated by the XUV pulse.

1.4 Time delay in photoionization and previous theoretical interpretations

As an important demonstration of the possible use of the attosecond streaking technique in attosecond science, Schultze *et al.* [3] applied it to study temporal dynamics of the XUV photoionization process in atoms. They intended to address a few very fundamental questions like: Is there any time delay between ionization processes from different orbitals, for example, the 2s and 2p orbitals in a neon atom? And when does the XUV photoionization occur in an atom? In their experiment two streaking traces are recorded simultaneously for electron emission from the 2s and 2p orbitals in a neon atom[2] by scanning a 200 as attosecond pulse with energy of 100 eV (energetic enough to ionize either electron) with respect to a 4 fs IR streaking pulse (left side of Fig. 1.6).

The answer to the first question appears to be easy to find by directly comparing the two streaking traces of the 2s and 2p photoelectrons. A time delay of 21 ± 5 as for the ionization of the 2p electron with respect to the ionization of the 2s electron was found in the comparison of the traces using several different data processing algorithms [3]. The authors hence claimed they have observed that the 2p electron takes more time to ionize than the 2s electron. In order to clearly see that there is indeed a small temporal shift (or time delay) between the traces, which is not so obvious in the original experimental data (left side of Fig. 1.6), we show also an example of time delay streaking results from Ref. [37] on the right side of Fig. 1.6, which are based on numerical simulations of streaking experiments in two atoms. By comparing the two traces from ground state ionization of the hydrogen atom and the helium ion atom, a time delay of about 30 as can be clearly seen from the inset of this figure.

In order to address the second question, one common way is to use the streaking trace predicted by the original streaking formula, Eq. (1.1), as a zero-time reference. Since the relative delay between the XUV and streaking pulses is defined to be the time difference of the center of the XUV pulse with respect to that of the streaking pulse with a positive sign representing that the XUV pulse is applied at the trailing edge of the streaking pulse, one actually uses the center of the

[2] The same idea has been also applied to a solid system to study the photoionization time delay between ionization from a valence and a conduction band [2].

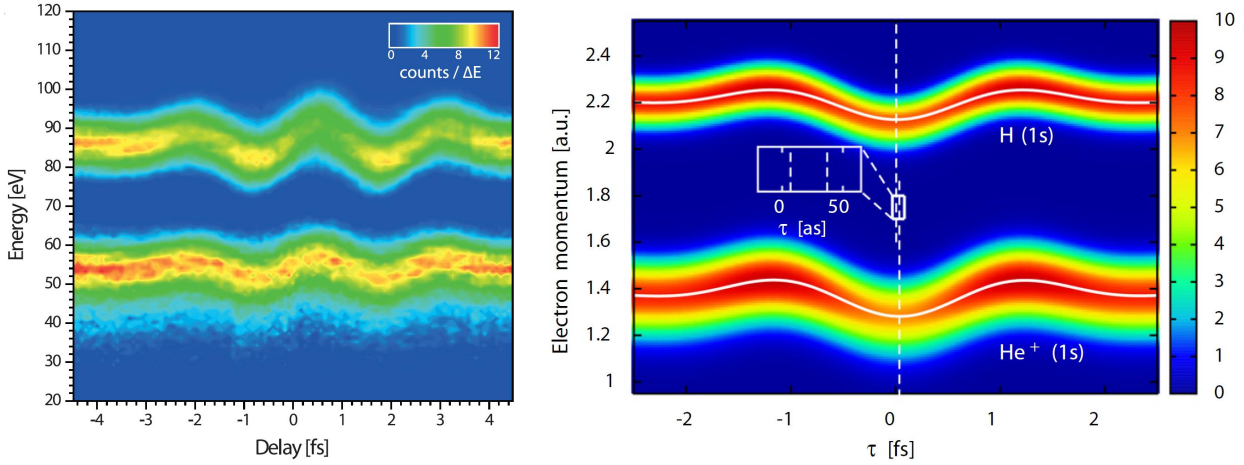

Figure 1.6: Streaking traces from experimental measurements in neon atoms (left, captured from Ref. [3]) and numerical simulations in hydrogen and helium ion atoms (right, captured from Ref. [37]). In the left figure the upper and lower traces correspond to the 2s and 2p electrons respectively. In the right figure the central white line of each trace is the expectation value of the momentum.

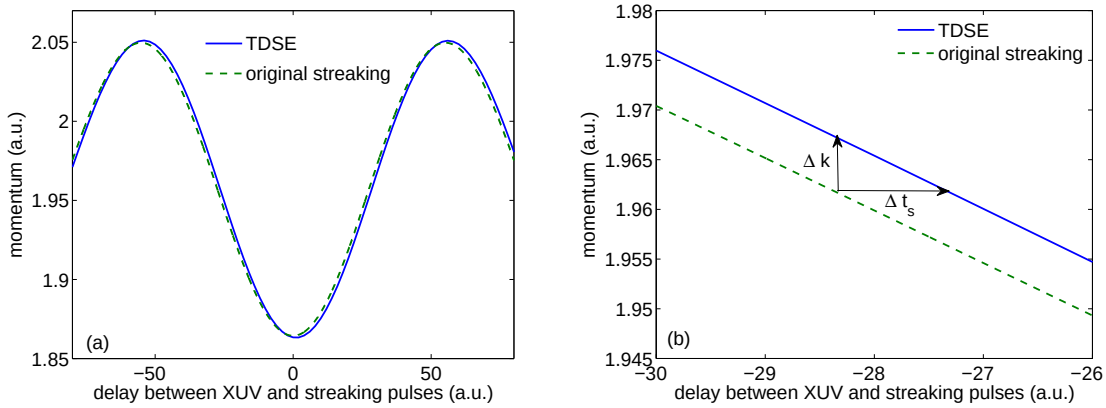

Figure 1.7: (a) Streaking traces obtained from numerical simulations for photoemission in the 1D Coulomb potential $V_C(z) = -3.0/\sqrt{z^2 + 2.0}$. A 8-cycle streaking pulse with $I_s = 1 \times 10^{12}$ W/cm^2, $\lambda_s = 800$ nm, and $\phi_s = -\pi/2$ is used in the calculations. We compare the streaking trace obtained from the TDSE (blue solid line) with that from the original streaking formula, Eq. (1.1), (green dashed line). (b) An enlargement of (a) to show the momentum shift Δk, the streaking time delay Δt_s, and the relation between them.

XUV pulse as the zero time reference when comparing the experimentally observed or theoretically calculated streaking traces to the predicted one. To exemplify this concept, in Fig. 1.7 we show the streaking trace from the numerical solution of the time-dependent Schrödinger equation (TDSE) corresponding to photoemission of an electron in a 1D model potential (blue solid line) as well as the trace predicted by the original streaking formula, Eq. (1.1), (green dashed line). Here we only show the expectation value of the numerically obtained final momentum in order to visualize the relative shift between the two traces. A clear temporal offset (or time delay) can be seen in Fig. 1.7(b) when we zoom into a certain part of the traces. As used by others (e.g., [37–39]), we denote such a temporal offset as the streaking time delay Δt_s. Theoretically, the trace from the original streaking formula provides a reference to study the origin of time delays and we will take advantage of this method in all of our studies within this thesis.

The photoionization time delay experiment by Schultze *et al.* [3] has initiated a lot of theoretical interest, in particular in view of the interpretation of the delay. In the original report [3], Schultze *et al.* gave a qualitative estimation and explanation of the delay by relating it to the so-called Wigner-Smith (WS) time delay [40, 41]. The WS time delay is a concept introduced in scattering studies and is defined to be the time difference between the time a particle spends within the scattering potential and the time that a free particle with an equal final energy spends in the same region under the condition that the region extends from $-\infty$ to $+\infty$. For a short-range potential that decays faster than $1/r$, the WS time delay can be evaluated by

$$\Delta t_{\mathrm{WS}} = \frac{d\varphi}{dE}, \tag{1.2}$$

with φ being the scattering phase shift. Since the WS delay diverges for a long-range Coulomb interaction [41], Schultze *et al.* [3] employed Eq. (1.2) to avoid the divergence problem, which later raised concerns from some theorists including us (e.g., [42, 43]). This WS delay concept was later revisited by Kheifets *et al.* in Ref. [44], in which an extension of this method was proposed to take account of the extra phase shift induced by the multielectron correlation effect[3] . However,

[3] Although its relation to the streaking time delay remains somehow unclear, the WS time delay concept in the

neither the original WS calculation nor the extension could reproduce the time delay measured in the experiment.

In order to seek further interpretation, it was proposed to compare the streaking time delay with the WS time delay for some single-electron potentials such as the hydrogen atom and the helium ion atom, in which direct numerical simulations of streaking experiments without any approximations are possible. Nagele *et al.* [37] and Zhang *et al.* [52] independently found that, generally, the streaking time delay is not given by the WS time delay calculated using Eq. (1.2) even for these simple single-electron systems, except for very short-ranged potentials. This discrepancy however implies there should be some additional contribution to the streaking time delay. Nagele *et al.* [37] pointed out that the (classical) propagation of the photoelectron in the coupled field of the atomic potential and the streaking pulse can induce an extra momentum shift to the original formula, Eq. (1.1), and therefore should give rise to an additional time delay. This coupling effect can be viewed as a correction to the strong field approximation (that neglects the Coulomb potential) used in the derivation of Eq. (1.1). They hence proposed to use a classical-trajectory Monte Carlo simulation, which treats the Coulomb potential on equal footing with the streaking field, to calculate this coupling related time delay and showed that the obtained coupling delay Δt_{CLC}[4] is equal to the streaking time delay. However, the authors did not further elaborate on this result.

Instead, inspired by this result, Ivanov *et al.* [38] derived an analytical formula for the coupling time delay Δt_{CLC} via a quantum approach based on eikonal approximation. Based on this approximation, their analysis implies that for a hydrogen atom the streaking time delay can be approximated as $\Delta t_s = \Delta t_{\mathrm{WS}} + \Delta t_{\mathrm{CLC}}$ with Δt_{WS} given by Eq. (1.2). By separating the neon potential into a $-1/r$ potential and a remaining short-range part, they applied this relation to both parts and obtained a total time delay of 18 as, which is within the uncertainty of the measured streaking delay of 21 ± 5 as and seems to explain the experimental result. However, later Nagele *et*

mean time has been widely used in theoretical analysis of time delays in atomic and molecular photoionizations (e.g., [45–51]).

[4] Here, "CLC" refers to "Coulomb laser coupling". Since the coupling delay Δt_{CLC} is induced by the classical propagation of the electron in the coupled field the ionic potential and the streaking pulse, most of the time we call it propagation time delay Δt_{prop} in this thesis.

al. [53] pointed out that the sum rule $\Delta t_s = \Delta t_{\rm WS} + \Delta t_{\rm CLC}$ cannot be generalized to short-range potentials since for short-range potentials the streaking time delay is found to be equal to the WS time delay and hence there should be no coupling delay contribution. As a result they interpreted that the coupling delay $\Delta t_{\rm CLC}$ solely arises from the coupling effect of the long-range tail of the Coulomb potential with the streaking field. In other words, they suggested to separate the whole potential into two parts, where for the short-range part $\Delta t_s = \Delta t_{\rm WS}$ while for the long-range part $\Delta t_s = \Delta t_{\rm CLC}$. Since the long-range Coulomb tail is the same for single-electron systems with the same parent ion charge, they further proposed that one can calculate the coupling delay by employing $\Delta t_{\rm CLC} = \Delta t_s - \Delta t_{\rm WS}$ for the hydrogen atom and then make use of it for all other more complex systems. Similar to the work of Ivanov *et al.* [38], Zhang *et al.* [39] also obtained the coupling time delay $\Delta t_{\rm CLC}$ using eikonal approximation and compared it with the streaking time delay, but they did not further relate their results with the proposed sum rule. Therefore, up to now, the debate about the interpretation of the streaking time delay even in single-electron systems is still going on. In particular, the following questions remain not fully answered: Is the streaking time delay related to the WS time delay? If yes, how are they related? For a short-range potential, is there a coupling time delay and how can it be calculated? Is the sum rule $\Delta t_s = \Delta t_{\rm WS} + \Delta t_{\rm CLC}$ true? And is it necessary to separate a Coulomb potential into two parts (short-range and long-range) in order to apply the proposed sum rule accordingly?

Meanwhile some other effects including the polarization effect and the multielectron effect were also investigated. For example, Baggesen *et al.* [54], Zhang *et al.* [39], and Nagele *et al.* [37] independently studied the influence of the polarization of the initial state due to the streaking pulse on the streaking time delay. Although they reach different conclusions for which initial state this effect is present and how the time delay related to this effect can be calculated, their works indicate that this effect may influence the streaking time delays measured in streaking experiments. Another important effect in streaking experiments is the multielectron correlation in photoionization. Due to the properties of noble gases, experimentalists prefer to use them in studying ultrafast processes, which however may increase the theoretical difficulty in analyzing them. The neon atom used by

Schultze *et al.* in the time delay experiment is such an example. There are ten electrons in a neon atom and at least eight of them (2s and 2p electrons) will rearrange during the photoionization process in the delay experiment even though only one of them will be ionized. The correlation effect has been shown (e.g., [44, 53, 55, 56]) to be important and may have a quite significant contribution to the measured delay. However, due to the complexity of this multielectron system, solving the problem from first principles without any approximations is still not feasible.

The time delay concept can also been implemented using the so-called reconstruction of attosecond beating by interference of two-photon transition (RABITT) technique, in which an attosecond pulse train is used instead of an isolated pulse (see Refs. [4, 57] for details). Theoretically, it was shown (e.g., [58, 59]) that the RABITT technique gives rise to the same time delay as the attosecond streaking technique if applied to the same system.

1.5 Organization of this thesis

As discussed in the last section, the debate on the interpretation of the streaking time delay is still ongoing and many related questions need to be addressed, even for single-electron systems like the hydrogen atom. In order to contribute to this debate and provide an independent interpretation of the streaking time delay, we study the time delay concept as well as the streaking experiment in detail and systematically in this thesis. Inspired by the concerns about the sum rule $\Delta t_s = \Delta t_{\mathrm{WS}} + \Delta t_{\mathrm{CLC}}$, we investigate the problem from two aspects: On the one hand, we start our studies by revisiting the WS time delay concept including the proposal of a new time-dependent numerical method to calculate Δt_{WS} and its application in the photoionization process. On the other hand, we employ a classical model to describe the electron dynamics in the coupled field of the ionic potential and the streaking pulse and calculate the coupling (or propagation) time delay. Based on the results from these two aspects, we are able to conclude that: (a) The WS time delay indeed diverges for a long-range potential and therefore is not suitable to explain (even partially) the streaking time delay. (b) For single-photon ionization (SPI) in a single-electron system (without polarization effect), the coupling (or propagation) time delay is equal to the streaking time delay and hence it

is the only contribution to the streaking delay. Moreover, the coupling time delay, or equivalently the streaking time delay, can be interpreted as the sum of piecewise field-free time delays weighted by the ratio of the instantaneous streaking field strength relative to the field strength at the instant of ionization[5] . With our understanding of the attosecond streaking technique, in particular of the streaking time delay, we are able to use this tool to study other ultrafast processes such as the two-photon ionization (TPI) process, in which a few new and interesting phenomena are observed in our numerical simulations. The structure and organization of this thesis is given as follows.

In Chapter 2 we review the numerical model that we use to describe the atomic or molecular system of interest as well as the method that is utilized to numerically solve the corresponding time-dependent Schrödinger equation (TDSE). We first introduce two different methods to obtain a single-active-electron (SAE) model for a multielectron system, which can significantly reduce our numerical cost in simulating laser-matter interactions. Then in the second section we review the solution of the TDSE in a grid representation using the finite difference method. The propagation scheme, the method of obtaining the initial eigenstates, and the boundary conditions are described in detail respectively in this section as well.

Chapter 3 is the central part of this thesis, in which we study the time delay in SPI from a few different perspectives. In the first section, we introduce a new numerical method to calculate the WS time delay for the photoionization process based on its fundamental definition by solving the TDSE. This new method gives a time-dependent view on the WS time delay and thus clearly shows its evolution during the propagation of the electron in the potential, which is not available from the original definition of the WS time delay. The results reconfirm that the WS time delay is an ill-defined concept for photoionization in a long-range potential and hence its application to the streaking experiment is questionable. In the second section, we focus on the analysis of the streaking experiment. We propose to consider the electron dynamics after the photon absorption in the combined field of the ionic potential and the streaking field by a classical model. The

[5] We define the instant of ionization as the instant of the transition of the electron into the continuum by absorbing photons.

results for the propagation time delay given by this model indeed agree very well with the streaking time delay obtained in TDSE simulation, which indicates that the propagation time delay is the only contribution to the streaking time delay, i.e., the streaking time delay arises from the finite propagation of the electron from the instant of ionization to the end of the streaking pulse in the combined potential. We further show that one can interpret the propagation time delay as a finite sum (or integral) of the piecewise field-free time delays weighted by a relative field strength. We also note that the finite-range property of the streaking time delay opens the possibility to use the streaking technique as a new tool of imaging. To relate our theoretical analysis to the experiment, we also study the influence of some experimental parameters such as the presence of the additional static field and the long tail of the streaking pulse on the streaking time delay.

Our studies of the streaking time delay in SPI imply that the photon absorption in SPI occurs most likely (in a quantum mechanical sense) at the center of the attosecond XUV pulse. In Chapter 4, we extend our studies to two-photon absorption processes. After properly accounting for the propagation (or measurement-induced) time delay, we show that for the nonresonant TPI, the two-photon absorption process occurs simultaneously with SPI, i.e., most likely at the center of the XUV pulse. However time delays obtained for the resonant TPI are significantly different: The absorption of the second photon occurs with a positive time delay with respect to the center of the XUV pulse and this delay changes linearly with the XUV duration. In the second section, we confirm these findings from the streaking simulations with a trajectory analysis based on TDSE simulations and an analysis of the phase acquired in the two-photon absorption process using second-order perturbation theory. These findings in TPI, in particular the linear dependence of the absorption time delay on the XUV duration, suggest a new way of controlling the initiation of ultrafast processes, which for example may be useful in controlling chemical reactions. In the third section of this chapter, we review our early work of two-photon coherent control of excitation in molecular model potentials, which does not directly relate to the time delay work but may inspire some future applications of the TPI delay. We end our thesis with a summary of our work in these five years.

Chapter 2

Numerical Model and Method

It is well-known that ultrafast quantum processes, including the interaction of atoms and molecules with laser fields, can be described by the time-dependent Schrödinger equation (TDSE), that however usually does not have an analytical solution. Nowadays with the development of super computers, numerically solving the TDSE is becoming more and more popular. Therefore, before we discuss certain quantum processes in detail, it is necessary to introduce and clarify the model and method we use in our numerical simulations. In section 2.1, we describe the single-active-electron (SAE) model, in which only one electron in a multielectron system is treated as active while all the others are considered to be frozen as a background. In section 2.2, we present our numerical approaches to solving TDSE, including the methods of obtaining initial field-free states, propagating the wave function in the time domain, and applying different absorbing boundary conditions.

2.1 Single-active-electron model for atoms and molecules

Consider a system consisting of N nuclei and n electrons interacting with an external field $\boldsymbol{A}(\boldsymbol{r},t)$. The Hamiltonian of such a system is given by

$$\begin{aligned} H(\boldsymbol{R}_1,\cdots,\boldsymbol{R}_N;\boldsymbol{r}_1,\cdots,\boldsymbol{r}_n;t) = \sum_\alpha \frac{1}{2m_\alpha}\left[\boldsymbol{p}_\alpha - Z_\alpha \boldsymbol{A}(\boldsymbol{R}_\alpha,t)\right]^2 + \sum_i \frac{1}{2m_i}\left[\boldsymbol{p}_i + \boldsymbol{A}(\boldsymbol{r}_i,t)\right]^2 \\ + V(\boldsymbol{R}_1,\cdots,\boldsymbol{R}_N;\boldsymbol{r}_1,\cdots,\boldsymbol{r}_n), \end{aligned} \tag{2.1}$$

where $\boldsymbol{p}_\alpha$ and $\boldsymbol{p}_i$ are the canonical momentum operator for the nucleus α with position $\boldsymbol{R}_\alpha$, mass m_α, and charge Z_α and electron i with position $\boldsymbol{r}_i$, mass m_i, and charge $Z_i = 1$, respectively and

the last potential term consists of three contributions from the charge-charge Coulomb interactions, i.e.,

$$V(\boldsymbol{R}_1,\cdots,\boldsymbol{R}_N;\boldsymbol{r}_1,\cdots,\boldsymbol{r}_n)=\sum_{\alpha}\sum_{\beta>\alpha}\frac{Z_\alpha Z_\beta}{|\boldsymbol{R}_\alpha-\boldsymbol{R}_\beta|}-\sum_{\alpha}\sum_{i}\frac{Z_\alpha}{|\boldsymbol{R}_\alpha-\boldsymbol{r}_i|}+\sum_{j}\sum_{i>j}\frac{1}{|\boldsymbol{r}_i-\boldsymbol{r}_j|}. \quad (2.2)$$

To study the electron and nuclei dynamics in such a system from first principles, one needs to solve the corresponding TDSE, which is very challenging even for a two-particle (six-dimensional) system via numerical approaches. Therefore, approximately describing a complex multielectron system with simple models is always of interest for theoreticians. In the case of investigating ultrafast electron dynamics in atoms and molecules, the dynamics of the complex system can be often well approximated by the Born-Oppenheimer approximation, in which the nuclei barely change their positions and hence can be assumed as fixed in the time window of the electron dynamics. This approximation reduces the system from an $(N+n)$-particle problem to an n-electron problem, which effectively decreases the numerical complexity. Furthermore, when analyzing electron dynamics, almost in all cases only a few electrons participate in the interactions with internal or external fields and in many cases (e.g., the HHG process) only one electron is effectively involved. This leads to the development of single-active-electron (SAE) models, in which only one electron is treated as active and the analysis is focused on the dynamics of this electron in the quantum process of interest. Meanwhile, all the other electrons are considered to be frozen and their influence on the active electron is modeled by an effective potential. There are different approaches of generating a SAE potential for the same system. Here in this section, we introduce two of them, namely, the potential average (PA) method, and the optimized effective potential (OEP) method.

2.1.1 Potential average method

The idea of the PA method is very intuitive. For an n-electron system with all nuclei fixed, the wave function and the potential can be written as $\Psi(\boldsymbol{r}_1,\cdots,\boldsymbol{r}_n)$ and $V(\boldsymbol{r}_1,\cdots,\boldsymbol{r}_n)$, respectively, with $\boldsymbol{r}_1$ to $\boldsymbol{r}_n$ being the electron's positions. Then the SAE potential can be constructed as

$$V(\boldsymbol{r}_1)=\frac{\int d\boldsymbol{r}_2\cdots d\boldsymbol{r}_n\Psi^*(\boldsymbol{r}_1,\cdots,\boldsymbol{r}_n)V(\boldsymbol{r}_1,\cdots,\boldsymbol{r}_n)\Psi(\boldsymbol{r}_1,\cdots,\boldsymbol{r}_n)}{\int d\boldsymbol{r}_2\cdots d\boldsymbol{r}_n\Psi^*(\boldsymbol{r}_1,\cdots,\boldsymbol{r}_n)\Psi(\boldsymbol{r}_1,\cdots,\boldsymbol{r}_n)}, \quad (2.3)$$

Table 2.1: Comparison of eigenenergies (in atomic units) from different methods for neon atom. The experimental values are from Ref. [60], the HF results are from Ref. [61], and all the other results are from our calculations.

orbital	experimental	HF	PA	LSDA	KLI+SIC+LSDA
1s	−31.979	−32.772	−32.520	−30.306	−31.129
2s	−1.782	−1.930	−1.244	−1.271	−1.662
2p	−0.797	−0.850	−0.457	−0.442	−0.805

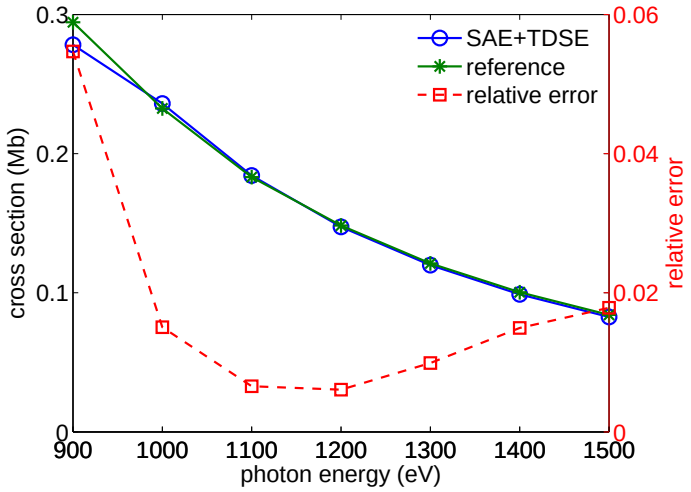

Figure 2.1: Neon photoionization cross section as a function of photon energy. The blue solid line with circles are numerical TDSE results by simulating the photoionization process in the SAE potential produced using the PA method, and the green solid line with asterisks are data from Ref. [62]. The relative error between them are shown as the red dashed line with squares (right axis).

where we assume the electron with coordinate $\boldsymbol{r}_1$ is the active electron and integrate out all the other coordinates $\boldsymbol{r}_2$ to $\boldsymbol{r}_n$. For most of the atoms, the multielectron wave function can be respresented in terms of Slater type functions, which can be found in some references. And for a complex system like a molecule, one can use quantum chemistry softwares (e.g., GAUSSIAN and GAMESS) to calculate its wave function. Usually the wave function is in a Hartree-Fock (HF) form, which consists of one Slater determinant or a sum of several Slater determinants.

To simplify the model, we further assume that our wave function can be written in the Hartree approximation, i.e.,

$$\Psi(\boldsymbol{r}_1, \cdots, \boldsymbol{r}_n) = \phi_1(\boldsymbol{r}_1) \cdots \phi_n(\boldsymbol{r}_n), \tag{2.4}$$

where $\phi_i(\boldsymbol{r}_i)$ is the normalized wave function of the ith electronic orbital, and for different orbitals, $\phi(\boldsymbol{r})$'s are orthogonal. As mentioned above, the potential of a complex system with electrons (labeled by i and j) and fixed nuclei (labeled by α and β) is given by

$$V(\boldsymbol{r}_1, \cdots, \boldsymbol{r}_n) = \sum_{\alpha} \sum_{\beta>\alpha} \frac{Z_\alpha Z_\beta}{|\boldsymbol{R}_\alpha - \boldsymbol{R}_\beta|} - \sum_{\alpha} \sum_{i} \frac{Z_\alpha}{|\boldsymbol{R}_\alpha - \boldsymbol{r}_i|} + \sum_{j} \sum_{i>j} \frac{1}{|\boldsymbol{r}_i - \boldsymbol{r}_j|}. \tag{2.5}$$

Since the first term here does not depend on $\boldsymbol{r}$, it does not change when substituted to Eq. (2.3). For the second term, if $i = 1$, we have

$$\begin{aligned} \sum_{\alpha} \langle \frac{Z_\alpha}{|\boldsymbol{R}_\alpha - \boldsymbol{r}_1|} \rangle &= \sum_{\alpha} \frac{\phi_1^*(\boldsymbol{r}_1)(Z_\alpha/|\boldsymbol{R}_\alpha - \boldsymbol{r}_1|)\phi_1(\boldsymbol{r}_1)}{\phi_1^*(\boldsymbol{r}_1)\phi_1(\boldsymbol{r}_1)} & (2.6) \\ &= \sum_{\alpha} \frac{Z_\alpha}{|\boldsymbol{R}_\alpha - \boldsymbol{r}_1|}, & (2.7) \end{aligned}$$

which also remains unchanged under Eq. (2.3). When $i \neq 1$, we have

$$\begin{aligned} \sum_{\alpha} \sum_{i\neq 1} \langle \frac{Z_\alpha}{|\boldsymbol{R}_\alpha - \boldsymbol{r}_i|} \rangle &= \sum_{\alpha} \sum_{i\neq 1} \frac{\int \phi_i^*(\boldsymbol{r}_i)(1/|\boldsymbol{R}_\alpha - \boldsymbol{r}_i|)\phi_i(\boldsymbol{r}_i) d\boldsymbol{r}_i}{\int \phi_i^*(\boldsymbol{r}_i)\phi_i(\boldsymbol{r}_i) d\boldsymbol{r}_i} & (2.8) \\ &= \sum_{\alpha} \sum_{i\neq 1} \int \frac{|\phi_i(\boldsymbol{r}_i)|^2}{|\boldsymbol{R}_\alpha - \boldsymbol{r}_i|} d\boldsymbol{r}_i. & (2.9) \end{aligned}$$

In our current model, all the nuclei are assumed to be fixed, so the double sum integral above is a constant, which is equivalent to a shift of all energy levels. Now we consider the third term, if

$j = 1$, then

$$\sum_{i\neq 1}\langle\frac{1}{|\boldsymbol{r}_1-\boldsymbol{r}_i|}\rangle = \sum_{i\neq 1}\frac{\int\phi_i^*(\boldsymbol{r}_i)(1/|\boldsymbol{r}_1-\boldsymbol{r}_i|)\phi_i(\boldsymbol{r}_i)d\boldsymbol{r}_i}{\int\phi_i^*(\boldsymbol{r}_i)\phi_i(\boldsymbol{r}_i)d\boldsymbol{r}_i} \tag{2.10}$$

$$= \sum_{i\neq 1}\int\frac{|\phi_i(\boldsymbol{r}_i)|^2}{|\boldsymbol{r}_1-\boldsymbol{r}_i|}d\boldsymbol{r}_i. \tag{2.11}$$

For $j \neq 1$, we have

$$\sum_{i>j}\sum_{j\neq 1}\langle\frac{1}{|\boldsymbol{r}_i-\boldsymbol{r}_j|}\rangle = \sum_{i>j}\sum_{j\neq 1}\frac{\int\int\phi_i^*(\boldsymbol{r}_i)\phi_j^*(\boldsymbol{r}_j)(1/|\boldsymbol{r}_i-\boldsymbol{r}_j|)\phi_i(\boldsymbol{r}_i)\phi_j(\boldsymbol{r}_j)d\boldsymbol{r}_i d\boldsymbol{r}_j}{\int\int\phi_i^*(\boldsymbol{r}_i)\phi_j^*(\boldsymbol{r}_j)\phi_i(\boldsymbol{r}_i)\phi_j(\boldsymbol{r}_j)d\boldsymbol{r}_i d\boldsymbol{r}_j} \tag{2.12}$$

$$= \sum_{i>j}\sum_{j\neq 1}\int\int\frac{|\phi_i(\boldsymbol{r}_i)|^2|\phi_j(\boldsymbol{r}_j)|^2}{|\boldsymbol{r}_i-\boldsymbol{r}_j|}d\boldsymbol{r}_i d\boldsymbol{r}_j. \tag{2.13}$$

This double sum is also a constant, which does not influence the shape of the effective potential. Thus, by neglecting the constant terms, we can write down the SAE potential as

$$V(\boldsymbol{r}_1) = -\sum_{\alpha}\frac{Z_\alpha}{|\boldsymbol{R}_\alpha-\boldsymbol{r}_1|} + \sum_{i\neq 1}\int\frac{|\phi_i(\boldsymbol{r}_i)|^2}{|\boldsymbol{r}_1-\boldsymbol{r}_i|}d\boldsymbol{r}_i. \tag{2.14}$$

The physical meaning of each term in Eq. (2.14) is clear: the first term is the attraction energy between the active electron (associated with coordinate $\boldsymbol{r}_1$) and the nuclei, and the second term is the repulsion energy between the active electron and all the other frozen electrons, which now are treated as an electron distribution. For an ultrafast process in which the Born-Oppenheimer approximation applies, we can calculate an effective potential for each nuclei configuration $\{\boldsymbol{R}_\alpha\}$, in case we want to include the nuclear motions.

To test this model, we calculate eigenenergies of several lowest energy levels for small atoms (e.g., He, Li, and Ne) and compare them with the accurate experimental results. Interestingly, this simple model provides good results for the lowest inner shell orbital (for atoms, the 1s orbital), where we find that the calculated energy is very close to the real one (e.g., see Table 2.1). This indicates that the exchange-correlation effect, which is neglected by this model, is not important for the most inner-shell electrons. We have also calculated the photoionization cross section as a function of photon energy for several atoms. For the neon atom (Fig. 2.1) there is a good agreement between results of our TDSE calculations based on the present SAE model and those from Ref. [62].

2.1.2 Optimized effective potential method

The PA method we proposed in the last subsection is easy to implement and works well for inner-shell electrons. However, it ignores the important exchange-correlation effect and is therefore not ideal for outer-shell electrons (see Table 2.1), which however are of importance in many laser-matter interaction processes (e.g., HHG). Fortunately, some more accurate models for outer-shell electrons have been established and well-tested based on density functional theory (DFT). In this section, we introduce one modified optimized effective potential (OEP) scheme using the self-interaction-free DFT.

In the Kohn-Sham (KS) DFT formulation [63], the one-electron effective potential is given as

$$V_\sigma(\boldsymbol{r}) = -\sum_\alpha \frac{Z_\alpha}{|\boldsymbol{R}_\alpha - \boldsymbol{r}|} + \int \frac{\rho(\boldsymbol{r}')}{|\boldsymbol{r} - \boldsymbol{r}'|} d\boldsymbol{r}' + V_{\mathrm{xc}\sigma}(\boldsymbol{r}), \tag{2.15}$$

where $\boldsymbol{R}_\alpha$ and $\boldsymbol{r}$ are defined as before, σ is the spin polarization, $\rho(\boldsymbol{r})$ is the total electron density

$$\rho(\boldsymbol{r}) = \sum_\sigma \sum_{i=1}^{N_\sigma} |\phi_{i\sigma}(\boldsymbol{r})|^2, \tag{2.16}$$

and $V_{\mathrm{xc}\sigma}(\boldsymbol{r})$ is the exchange-correlation potential given by

$$V_{\mathrm{xc}\sigma}(\boldsymbol{r}) = \frac{\delta E_{\mathrm{xc}}[\rho_\uparrow, \rho_\downarrow]}{\delta \rho_\sigma(\boldsymbol{r})}. \tag{2.17}$$

Once the specific form of the exchange-correlation functional $E_{\mathrm{xc}}[\rho_\uparrow, \rho_\downarrow]$ is known, we can solve the KS equation

$$\left[-\frac{1}{2}\nabla^2 + V_\sigma(\boldsymbol{r})\right] \phi_{i\sigma}(\boldsymbol{r}) = \varepsilon_{i\sigma} \phi_{i\sigma}(\boldsymbol{r}), \tag{2.18}$$

in a self-consistent way.

However, in the traditional DFT, most forms of $E_{\mathrm{xc}}[\rho_\uparrow, \rho_\downarrow]$, such as the local spin density approximation (LSDA) [63], contains spurious self-interaction contributions. This self-interaction contribution can be seen from the total energy

$$E[\rho_\uparrow, \rho_\downarrow] = T[\rho] - \sum_\alpha Z_\alpha \int \frac{\rho(\boldsymbol{r})}{|\boldsymbol{R}_\alpha - \boldsymbol{r}|} d\boldsymbol{r} + \frac{1}{2} \int\int \frac{\rho(\boldsymbol{r})\rho(\boldsymbol{r}')}{|\boldsymbol{r} - \boldsymbol{r}'|} d\boldsymbol{r} d\boldsymbol{r}' + E_{\mathrm{xc}}[\rho_\uparrow, \rho_\downarrow], \tag{2.19}$$

where $T[\rho]$ is the total noninteracting kinetic energy. For a one-electron system the last two terms should in principle cancel each other. However, in real calculations, one has to take some approximations of $E_{\rm xc}[\rho_\uparrow, \rho_\downarrow]$, which usually do not satisfy this requirement. The self-interaction contribution may result in an inaccuracy of the energies of the outer-shell orbitals, because it causes an incorrect long-range behavior of the effective potential in Eq. (2.15). Thus, to construct a good SAE model for outer-shell electrons, one has to find some efficient way to eliminate the self-interaction contribution. Many methods have been suggested to solve the self-interaction problem. Here we introduce two of them: the self-interaction correction (SIC) method [64] and the Krieger-Li-Iafrate (KLI) method [65–67] based on the optimized effective potential (OEP) scheme [68, 69].

In the SIC approach [64], the following form of the exchange-correlation functional is used:

$$E_{\rm xc}^{\rm SIC}[\rho_\uparrow, \rho_\downarrow] = E_{\rm xc}[\rho_\uparrow, \rho_\downarrow] - \sum_\sigma \sum_{i=1}^{N_\sigma} \{\frac{1}{2} \int\int \frac{\rho_{i\sigma}(\boldsymbol{r})\rho_{i\sigma}(\boldsymbol{r}')}{|\boldsymbol{r}-\boldsymbol{r}'|} d\boldsymbol{r} d\boldsymbol{r}' + E_{\rm xc}[\rho_{i\sigma}, 0]\}, \tag{2.20}$$

where $\rho_{i\sigma}$ is the electron density of the ith spin σ-orbital. This $E_{\rm xc}^{\rm SIC}[\rho_\uparrow, \rho_\downarrow]$, which can effectively remove the self-interaction contribution, however, leads to different potentials for different orbitals [64]. So the wave functions for different orbitals are not orthogonal and orthogonalization is required.

Another promising approach is the OEP scheme [68, 69], in which one uses the HF exchange-only energy functional

$$E_{\rm xc}^{\rm HF} = -\frac{1}{2} \sum_{ij\sigma} \int\int \frac{\phi_{i\sigma}^*(\boldsymbol{r})\phi_{i\sigma}(\boldsymbol{r}')\phi_{j\sigma}^*(\boldsymbol{r}')\phi_{j\sigma}(\boldsymbol{r})}{|\boldsymbol{r}-\boldsymbol{r}'|} d\boldsymbol{r} d\boldsymbol{r}'. \tag{2.21}$$

In the one-electron limit, this functional can cancel out with the third term in Eq. (2.19), and therefore is self-interaction-free. To make use of this orbital-dependent (not density-dependent) functional in a DFT approach, it was proposed [69] to choose a one-electron effective potential $V_\sigma^{\rm OEP}(\boldsymbol{r})$ such that it can minimize the total-energy functional, i.e.,

$$\frac{\delta E^{\rm OEP}[\{\phi_{i\uparrow}, \phi_{j\downarrow}\}]}{\delta V_\sigma^{\rm OEP}(\boldsymbol{r})} = 0, \tag{2.22}$$

which can be converted to an integral equation and then solved together with Eq. (2.18). While the physical idea of the OEP method is simple, its computational implementation is quite difficult

due to the integral equation derived from Eq. (2.22). Krieger, Li, and Iafrate [65–67] suggested an approximative procedure to circumvent this difficulty, in which the OEP $V_\sigma^{\rm OEP}(\boldsymbol{r})$ is determined by solving linear equations instead of the complicated integral equation.

In the KLI approach, the exchange-correlation potential is shown to be

$$V_{{\rm xc}\sigma}^{\rm KLI}(\boldsymbol{r}) = \sum_i \frac{\rho_{i\sigma}(\boldsymbol{r})}{\rho_\sigma(\boldsymbol{r})} v_{{\rm xc}i\sigma}(\boldsymbol{r}) + \sum_{i\neq m} \frac{\rho_{i\sigma}(\boldsymbol{r})}{\rho_\sigma(\boldsymbol{r})} (\overline{V}_{{\rm xc}i\sigma}^{\rm KLI} - \overline{v}_{{\rm xc}i\sigma}), \tag{2.23}$$

where

$$v_{{\rm xc}i\sigma}(\boldsymbol{r}) = \frac{\delta E_{\rm xc}[\phi_{i\sigma}]}{\phi_{i\sigma}\delta\phi_{i\sigma}^*} = -\frac{1}{\phi_{i\sigma}(\boldsymbol{r})} \sum_j \int \frac{\phi_{i\sigma}(\boldsymbol{r}')\phi_{j\sigma}^*(\boldsymbol{r}')\phi_{j\sigma}(\boldsymbol{r})}{|\boldsymbol{r}-\boldsymbol{r}'|} d\boldsymbol{r}', \tag{2.24}$$

$$\overline{V}_{{\rm xc}i\sigma}^{\rm KLI} = \langle \phi_{i\sigma} | V_{{\rm xc}\sigma}^{\rm KLI}(\boldsymbol{r}) | \phi_{i\sigma} \rangle, \tag{2.25}$$

$$\overline{v}_{{\rm xc}i\sigma} = \langle \phi_{i\sigma} | v_{{\rm xc}i\sigma}(\boldsymbol{r}) | \phi_{i\sigma} \rangle, \tag{2.26}$$

and the second summation in Eq. (2.23) does not include the highest-occupied orbital $m\sigma$. The term of $\overline{V}_{{\rm xc}i\sigma}^{\rm KLI} - \overline{v}_{{\rm xc}i\sigma}$ can be obtained by solving the following linear equations

$$\sum_{i=1}^{N_\sigma - 1} (\delta_{ji} - (M_\sigma)_{ji})(\overline{V}_{{\rm xc}i\sigma}^{\rm KLI} - \overline{v}_{{\rm xc}i\sigma}) = \overline{V}_{{\rm xc}j\sigma}^{\rm S} - \overline{v}_{{\rm xc}j\sigma}, \tag{2.27}$$

where

$$(M_\sigma)_{ji} = \int \frac{\rho_{j\sigma}(\boldsymbol{r})\rho_{i\sigma}(\boldsymbol{r})}{\rho_\sigma(\boldsymbol{r})} d\boldsymbol{r}, \tag{2.28}$$

and

$$\overline{V}_{{\rm xc}j\sigma}^{\rm S} = \langle \phi_{j\sigma} | \sum_{i=1}^{N_\sigma} \frac{\rho_{i\sigma}(\boldsymbol{r}) v_{{\rm xc}i\sigma}(\boldsymbol{r})}{\rho_\sigma(\boldsymbol{r})} | \phi_{j\sigma} \rangle. \tag{2.29}$$

At the time of the development of the KLI method, the HF nonlocal exchange-only functional in Eq. (2.21) was used. This functional is accurate for the exchange part of $E_{\rm xc}$, but is computationally more expensive than the DFT $E_{\rm xc}$'s, such as LSDA. Thus, in some reference papers [67, 70] it has been suggested to use a combined version of the KLI method and the SIC method. It completely follows the KLI procedure, while the only change is that, at the step of Eq. (2.24), one uses the self-interaction-free $E_{\rm xc}$ in Eq. (2.20) rather than that in Eq. (2.21). For the widely-used simple LSDA functional [63], Eq. (2.24) then yields

$$v_{{\rm xc}i\sigma}(\boldsymbol{r}) = \left(\frac{6}{\pi}\right)^{1/3} \{-[\rho_\sigma(\boldsymbol{r})]^{1/3} + [\rho_{i\sigma}(\boldsymbol{r})]^{1/3}\} - \int \frac{\rho_{i\sigma}(\boldsymbol{r}')}{|\boldsymbol{r}-\boldsymbol{r}'|} d\boldsymbol{r}'. \tag{2.30}$$

This new KLI-SIC scheme is self-interaction-free, orbital-independent, and computationally not expensive. The improvement on computational efficiency becomes particularly important when a time-dependent process is considered, in which one needs to reconstruct the SAE at each time step.

As a summary of the two methods to generate a SAE potential, we compare eigenenergies of different orbitals obtained using different methods for a neon atom in Table 2.1, in which the experimental eigenenergies from Ref. [60] serve as reference. We see that, for outer-shell orbitals, the KLI-SIC method with the LSDA functional gives best results, while the PA method performs best for the inner-shell orbital. Furthermore, it appears that all methods can give a reasonable result for the inner-shell orbital. Therefore, it is usually a good choice to use the KLI-SIC method if electrons from many orbitals participate in the process of interest. For some atoms, the SAE potential based on KLI-SIC is fitted to an analytical formula with several fitting parameters and these parameters are given in Ref. [71].

2.2 Numerical methods of solving time-dependent Schrödinger equation

To numerically simulate laser-matter interactions, we need to solve the TDSE

$$i\frac{\partial\Psi(\boldsymbol{r},t)}{\partial t} = \left[\hat{H}_0 + \hat{H}_I(t)\right]\Psi(\boldsymbol{r},t), \tag{2.31}$$

where $\boldsymbol{r}$ is the coordinate of the particle, $\hat{H}_0$ is the field-free Hamiltonian of the system, and $\hat{H}_I(t)$ describes the interaction of the system with the laser field. In the SAE approximation and using the length-gauge, this equation yields

$$i\frac{\partial\Psi(\boldsymbol{r},t)}{\partial t} = \left[\frac{\boldsymbol{p}^2}{2} + V(\boldsymbol{r}) + \boldsymbol{E}(t)\cdot\boldsymbol{r}\right]\Psi(\boldsymbol{r},t), \tag{2.32}$$

where $\boldsymbol{p} = -i\boldsymbol{\nabla}$ is the momentum operator, $V(\boldsymbol{r})$ is the SAE potential, and $\boldsymbol{E}(t)$ is the laser field. Using the standard Crank-Nicolson method [72], this second-order differential equation can be discretized on a grid in space and time and then numerically solved.

2.2.1 Propagation method

For a small time step Δt, the solution of Eq. (2.31) can be approximated as

$$\Psi(t+\Delta t) \simeq e^{-i\hat{H}(t)\Delta t}\Psi(t) \simeq \frac{1-i\frac{\Delta t}{2}\hat{H}(t)}{1+i\frac{\Delta t}{2}\hat{H}(t)}\Psi(t), \tag{2.33}$$

where the Cayley unitary transformation [73] is used in the second step in order to preserve the norm of the wave function. This equation can be further written as

$$\left(1+i\frac{\Delta t}{2}\hat{H}(t)\right)\Psi(t+\Delta t) = \left(1-i\frac{\Delta t}{2}\hat{H}(t)\right)\Psi(t). \tag{2.34}$$

Moreover, the Hamiltonian $\hat{H}(t)$ can be decomposed into different coordinate directions, where each component is a one-dimensional (1D) Hamiltonian given by

$$\hat{H}_x(t) = A(x,y,t)\frac{\partial^2}{\partial x^2} + B(x,y,t)\frac{\partial}{\partial x} + V(x,y,t), \tag{2.35}$$

where x is the coordinate of interest and y stands for all the other coordinates. Discretizing this 1D Hamiltonian using the second-order central scheme, Eq. (2.34) yields

$$\begin{aligned}
&\Psi_n(t+\Delta t) + i\frac{\Delta t}{2}\left(A_n(t)\frac{\Psi_{n+1}(t+\Delta t) - 2\Psi_n(t+\Delta t) + \Psi_{n-1}(t+\Delta t)}{(\Delta x)^2}\right.\\
&\left.+B_n(t)\frac{\Psi_{n+1}(t+\Delta t) - \Psi_{n-1}(t+\Delta t)}{2\Delta x} + V_n(t)\Psi_n(t+\Delta t)\right)\\
&= \Psi_n(t) - i\frac{\Delta t}{2}\left(A_n(t)\frac{\Psi_{n+1}(t) - 2\Psi_n(t) + \Psi_{n-1}(t)}{(\Delta x)^2} + B_n(t)\frac{\Psi_{n+1}(t) - \Psi_{n-1}(t)}{2\Delta x} + V_n(t)\Psi_n(t)\right),
\end{aligned} \tag{2.36}$$

where n represents the grid point (x_n, y) in the discretized space grid. It is not difficult to show that this equation leads to the following system of linear equations:

$$\begin{pmatrix} {}_2X_1 & {}_3X_1 & 0 & 0 & \cdots & 0 & 0 & 0 \\ {}_1X_2 & {}_2X_2 & {}_3X_2 & 0 & \cdots & 0 & 0 & 0 \\ 0 & {}_1X_3 & {}_2X_3 & {}_3X_3 & \cdots & 0 & 0 & 0 \\ \vdots & \vdots & \vdots & \vdots & \ddots & \vdots & \vdots & \vdots \\ 0 & 0 & 0 & 0 & \cdots & {}_1X_{N-1} & {}_2X_{N-1} & {}_3X_{N-1} \\ 0 & 0 & 0 & 0 & \cdots & 0 & {}_1X_N & {}_2X_N \end{pmatrix} \begin{pmatrix} \Psi_1(t+\Delta t) \\ \Psi_2(t+\Delta t) \\ \Psi_3(t+\Delta t) \\ \vdots \\ \Psi_{N-1}(t+\Delta t) \\ \Psi_N(t+\Delta t) \end{pmatrix}$$

$$= \tag{2.37}$$

$$\begin{pmatrix} {}_2Y_1 & {}_3Y_1 & 0 & 0 & \cdots & 0 & 0 & 0 \\ {}_1Y_2 & {}_2Y_2 & {}_3Y_2 & 0 & \cdots & 0 & 0 & 0 \\ 0 & {}_1Y_3 & {}_2Y_3 & {}_3Y_3 & \cdots & 0 & 0 & 0 \\ \vdots & \vdots & \vdots & \vdots & \ddots & \vdots & \vdots & \vdots \\ 0 & 0 & 0 & 0 & \cdots & {}_1Y_{N-1} & {}_2Y_{N-1} & {}_3Y_{N-1} \\ 0 & 0 & 0 & 0 & \cdots & 0 & {}_1Y_N & {}_2Y_N \end{pmatrix} \begin{pmatrix} \Psi_1(t) \\ \Psi_2(t) \\ \Psi_3(t) \\ \vdots \\ \Psi_{N-1}(t) \\ \Psi_N(t) \end{pmatrix},$$

where N is the total number of grid points in x direction and

$$ {}_1X_n = \frac{i\Delta t}{2(\Delta x)^2} A_n(t) - \frac{i\Delta t}{4\Delta x} B_n(t), \tag{2.38}$$

$$ {}_2X_n = 1 - \frac{i\Delta t}{(\Delta x)^2} A_n(t) + \frac{i\Delta t}{2} V_n(t), \tag{2.39}$$

$$ {}_3X_n = \frac{i\Delta t}{2(\Delta x)^2} A_n(t) + \frac{i\Delta t}{4\Delta x} B_n(t), \tag{2.40}$$

$$ {}_1Y_n = -\frac{i\Delta t}{2(\Delta x)^2} A_n(t) + \frac{i\Delta t}{4\Delta x} B_n(t), \tag{2.41}$$

$$ {}_2Y_n = 1 + \frac{i\Delta t}{(\Delta x)^2} A_n(t) - \frac{i\Delta t}{2} V_n(t), \tag{2.42}$$

$$ {}_3Y_n = -\frac{i\Delta t}{2(\Delta x)^2} A_n(t) - \frac{i\Delta t}{4\Delta x} B_n(t). \tag{2.43}$$

The matrix on the left side of Eq. (2.37) is tridiagonal and the linear equations can hence be solved by the typical LU decomposition method with a time complexity of $O(N \log N)$.

For a 2D Hamiltonian in (x, y) coordinates, it can be decomposed as

$$\hat{H}(t) = \hat{H}_x(t) + \hat{H}_y(t), \tag{2.44}$$

in which the mixing (x, y) terms are separated symmetrically. Then the wave function at time $t + \Delta t$ is given by

$$\begin{aligned} \Psi(t + \Delta t) &\simeq e^{-i[\hat{H}_x(t)+\hat{H}_y(t)]\Delta t}\Psi(t) \\ &\simeq e^{-i\hat{H}_y(t)\Delta t/2} e^{-i\hat{H}_x(t)\Delta t} e^{-i\hat{H}_y(t)\Delta t/2}\Psi(t), \end{aligned} \tag{2.45}$$

where in the second approximation the Baker-Campbell-Hausdorff formula [74] is used. This approximation can be shown to have an accuracy of $O(\Delta t^3)$. So, for obtaining the wave function $\Psi(t + \Delta t)$, we first propagate the wave function $\Psi(t)$ in y direction by a time step of $\Delta t/2$, then propagate the updated wave function $\Psi'(t)$ in x direction by Δt, and finally propagate again the further-updated wave function $\Psi''(t)$ in y direction by $\Delta t/2$. In each x- (or y-) direction propagation step, Eq. (2.37) is solved for all y (or x) values. The propagation in 3D case is similar

$$\begin{aligned} \Psi(t + \Delta t) &\simeq e^{-i[\hat{H}_x(t)+\hat{H}_y(t)+\hat{H}_z(t)]\Delta t}\Psi(t) \\ &\simeq e^{-i\hat{H}_z(t)\Delta t/2} e^{-i\hat{H}_y(t)\Delta t/2} e^{-i\hat{H}_x(t)\Delta t} e^{-i\hat{H}_y(t)\Delta t/2} e^{-i\hat{H}_z(t)\Delta t/2}\Psi(t), \end{aligned} \tag{2.46}$$

where the order of (x, y, z) does not matter as long as the symmetry of the propagator is preserved. The generalization to higher dimensions is straightforward and not limited to Cartesian coordinates.

2.2.2 Methods of obtaining initial states

We have reviewed the approach of propagating the wave function in time in the last subsection. However, before the start of the propagation, one needs to know the initial condition for the differential equation, which is usually one of the eigenstates of the system of interest. These eigenstates can be obtained by solving the boundary condition problem of the time-independent Schrödinger equation

$$\hat{H}_0\Psi(\boldsymbol{r}) = E\Psi(\boldsymbol{r}), \tag{2.47}$$

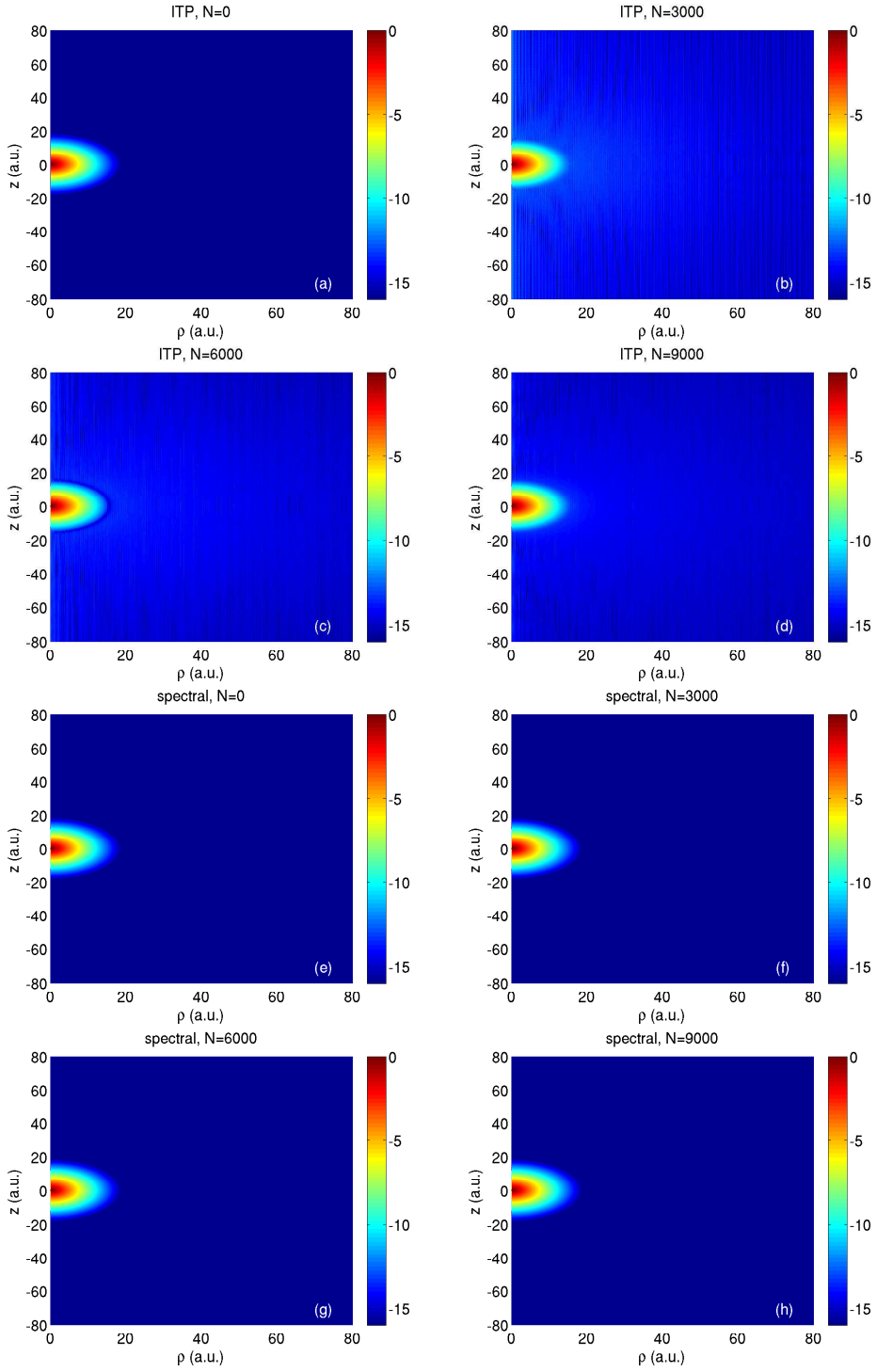

Figure 2.2: Comparison of eigenstates calculated from the ITP [(a)-(d)] and spectral [(e)-(h)] methods. We have considered a hydrogen atom in (ρ, z) coordinates. The field-free propagations of the 1s state are shown for four different propagation steps ($N = 0$, 3000, 6000, and 9000) with a time step of $\Delta t = 0.02$. When using the spectral method, the eigenenergies are obtained from the ITP calculations and then the eigenfunctions are evaluated from Eq. (2.59).

with certain boundary conditions [e.g., $\Psi(r=0)=\Psi(r=\infty)=0$ for 3D Coulomb potential]. For 1D systems, Eq. (2.47) can be solved easily with the typical diagonalization or shooting method, which may however become extremely slow and difficult for systems with higher dimensions. Fortunately, it has been shown that the imaginary time propagation (ITP) method and the spectral method are two very powerful and efficient tools to resolve this problem.

The idea of the ITP method is based on the propagation of a randomly-assumed wave function (usually a Gaussian wave packet for atoms) in the field-free Hamiltonian, i.e.,

$$i\frac{\partial\Psi(\boldsymbol{r},t)}{\partial t}=\hat{H}_0\Psi(\boldsymbol{r},t). \tag{2.48}$$

Expanding the wave function in the Hilbert space of $\hat{H}_0$, one obtains the time-dependent wavefunction $\Psi(\boldsymbol{r},t)$ as

$$\Psi(\boldsymbol{r},t)=\sum_j c_j\phi_j(\boldsymbol{r})e^{-iE_jt}, \tag{2.49}$$

where $\phi_j(\boldsymbol{r})$ is the jth eigenstate with energy E_j, and c_j is the projection coefficient of $\Psi(\boldsymbol{r},t=0)$ on $\phi_j(\boldsymbol{r})$. If we do an imaginary time propagation instead of the real time evolution, i.e., $t\rightarrow -it'$, the wave function after N steps of propagations becomes

$$\Psi(\boldsymbol{r},t=N\Delta t)=\sum_j c_j\phi_j(\boldsymbol{r})e^{-E_jN\Delta t}. \tag{2.50}$$

When N is large enough, all the other terms are negligible small as compared to the first term, which can be seen from

$$\frac{c_je^{-E_jN\Delta t}}{c_0e^{-E_0N\Delta t}}=(c_j/c_0)e^{(E_0-E_j)N\Delta t}\rightarrow 0. \tag{2.51}$$

Therefore, the ground state is given by

$$\phi_0(\boldsymbol{r})=\Psi'(\boldsymbol{r},t=N\Delta t), \tag{2.52}$$

where $\Psi'(\boldsymbol{r},t=N\Delta t)$ here denotes the normalized wave function. The excited states can be obtained with the same idea, while the only modification is that those states that are lower in energy than the calculated state need to be projected out at every propagation step. For degenerate states, one has to use the symmetry of the wave function to distinguish them, which can be done

by using only half of the grid in the imaginary time propagation. As an example, for the 1s state of an atom, it has a symmetry of $\Psi(\rho, z) = \Psi(\rho, -z)$ in the (ρ, z) coordinates. We hence only use the half grid with $\rho \geqslant 0$ and $z \geqslant 0$, and set the first- and second-order derivatives at $z = 0$ according to the symmetry, i.e., $\Psi'(z = 0) = 0$ and $\Psi''(z = 0) = 2[\Psi(\Delta z) - \Psi(z = 0)]/\Delta z^2$.

The ITP method is easy to implement and the resulting eigenfunctions work well for most of our simulations. However, for some calculations, especially when excited states are involved, its accuracy is not ideal. This is due to the error accumulation in the calculation since the higher states are calculated based on the lower states. Moreover, when two states have close eigenenergies but are not degenerate, this method converges very slowly and its accuracy is also questionable. Even for a ground state, we clearly see some probability flux emerging during the field-free propagation of the initial states calculated using ITP [see Fig. 2.2(b)-(d)], when the background probability is chosen to be small (e.g., 10^{-16} in Fig. 2.2). We therefore like to introduce another method called spectral method to improve the eigenfunctions for some high-precision calculations.

The spectral method [75] is also based on the propagation of an initially-guessed wave function. Let us define a correlation function $C(t)$ as

$$C(t) = \langle \Psi(\boldsymbol{r}, t = 0) | \Psi(\boldsymbol{r}, t) \rangle = \int \Psi^*(\boldsymbol{r}, t = 0) \Psi(\boldsymbol{r}, t) d\boldsymbol{r}, \tag{2.53}$$

which can be further reduced to

$$C(t) = \sum_j |c_j|^2 e^{-iE_j t}, \tag{2.54}$$

using Eq. (2.49). The Fourier transform of this equation is

$$\widetilde{C}(E) = \sum_j |c_j|^2 \delta(E - E_j), \tag{2.55}$$

from which the eigenenergies E_j can be obtained from the peaks of this spectrum. With a known E_j, the eigenfunction can be reconstructed from

$$\phi_j(\boldsymbol{r}) = a \int_{-\infty}^{\infty} \Psi(\boldsymbol{r}, t) e^{iE_j t} dt, \tag{2.56}$$

where a is determined by normalization. In practice, integrating to infinity is impossible, so the

following window function

$$w(t) = \begin{cases} 1 - \cos(2\pi t/T), & \text{if } 0 \leqslant t \leqslant T, \\ 0, & \text{if } t > T, \end{cases} \tag{2.57}$$

is suggested to keep the integration within the region $(0, T)$, with T being the total propagation time. We thus have

$$\widetilde{C}(E) = \frac{1}{T} \int_0^T C(t) w(t) dt, \tag{2.58}$$

and

$$\phi_j(\boldsymbol{r}) = \frac{a}{T} \int_0^T \Psi(\boldsymbol{r}, t) w(t) e^{iE_j t} dt, \tag{2.59}$$

which both can be numerically evaluated easily.

To efficiently make use of Eq. (2.59), one needs very accurate eigenenergies (e.g., at least with an accuracy of 10^{-6} a.u.), which however may be not easy to extract from the correlation spectrum calculated from Eq. (2.58) in simulations. Our numerical experience shows that the eigenenergies calculated from the ITP method are usually very accurate and well beyond our requirement of using Eq. (2.59). We therefore propose a combined scheme of the ITP and the spectral methods, in which we use the ITP method to calculate the eigenenergies and then obtain the wave functions from the spectral method using Eq. (2.59). Results in Fig. 2.2 [(e)-(h)] show that the quality of the eigenstate is greatly improved using this combined scheme.

2.2.3 Absorbing boundaries

During laser-matter interactions, ionization is the most general consequence and also contains a lot of useful and significant information about the system. To simulate ionization processes, we always need to propagate the ionizing wave packet, i.e., the outgoing ionization probability, on our numerical grid. Usually such a wave packet has a momentum in the outgoing direction, finally it will hence hit and be reflected by the boundaries of our grid, if no boundary conditions are used. Such a reflection will cause some artificial physical processes, such as the interference with an outgoing wave packet that approaches the boundary at a later time, and therefore needs to

be eliminated. While there exists many different carefully-designed boundary conditions that can solve this problem, we introduce two most-widely used ones: the masking function method and the exterior complex scaling (ECS) method.

In the masking function method one simply multiplies the wave function by a cosine-based function that smoothly decays from 1 to 0 in the absorbing region. Considering the 1D case, this method gives

$$\Psi(x) = \Psi(x) f_{\text{mask}}(x) = \Psi(x) \cos^{\alpha}(\frac{\pi}{2} \frac{x - x_0}{x_1 - x_0}), \tag{2.60}$$

where x_0 and x_1 are the starting and ending points of the absorbing region ($x_0 < x < x_1$), respectively, and α is a coefficient selected depending on the specific problem. The masking function boundary is easy to code and works well for most cases, especially for those problems where a little reflection is allowed to occur.

To suppress the reflection to an even lower level, one can use the ECS method ([76] and references therein), in which an exponentially decaying term in the propagator can absorb the outgoing flux, if a complex coordinate axis is artificially assumed in the absorbing region as

$$x = x_0 + (x - x_0) e^{i\eta}. \tag{2.61}$$

Here, η is the scaling angle with $0 < \eta < \pi/2$, and we have again simplified our model to 1D and assumed that x_0 is the starting point of the absorbing boundary. Under these assumptions and together with the length-gauge, the solution of the reduced 1D TDSE from Eq. (2.32) in the absorbing region yields

$$\begin{aligned} \Psi(t + \Delta t) &= e^{-i[\hat{p}^2/2 + V_0(x) + E(t)x]\Delta t} \Psi(t) \\ &= e^{-i \cos(2\eta) \hat{p}^2 \Delta t/2} e^{-\sin(2\eta) \hat{p}^2 \Delta t/2} e^{-iV_0(x)\Delta t} e^{-iE(t)[x_0 + (x - x_0)e^{i\eta}]\Delta t} \Psi(t), \end{aligned} \tag{2.62}$$

with the potential term $V_0(x)$ untransformed in this region and

$$e^{-iE(t)[x_0 + (x - x_0)e^{i\eta}]\Delta t} = e^{-iE(t)[x_0 + (x - x_0)\cos\eta]\Delta t} e^{E(t)[x_0 + (x - x_0)\sin\eta]\Delta t}. \tag{2.63}$$

It is now clear that the second exponential term in the second row of Eq. (2.62) decays exponentially and hence can absorb the outgoing probability that enters the boundary region. However, one may

note that the second exponential term on the right-hand side of Eq. (2.63) may become an undesired source when the sign of the laser field $E(t)$ is positive. In some extreme conditions, this term may cause the wave function to explode and therefore induce numerical problems. He *et al.* [76] hence suggested to drop the $e^{i\eta}$ term in Eq. (2.63), i.e., to do the propagation using

$$\Psi(t+\Delta t) = e^{-i\cos(2\eta)\hat{p}^2\Delta t/2} e^{-\sin(2\eta)\hat{p}^2\Delta t/2} e^{-iV_0(x)\Delta t} e^{-iE(t)x\Delta t}\Psi(t), \tag{2.64}$$

which means the untransformed standard field coupling is used over the entire grid including the absorbing region. This simple modification of the traditional ECS method has been shown to strongly absorb the outgoing flux without any undesired explosion and also effectively suppress reflections as compared to the masking function method [76].

Chapter 3

Time Delays in Single-Photon Ionization

Due to the great advances in the development in laser technologies, nowadays we are able to use attosecond XUV pulses to observe, study, and even control electron dynamics in atoms and molecules on their intrinsic time scale [1]. As an important application, the time information of XUV-induced single-photon ionization has been extracted using the attosecond streak camera [2, 3] as well as the RABITT technique [4]. A substantial time delay (a few tens of attoseconds) between ionization from different orbitals has been reported in both neon [3] and argon [4] atoms, and therefore initiated a lot of theoretical interest in interpreting the physical origin of such a time delay. In this chapter, we want to contribute to this debate by exploring this problem from several different perspectives and finally giving our understanding of this photoionization time delay. In section 3.1, we introduce a new numerical method of calculating the Wigner-Smith (WS) time delay in the photoionization process using its fundamental definition from a time-dependent perspective. In section 3.2, we turn to the experimental measurement of the streaking time delay and systematically study problems related to the streaking experiment, including the physical interpretation of the streaking time delay, the finite-range property of this delay and its application to imaging, as well as the influence of pedestal and additional static field on this delay.

3.1 Calculation of Wigner-Smith-like time delays from a time-dependent perspective[1]

In this section, we propose a time-dependent theoretical approach to calculate time delays in photoionization, which not only is more general for different cases (e.g., short- and long-range potentials) but also provides more information about the process than the traditional time-independent methods. This new numerical method is based on the fundamental definition of a time delay and realized using the back-propagation technique. The time delays calculated using this new method are then compared with those from the traditional methods, namely, the phase derivative method and the trajectory method. We also apply this method to study the influence of the parameters of the XUV pulse in the XUV photoionization process as well as the parameters of an additional laser pulse in the laser-assisted photoionization on the time delay.

3.1.1 Wigner-Smith time delay

The Wigner-Smith (WS) time delay concept was originally introduced and developed for a scattering process [40, 41]. It is defined to be the difference between the time $t_p(R)$ a particle spends in a certain region R of a potential and the time $t_0(R)$ that a free particle spends in the same region without the presence of the potential (Fig. 3.1). Since a scattering process usually starts and ends far away from the scattering center, one requires that the region R extends to infinity in the definition of the WS time delay and therefore mathematically the WS time delay is given by

$$\Delta t_{\mathrm{WS}} = t_p(R) - t_0(R)|_{R\to\infty}. \tag{3.1}$$

For scattering in a short-range potential, the WS time delay is related to the scattering phase shift φ by

$$\Delta t_{\mathrm{WS}} = \frac{d\varphi}{dE}. \tag{3.2}$$

[1] The results of this section are presented in J. Su, H. Ni, A. Becker, and A. Jaroń-Becker, Phys. Rev. A **87**, 033420 (2013) and J. Su, H. Ni, A. Becker, and A. Jaroń-Becker, J. Mod. Opt. **60**, 1484 (2013).

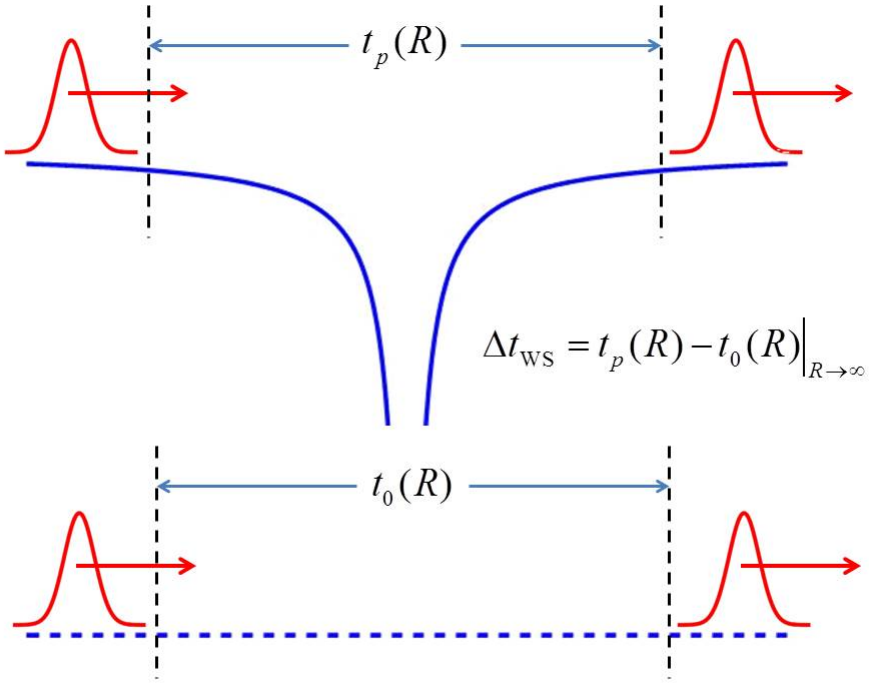

Figure 3.1: Schematic diagram for the WS time delay in a scattering scenario. The WS time delay Δt_{WS} is defined as the difference of two times: one is the time $t_p(R)$ a particle (or wave packet) spends in region R within the potential (upper row), the other one is the time $t_0(R)$ that a free particle spends in the same region R without the presence of the potential (lower row), as the region R extends to infinity, i.e., $\Delta t_{\mathrm{WS}} = t_p(R) - t_0(R)|_{R\to\infty}$.

Wigner [40] has given a beautiful derivation of Eq. (3.2) by using a superposition of two monoenergetic beams of slightly different energies as a substitute for a wave packet. Here, alternatively, we derive this formula by employing a wave packet analysis. To make our derivation simple but without losing the central physical idea, we restrict the motion of the particle along the x direction, i.e., considering a 1D scattering process. As initial condition, we assume that a particle is propagating towards a short-range potential $V(x)$ from $x = -\infty$, given by the following incident wave function

$$\Psi(x,t) = \int A(k) e^{i(kx - Et)} dk, \tag{3.3}$$

where k is the momentum and $E = k^2/2$. To obtain the classical trajectory of the incident particle, one uses the stationary phase approximation. According to this approximation, the rapid phase variation in Eq. (3.3) will generally lead to destructive interference so that the integral is determined by the point where the phase is stationary

$$\frac{d}{dE}(kx - Et) = \frac{x}{k} - t = 0, \tag{3.4}$$

which further reduces to a trajectory as

$$t = \frac{x}{k}. \tag{3.5}$$

After the particle passes through the potential, the wave function of the particle at $x = \infty$ can be expressed by

$$\Psi(x,t) = \int A(k) e^{i[kx - Et + \varphi(E)]} dk, \tag{3.6}$$

where $\varphi(E)$ is the scattering phase shift. Using the stationary phase analysis again, one obtains the trajectory of the outgoing particle after the scattering as

$$t = \frac{x}{k} + \frac{d\varphi(E)}{dE}. \tag{3.7}$$

According to its original definition, the WS time delay is the delay the particle accumulates during its propagation in the scattering potential as compared to a freely-propagating particle. It is obvious that Eqs. (3.7) and (3.5) describe the motions of the scattering and the corresponding free particles

respectively, and therefore the WS time delay associated with this scattering process is $\frac{d\varphi(E)}{dE}$ by comparing these two trajectories. While the above derivation for the WS time delay is based on a 1D assumption, one can generalize this procedure and show that Eq. (3.2) is also true for a more general 3D case, for which a detailed discussion can be found e.g. in Ref. [77]. Due to the fact that a photoionization process is a half scattering process, the application of the WS time delay formula for a photoionization process is straightforward: its WS time delay is $\frac{1}{2}\frac{d\varphi(E)}{dE}$, where again $\varphi(E)$ is the phase shift for the complete scattering process.

One may note that the above derivation for the WS time delay does not hold for a long-range potential, because the outgoing wave function of the particle can not simply be expressed by Eq. (3.6), which is derived by assuming the potential vanishes quickly enough when $x \to \infty$. For long-range potentials, usually there are more terms in the phase of the scattered wave function. As an example, for the Coulomb potential, there exists a logarithmic phase term of the form $(1/k)\ln(2kr)$. Consequently, the time delay is not only position dependent but also diverges when $r \to \infty$, which we will later discuss in detail.

The above method of calculating the WS time delay, i.e., using Eq. (3.2), is simple and not difficult to evaluate for a photoionization process. However, such a method has a few drawbacks: On the one hand, the WS time delay calculated via Eq. (3.2) for a short-range potential only gives one time delay value for an ultrafast process, which is time-independent and does not allow a time-dependent analysis of the process. On the other hand, such a method cannot be applied to long-range potentials such as the Coulomb potential, which exists in all atoms and molecules. As an alternative, it has been proposed (e.g., [37, 38, 44]) to still employ Eq. (3.2) to calculate the WS time delay by using the Coulomb scattering phase shift. Such an idea however does not match the original definition of the WS time delay and only accounts for the short-range part of the total potential. Moreover, for a given problem it is not always obvious how one should separate the full potential into a short-range and a long-range part.

We therefore seek for an alternative time-dependent theoretical approach to calculate time delays in photoionization, which addresses some of the concerns regarding the WS time delay and

its determination. We further attempt to apply such an approach in time-dependent numerical grid simulations, which are known to be a powerful tool in calculating and analyzing processes on an ultrashort time scale. The present theoretical analysis of a time delay is intended to be general and not focused, in particular, on the recent streaking experiments. Once formulated, tested and established this may turn out in future as a useful step towards understanding the physics of time delays in streaking experiments and other precise measurements of ultrashort time scales.

Our proposal is based on the quantum mechanical expression for the time a particle spends inside a certain region R of a potential. By comparing this time to the corresponding time for a free particle, a time delay is given, which is well-defined for any finite region. To the best of our knowledge, this fundamental definition of a time delay has not been applied in the analysis of time-dependent processes initiated or driven by ultrashort laser pulses. It however offers a few interesting features: First, for any finite region R the time delay is well-defined for any physical relevant potential and independent whether or not the limit for an extension of the region towards infinity exists. This enables a theoretical analysis in particular for long-range potentials without any restriction of the potential. Second, in the limit to infinity, if well-defined, the time delay should converge to the WS delay. Third, the time delay can be determined as a function of time after the emission of the photoelectron even during its interaction with some other external fields such as the IR field present in the streaking experiment. This expands the options for a theoretical analysis of ultrashort time-dependent processes. Fourth, there is no a-priori separation of short- and long-range parts in the potential necessary and the influence of both contributions can be studied.

3.1.2 Theoretical method and back-propagation technique

For a particle in a given normalized state $\Psi(\boldsymbol{r}, t)$, the time it spends inside a region R of a potential $V(\boldsymbol{r})$ can be expressed as [78]

$$t_{\Psi,R} = \int_{-\infty}^{\infty} dt \int_R d\boldsymbol{r} |\Psi(\boldsymbol{r}, t)|^2. \tag{3.8}$$

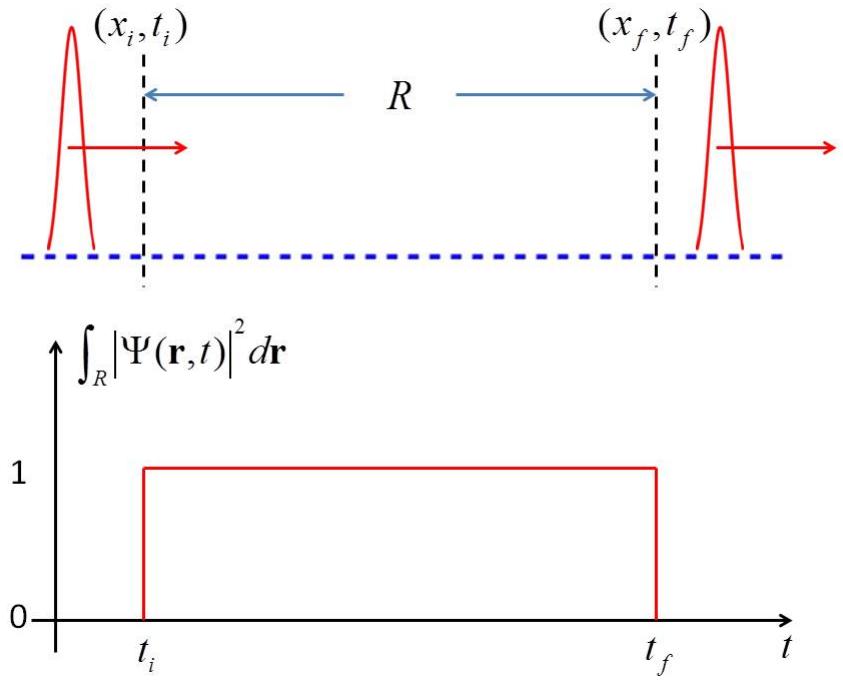

Figure 3.2: Schematic diagram for understanding Eq. (3.8). We consider a normalized delta wave packet that enters the region R at instant t_i and leaves R at t_f. In the lower panel we plot the probability to find the wave packet in the region R, i.e., $\int_R |\Psi(\boldsymbol{r},t)|^2 d\boldsymbol{r}$, as a function of time. Eq. (3.8) calculates the area of the red rectangular region, i.e., $S_{\rm red} = (t_f - t_i) \times 1 = t_f - t_i$, which is essentially the time the wave packet spends in the region R.

In order to understand this interpretation, we consider a normalized delta wave function that enters the left side of the region R (i.e., $[x_i, x_f]$) at instant t_i and then leaves the right side at t_f (see Fig. 3.2). One may note that the inner integration in Eq. (3.8), i.e., $\int_R |\Psi(\boldsymbol{r},t)|^2 d\boldsymbol{r}$, is equal to the probability to find the wave packet in the region R. Since the wave packet is in the region R only during the time interval $[t_i, t_f]$, the result of the inner integration is always zero at other times. Therefore the double integration in Eq. (3.8) can be determined by the area of the red rectangular region that is

$$t_{\Psi,R} = S_{\text{red}} = (t_f - t_i) \times 1 = t_f - t_i. \tag{3.9}$$

This is just the time the wave packet spends in the region R. One major advantage of this time formula is that it does not require time information about when the wave packet enters and leaves the region R, as long as the wave packet is initially outside this region. Such a property may become useful for calculating times when the start and end points for a process of interest are not available. One may also notice that for such an application the probability needs to be 1 when the wave packet is in the region R. Thus one needs to normalize the wave packet when making use of this formula.

While $t_{\Psi,R}$ is, in general, finite for finite regions and any $\Psi(\boldsymbol{r},t)$, it is useful to compare $t_{\Psi,R}$ to the time spent by a free particle in R (or another reference time):

$$t_{\Psi^{(0)},R} = \int_{-\infty}^{\infty} dt \int_R d\boldsymbol{r} |\Psi^{(0)}(\boldsymbol{r},t)|^2. \tag{3.10}$$

Here, $\Psi^{(0)}(\boldsymbol{r},t)$ is the free particle state corresponding to $\Psi(\boldsymbol{r},t)$. The difference between $t_{\Psi,R}$ and $t_{\Psi^{(0)},R}$ defines the time delay associated with $\Psi(\boldsymbol{r},t)$, the region R, and the potential $V(\boldsymbol{r})$

$$\Delta t_{\Psi,R} = t_{\Psi,R} - t_{\Psi^{(0)},R}. \tag{3.11}$$

Similar to the WS time delay, the quantity $\Delta t_{\Psi,R}$ should have a finite limit as the radius of R grows to infinity if the interaction vanishes quickly enough. Thus, $\Delta t_{\Psi,R\to\infty}$ and the associated quantum mechanical operator are well-defined for short-range potentials $V(\boldsymbol{r})$ only.

The above definition provides a useful concept to calculate time delays in time-dependent processes, in particular on an ultrashort time scale. While it is known as the basis for deriving a

time delay in scattering scenarios, it has not been applied for the theoretical analysis of processes initiated or driven by ultrashort intense laser pulses. We thus intend to apply this method to obtain time delays for a photoionization process in our numerical simulations. Physically, we are interested in the time that an initially-bounded electron needs to leave a certain region (centered about the position of the nucleus) following ionization due to the absorption of an XUV photon. To this end, we note that the expressions above can be readily applied to a photoelectron described by the continuum wave function $\Psi_i^{(\mathrm{ion})}(\boldsymbol{r},t)$ in our adoption of Eq. (3.8)

$$t_{\Psi_i,R} = \frac{1}{P_{\mathrm{ion}}} \int_{-\infty}^{\infty} dt \int_R d\boldsymbol{r} |\Psi_i^{(\mathrm{ion})}(\boldsymbol{r},t)|^2, \tag{3.12}$$

where $\Psi_i^{(\mathrm{ion})}(\boldsymbol{r},t)$ is normalized by the ionization probability

$$P_{\mathrm{ion}} = \int_{-\infty}^{\infty} d\boldsymbol{r} |\Psi_i^{(\mathrm{ion})}(\boldsymbol{r},t\to\infty)|^2. \tag{3.13}$$

We can then define the time delay associated with the ionization from a specific initial state analogous to Eq. (3.11) as

$$\Delta t_{\Psi_i,R} = t_{\Psi_i,R} - t_{\Psi_i^{(0)},R}, \tag{3.14}$$

where $\Psi_i^{(0)}(\boldsymbol{r},t)$ is the free-particle state corresponding to the continuum wave function after transition from the initial state $\Psi_i(\boldsymbol{r},t=0)$. According to this definition, we expect negative values for the time delays, since a free wave packet should spend more time in a given region R than the corresponding wave packet that has the same asymptotic momentum propagating in an attractive potential. We also consider the difference in the time delays for the ionization from two different initial states $\Psi_i(\boldsymbol{r},t=0)$ and $\Psi_j(\boldsymbol{r},t=0)$ as

$$\Delta T(\Psi_i,\Psi_j;R) = \Delta t_{\Psi_i,R} - \Delta t_{\Psi_j,R}. \tag{3.15}$$

In order to use the above definitions in a numerical simulation of a photoionization process, we need to identify the ionizing part of the wave function $\Psi_i^{(\mathrm{ion})}(\boldsymbol{r},t)$ as well as the corresponding free particle state $\Psi_i^{(0)}(\boldsymbol{r},t)$. Moreover, to make use of Eq. (3.14) correctly, one needs to know the time of ionization. Otherwise, for a wave function that is initially bound in region R, integrating the

time from $-\infty$ to ∞ using Eq. (3.14) results with an infinite value. However, in traditional TDSE simulations, it is not straightforward to obtain either the time of ionization or the form of the wave packet after the transition into the continuum. Moreover, the information of the corresponding free particle state is not available in the simulations either. It hence appears to be difficult to make use of Eq. (3.14) in our calculations directly. We circumvent this obstacle by using the following back-propagation technique.

We first solve the TDSE of the system, initially in the state $\Psi_i(\boldsymbol{r}, t = 0)$, under the interaction with the external XUV field on a space-time grid:

$$i\frac{\partial}{\partial t}\Psi(\boldsymbol{r}, t) = \left[\frac{\boldsymbol{p}^2}{2} + V(\boldsymbol{r}) + V_{\text{light}}(\boldsymbol{r}, t)\right]\Psi(\boldsymbol{r}, t), \tag{3.16}$$

where $\boldsymbol{p}$ is the momentum operator, $V(\boldsymbol{r})$ is the field-free potential of the system, and $V_{\text{light}}(t)$ represents the interaction with the ionizing light field. After the end of the interaction with the light field we separate the ionizing part of the wavefunction from the remaining bound parts, either via projection onto analytically or numerically known states or via spatial separation of the ionizing part at large distances on the grid. After removal of the bound parts we propagate the remaining ionizing part of the wave function backwards in time without taking account of the interaction with the light field using two different Hamiltonians, once including the potential $V(\boldsymbol{r})$ as

$$i\frac{\partial}{\partial t}\Psi_i^{(\text{ion})}(\boldsymbol{r}, t) = \left[\frac{\boldsymbol{p}^2}{2} + V(\boldsymbol{r})\right]\Psi_i^{(\text{ion})}(\boldsymbol{r}, t), \tag{3.17}$$

and once as a free particle

$$i\frac{\partial}{\partial t}\Psi_i^{(0)}(\boldsymbol{r}, t) = \frac{\boldsymbol{p}^2}{2}\Psi_i^{(0)}(\boldsymbol{r}, t). \tag{3.18}$$

In order to calculate the time delay $\Delta t_{\Psi_i,R}$ for a given region R, the wavepacket has to be located outside of R at the start of the back-propagation and the propagation needs to be terminated as the wave packet reaches the center of R, i.e., the location of the residual target ion. The latter point will be further discussed in the application of the method below.

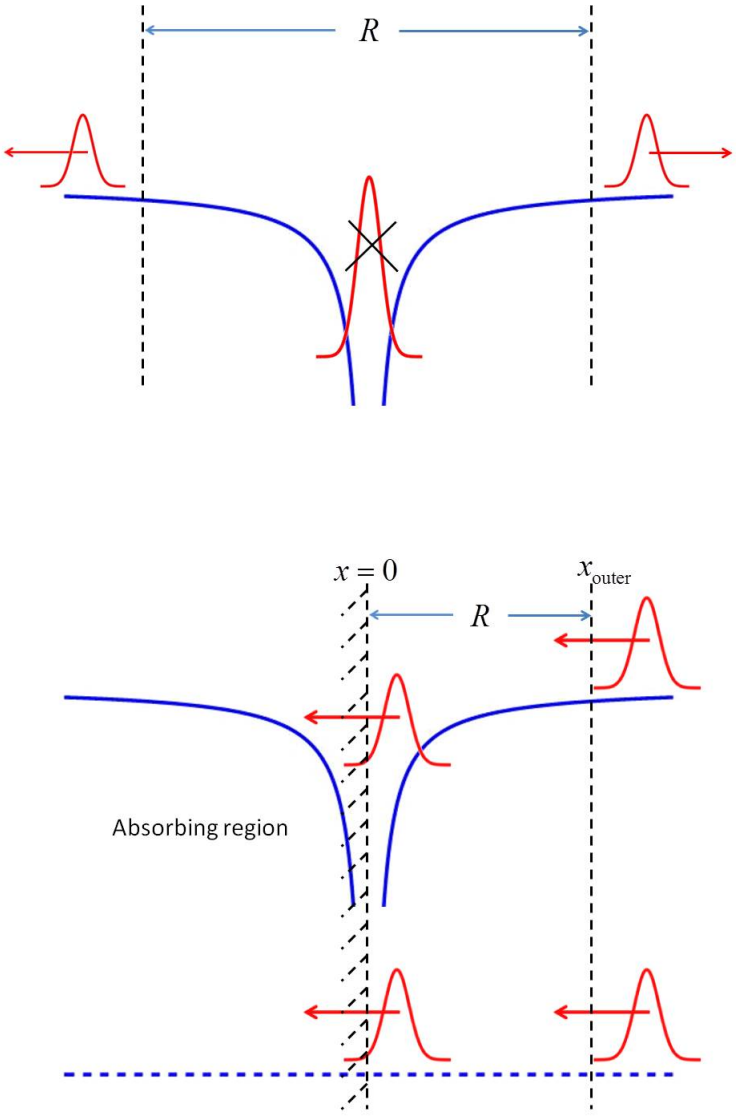

Figure 3.3: Schematic diagram for the back-propagation technique. In such a procedure we first solve the TDSE describing the interaction of the model potential with the laser pulse forward in time and obtain the ionizing wave packet by separating it from the whole wave function long after the laser pulse ceases (upper panel). We then back propagate one side of the normalized ionizing wave packet (e.g., right side) once within the potential and once as a free particle and absorb the corresponding wave packet at the center of the grid ($x = 0$) by using ECS boundary at the other side (e.g., left side) of the grid (lower panel). The difference of these two propagation times gives a time delay that relates to the propagation on one side. Repeating this procedure again for the other side of the ionizing wave packet and adding the two time delay contributions together, we finally obtain a time delay for the corresponding photoionization process accumulated in region R.

3.1.3 Application to single-photon ionization by an XUV pulse

The theoretical method outlined above is, in general, applicable to ionization of an atom or molecule in any light field. Here we present results for the application to photoionization of an electron initially bounded in two different model potentials. First, we use a short-range Yukawa potential in 1D

$$V_{\mathrm{Y}}(x) = -\frac{Z}{\sqrt{x^2+a}} e^{-\frac{|x|}{b}}, \tag{3.19}$$

where Z is the effective nuclear charge, a is the soft-core parameter, and b is a parameter that determines the effective range of this 1D potential. For our simulations we choose $Z = 3.0$, $a = 2.0$, and $b = 30.0$, which relate to energies of -1.6742 and -1.0124 of the ground and first excited states. As a long-range interaction we make use of the Coulomb potential in 1D

$$V_{\mathrm{C}}(x) = -\frac{Z}{\sqrt{x^2+a}}. \tag{3.20}$$

For $Z = 3.0$ and $a = 2.0$, the energies of the lowest two states are -1.7117 and -1.0807, which are close to the energies of the Yukawa potential.

For the interaction with the XUV laser pulse we use the length gauge, i.e.,

$$V_{\mathrm{light}}(t) = E_{\mathrm{XUV}}(t)x, \tag{3.21}$$

where $E_{\mathrm{XUV}}(t)$ represents a linearly polarized XUV pulse with a $\sin^2$ envelope, i.e.,

$$E_{\mathrm{XUV}}(t) = E_0 \sin^2(\pi t/T)\cos(\omega t + \phi), \tag{3.22}$$

where E_0 is the peak amplitude, T is the pulse duration, ω is the central frequency, and ϕ is the carrier-envelope phase (CEP).

To solve the corresponding TDSE, we use the previously introduced Crank-Nicolson method in a grid representation. We use a spatial step of $\delta x = 0.02$ and a time step of $\delta t = 0.002$, and the grid extends from -4000 to 4000, which is large enough to hold the full wave function in our simulations on the grid. The initial ground and first excited states are obtained by the ITP method. We continue the propagation of the wave function after the interaction with the XUV pulse until

Table 3.1: Results of numerical calculations for the times $t_{\Psi_g,R}$, $t_{\Psi_g^{(0)},R}$ and the time delay $\Delta t_{\Psi_g,R}$ for different spatial steps δx and a fixed time step of $\delta t = 0.002$. Results are obtained for ionization from the ground state of the 1D Yukawa potential and $R = [0, \pm 460]$. The parameters of the XUV pulse were: peak intensity $I = 1 \times 10^{15}$ W/cm^2, frequency $\omega = 100$ eV, pulse duration $T = 400$ as, and carrier-envelope phase $\phi = -\pi/2$.

spatial step	$t_{\Psi_g,R}$	$t_{\Psi_g^{(0)},R}$	$\Delta t_{\Psi_g,R}$
0.5	275.3389	274.4569	0.8820
0.2	240.6028	241.5927	−0.9899
0.1	236.8736	237.9043	−1.0307
0.05	235.9751	237.0109	−1.0358
0.02	235.7258	236.7628	−1.0370
0.01	235.6903	236.7274	−1.0371

the ionizing parts of the wave packet reach a distance beyond $|x| \geqslant 500$ and hence can be well separated from the remaining bound parts. This allows us to remove the latter parts from the grid and remain the ionizing parts of the wave function only. We then propagate the ionizing parts at negative and positive x backwards in time independently, either under the influence of the potential, V_Y or V_C, or as a free particle. We determine the corresponding times $t_{\Psi_i,R}$ and $t_{\Psi_i^{(0)},R}$ for both parts of the ionizing wave function and added the two contributions. In the 1D calculations we defined the region as $R = [\pm x_{\text{inner}}, \pm x_{\text{outer}}]$, where x_{inner} and $x_{\text{outer}} \leq 500$ are the inner and outer boundaries, respectively, and the $\pm$-signs apply to back-propagation of the two parts of the ionizing wave packet along the positive/negative x-axis, respectively. We absorb the wave function beyond the inner boundary x_{inner} using the ECS method [76].

Based on the results of recent experimental observations and theoretical calculations, we expect that the time delay $\Delta t_{\Psi_i,R}$ as well as the difference in the time delays for the ionization from different initial states $\Delta T(\Psi_i, \Psi_j, R)$ are of the orders of a few tens of attoseconds. Resolution of such small times requires an analysis of the time and spatial steps in the numerical simulations in order to establish appropriate limits for grid parameters towards a convergence of the results in our present studies. In Tables 3.1 and 3.2 we present a set of numerical results obtained for different δx and δt in the case of the Yukawa potential. We see that a convergence of the time delay $\Delta t_{\Psi_i,R}$

Table 3.2: Results of numerical calculations for the times $t_{\Psi_g,R}$ and $t_{\Psi_g^{(0)},R}$ and the time delay $\Delta t_{\Psi_g,R}$ for different time steps δt and a fixed spatial step of $\delta x = 0.02$. All the other parameters were the same as in Table 3.1.

time step	$t_{\Psi_g,R}$	$t_{\Psi_g^{(0)},R}$	$\Delta t_{\Psi_g,R}$
0.1	237.0072	238.0431	−1.0359
0.05	236.0391	237.0757	−1.0366
0.02	235.7752	236.8121	−1.0369
0.01	235.7378	236.7747	−1.0369
0.005	235.7284	236.7654	−1.0370
0.002	235.7258	236.7628	−1.0370
0.001	235.7254	236.7624	−1.0370

within less than 0.001 a.u. (i.e., < 0.025 as) is reached for a time step of $\delta t = 0.002$ and a spatial step of $\delta x = 0.02$. Similar conclusions hold for our studies with the Coulomb potential as well.

As mentioned above, the time delay $\Delta t_{\Psi_i,R}$ depends on the size of the region R, and should be negative and converge to a finite limit for short-range potentials only. To test these expectations, we perform a set of simulations for the time delays for photoionization from the ground and excited states of both potentials as a function of x_{outer} by fixing $x_{\text{inner}} = 0$, i.e., for the region $R = [0, x_{\text{outer}}]$. As expected, the values for the time delays are negative and decrease as the size of R (i.e., x_{outer}) increases for each of the results presented in Fig. 3.4. For the Yukawa potential (panel a) convergence is found for outer boundaries $x_{\text{outer}} > 150$. Consequently, for large values of the outer boundary we obtain a well-defined value for the time difference ΔT (red dashed line) of the time delays for ionization from the ground and the excited states.

In contrast, our results do not show a convergence for the time delays as a function of x_{outer} in the case of the long-range Coulomb potential [see Fig. 3.4(b)]. This reflects the well-known logarithmic divergence of the time delay for the Coulomb potential in scattering processes and, hence, for ionization from any bound state within the potential. Of course, in these cases a WS time delay as the derivative of the phase shift [see Eq. (3.2)] cannot be defined as well, since its derivation requires a finite limit of $\Delta t_{\Psi_i,R\to\infty}$. It is interesting to point out that the results in Fig. 3.4(b) further show that the logarithmic divergence is, in general, still present for the difference

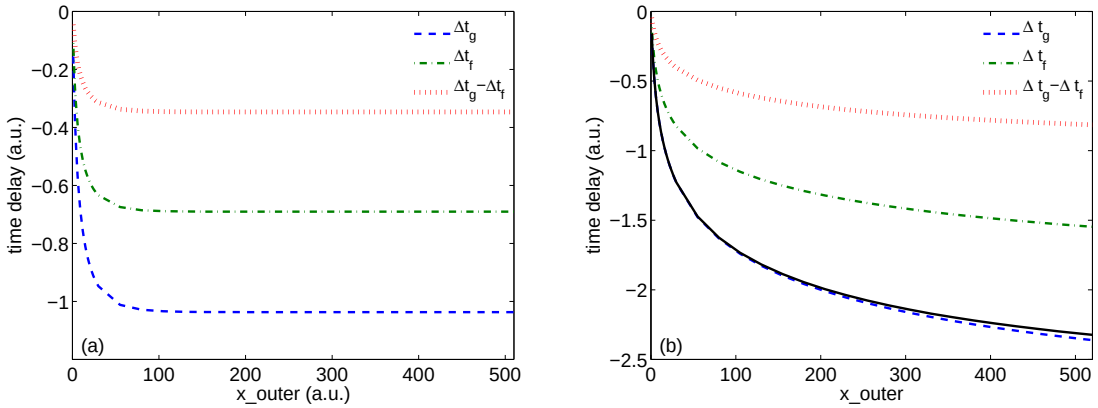

Figure 3.4: Time delays $\Delta t_{\Psi_i,R}$ and time difference $\Delta T(\Psi_i, \Psi_j, R)$ as a function of the outer integration boundary x_{outer} for two potentials: (a) short-range Yukawa potential and (b) long-range Coulomb potential. Time delays obtained for the ground and first-excited states are represented by blue dashed lines and green dash-dotted lines, respectively; while the red dotted lines show the results for the time difference between the delays. In (b) the black solid and blue dashed lines correspond to two different forward propagation distances: $\langle x_{\text{forward}} \rangle = 2000$ and 3000, respectively, for the ionization from the ground state. In all calculations we have used an XUV pulse with peak intensity $I = 1 \times 10^{15}$ W/cm^2, central frequency $\omega = 100$ eV, pulse duration $T = 400$ as, and carrier-envelope phase $\phi = -\pi/2$ for the ionization.

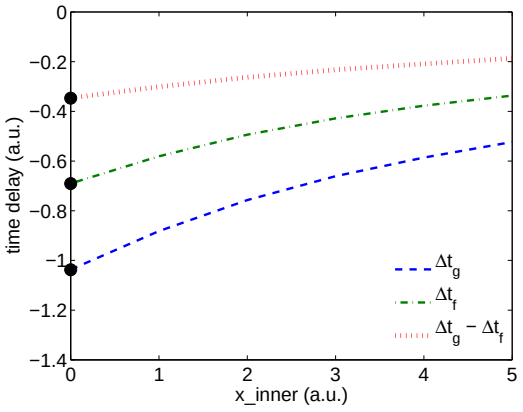

Figure 3.5: Time delays and difference between time delays as a function of inner integration boundary x_{inner}. Symbols and laser parameters are the same as in Fig. 3.4. We also plotted the WS time delays as black dots in this figure.

between a pair of time delays obtained for the ionization from two different initial states. Thus, such a time delay difference does not simply depend on the short-range character of the potential but also contains information about the long-range part of the potential and is therefore not well-defined as well. The present results agree well with the conclusions of early works on time delays [41]. We may however reemphasize that any time delay obtained for a finite region via the present method is finite and therefore well-defined, even in the case of the long-range Coulomb potential. As pointed out above, this allows us to study certain aspects with respect to the parameters of the XUV pulse and the effects of an additional field even in the Coulomb case.

It is necessary to point out that for the Coulomb potential the time delay also depends on the distance that the ionizing wave packet is propagated in forward direction. This is due to the long-range character of the Coulomb potential, since the central momentum of the ionizing wave packet decreases with an increase of the forward propagation distance. Thus, the velocity of the free particle during the back-propagation decreases as well. In Fig. 3.4(b) we show this effect by showing results for the time delay from the ground state for two forward propagation distances: $\langle x_{\text{forward}} \rangle = 2000$ (black solid line) and 3000 (blue dashed line). As expected, the time delays for $\langle x_{\text{forward}} \rangle = 3000$ are slightly smaller than those for $\langle x_{\text{forward}} \rangle = 2000$. This shows the need to use rather large grids for the numerical simulations in the case of a Coulomb potential. However, this small dependence on the forward-propagation distance does not change our conclusions regarding the convergence of the results towards infinite regions.

We also note from the results in Fig. 3.4 that the time delay increases most strongly in the region close to the center of the potential, where the potential changes most strongly. This indicates that the results should depend on the choice of the inner boundary x_{inner} of the region R. To study this feature, we fix the outer boundary of R at $x_{\text{outer}} = 500$, which is large enough to obtain converged results in the case of the Yukawa potential, and then vary the inner boundary x_{inner}. The results in Fig. 3.5 show the expected dependence on the choice of x_{inner}: the absolute values of the time delays decrease by half as x_{inner} increases from 0 to 5. In the remainder of the present studies we have chosen the $x_{\text{inner}} = 0$ as the inner boundary, since this value corresponds

to the expectation value of x for all the bound states investigated here.

3.1.4 Comparison with results of other theoretical methods

Up to now, we have introduced the theoretical principle of our new method to calculate time delays for photoionization processes and also established a numerical technique to demonstrate its application. In order to further support our theory, we want to compare the time delays calculated using our new method with results from those of previously existing and well-tested methods. To this end, for a short-range potential, we like to make use of the WS time delay formula, i.e., Eq. (3.2), and further review another method based on the analysis of the photoelectron trajectory in the continuum.

To make use of the WS time delay formula for the 1D Yukawa potential of Eq. (3.19), we calculate the scattering phase shift from a time-independent scattering approach. We assume that an electron with energy E (i.e., momentum $k = \sqrt{2E}$) is incident from $x = -\infty$ towards the Yukawa potential. We then solve the corresponding time-independent Schrödinger equation numerically using the fourth order Runge-Kutta method up to $|x| = 500$, project the numerical solution onto the appropriate plane-wave solutions for $x \to \pm\infty$, and obtain the corresponding phase shift $\varphi(E)$. By repeating the same procedure for an electron with energy $E + \Delta E$, we know the phase shift $\varphi(E + \Delta E)$ and then evaluate the WS time delay approximately as

$$\Delta t_{\mathrm{WS}}^{(\mathrm{scat})}(E) = \frac{\varphi(E + \Delta E) - \varphi(E)}{\Delta E}. \tag{3.23}$$

In order to take account of the energy spread of the ionizing wave packet in a specific photoionization process, we averaged $\Delta t_{\mathrm{WS}}^{(\mathrm{scat})}(E)$ over the energy spectrum of the wave packet, as obtained in our time-dependent numerical simulations. Finally, we consider the photoionization as a half-scattering process and divide the result of the average by two. The resulting WS time delays are shown as black dots in Fig. 3.5 and are in good agreement with our numerical results, obtained from the time-dependent calculations, for $x_{\mathrm{inner}} = 0$ and $x_{\mathrm{outer}} = 500$. This is in support of the applicability of our approach to obtain time delays from the time-dependent numerical simulations.

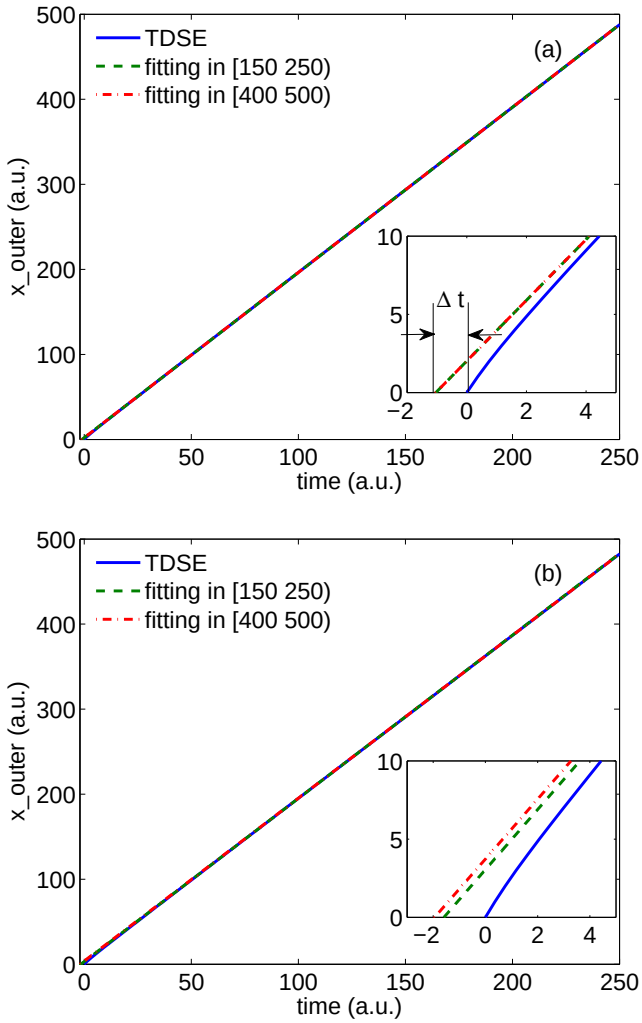

Figure 3.6: Extrapolation method to calculate the WS time delay. The solid blue lines show the outer integration boundary x_{outer} as a function of time for (a) the Yukawa potential and (b) the Coulomb potential, calculated from Eq. (3.12) by solving TDSE. The green dashed and red dash-dotted lines are obtained by linearly fitting the solid blue lines in two regions: $[150, 250)$ and $[400, 500)$ respectively. The two insets show the behaviors near $t = 0$ for each line. Δt in panel (a) corresponds to the WS time delay for a short-range potential.

As discussed before, the derivation of the WS time delay is based on the comparison of two trajectories, one of the free particle and the other of the scattering particle. This actually provides another useful way of calculating the WS time delays since both trajectories are easily accessable in our numerical simulations of a photoionization process. In practice, the WS time delay is given as the time difference between the time obtained by extrapolating the linear part of the photoelectron trajectory back to the center of the potential ($x = 0$) and the time zero (chosen as the center of the XUV pulse). There is no need to numerically calculate the free particle trajectory since it is just a line that goes through the origin (i.e., $x = 0$ and $t = 0$) with the same slope as that of the photoelectron trajectory. Usually, the photoelectron trajectory is calculated as the expectation value of the ionizing wave packet as a function of time [44, 46]. Here, as shown in Fig. 3.6, we instead obtain the trajectory by plotting the outer boundary x_{outer} of the region R as a function of $t_{\Psi,R}$ (blue solid lines), which requires no more calculations once the back-propagation simulations are done. As an example, we show how the WS time delay is obtained using this method for the short-range Yukawa potential in Fig. 3.6(a), where the fit of trajectories in two different regions gives the same time delay. However, based on our above discussions, it is expected that this method does not work for a long-range potential, such as the Coulomb potential considered in Eq. (3.20), since the trajectory of the photoelectron ionized from the Coulomb potential has a logarithmic term and cannot be fitted to a linear line. This is illustrated in Fig. 3.6(b), from which one sees the fitted lines have different interceptions with the time axis for different fitting regions.

3.1.5 Dependence of time delay on XUV pulse parameters

In order to systematically test the applicability of our time-dependent method of calculating time delays and also study the dependence of the time delay introduced here on the parameters of the XUV ionizing pulse, in Fig. 3.7 we present our results as functions of (a) the XUV frequency at a fixed pulse duration of $T = 400$ as and (b) the duration of the XUV pulse at a fixed frequency of $\omega = 100$ eV. The peak intensity is $I = 1 \times 10^{15}$ W/cm^2 and the CEP is $\phi = -\pi/2$ in each of these simulations. Other than the time-dependent back-propagation method (blue diamonds), we also

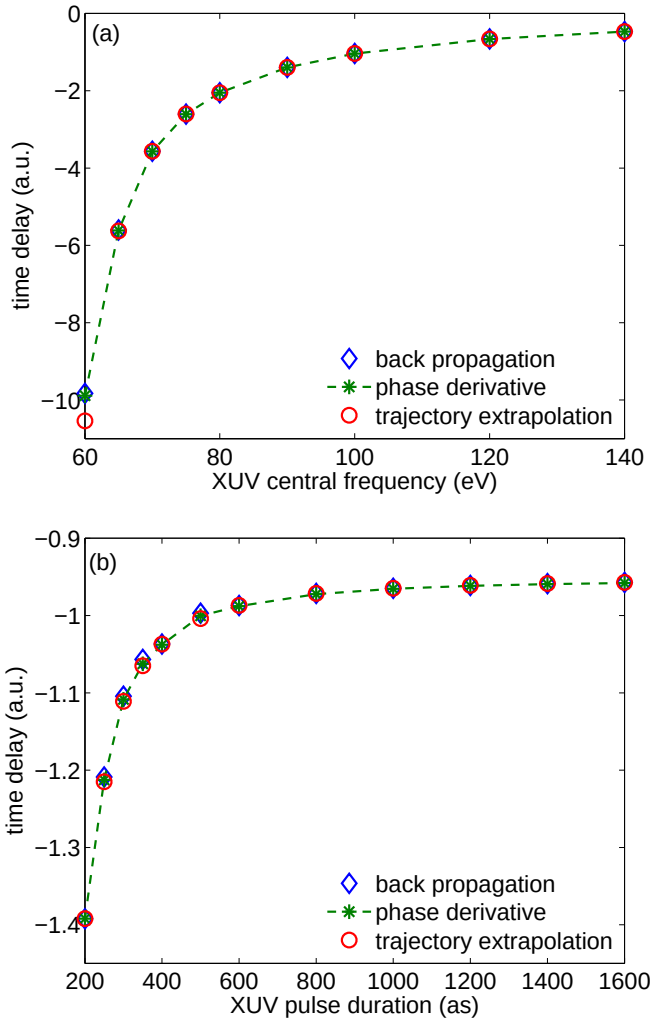

Figure 3.7: Time delays for ionization from the ground state of the Yukawa potential as functions of (a) the XUV photon frequency ($T = 400$ as) and (b) the pulse duration of the XUV pulse ($\omega = 100$ eV). We have used three different methods to calculate the time delay: back propagation method (blue diamonds), phase derivative method (green dashed lines with asterisks), and trajectory extrapolation method (red open circles). Other laser parameters are: $I = 1 \times 10^{15}$ W/cm^2 and $\phi = -\pi/2$.

show time delays from the other two methods: the energy derivative with respect to the phase shift (green dashed lines with asterisks) and the trajectory extrapolation method (red open circles). The results from different methods agree very well with each other and this again shows the application of the time-dependent back-propagation method on time delays is solid and convincing.

The trends of the time delays also agree well with qualitative expectations. The absolute value of the time delay decreases towards zero as the frequency of the ionizing XUV pulse and, hence, the final kinetic energy of the emitted electron increases [Fig. 3.7(a)]. This is due to the fact that the effect of the potential on the motion of the photoelectron becomes negligible in the limit of infinitely large kinetic energy of the electron (i.e., infinite large XUV frequency) and therefore the time spent in the potential approaches that of the free particle in this limit. We further find that the absolute value of the time delay decreases with an increase of the XUV pulse duration [Fig. 3.7(b)]. This dependence is closely related to that presented in Fig. 3.7(a) and can be qualitatively understood as follows. It is found that the expectation value of the kinetic energy of the ionizing wave packet increases as the XUV pulse duration increases, which causes the time delay to increase according to its dependence on photoelectron energy in Fig. 3.7(a). Furthermore, due to the finite pulse duration the ionizing wave packet has a certain bandwidth about a central kinetic energy. Consequently, the time delay obtained for the wave packet can be considered as an average over contributions at particular electron energies within the bandwidth (weighted by the ionization probability at a given energy). As indicated by the results in Fig. 3.7(a) the time delay does not change linearly with the kinetic energy. Therefore, the time delay obtained for a wave packet will be smaller than its contribution at the central kinetic energy or the expectation value of the kinetic energy. This difference decreases and, thus, the time delay for the wave packet increases as the energy bandwidth of the wave packet decreases, i.e., as the pulse duration increases.

3.1.6 Application to laser-assisted XUV photoionization

As introduced in Chapter 1, the HHG process is a popular and promising way of generating attosecond XUV pulses. Usually a few-cycle intense IR laser field is used to drive the HHG process.

So in many applications using the attosecond XUV pulses, the strong laser field is present and therefore influences the interaction of the XUV pulse and the systems of interest. In particular, the interplay of the strong laser field and the ionic potential of the system is very important for many attosecond measurements, including the attosecond streak camera [34], laser-induced tomography [79], diffraction imaging of molecules [80], and many other applications. In this section, as another application of our proposed method of calculating time delays in photoionization, we like to extend this idea to the situation, in which the XUV photoionization is assisted by a streaking field and the interplay of the streaking field and the ionic potential can be treated together as a time-dependent combined potential.

The attosecond streaking experiment resembles such a set up and we like to study the effect of a streaking field on WS-like time delays. To this end, we will first discuss how the streaking field can be included in our numerical simulations of time delays and then study the impact of a streaking field on the time delays for the short-range Yukawa as well as the long-range Coulomb potentials by varying the parameters of the streaking field. We may stress that it is found (see Section 3.2) that the time delay studied here does not correspond to those observed in streaking experiments. The difference between these two delays are apparent and significant: the present one is evaluated directly from the definition of a time delay from the time domain, while the streaking time delay is extracted from a streaking trace in the momentum space.

The streaking field is considered as part of the potential $V(\boldsymbol{r})$ in Eq. (3.16) and can be represented by

$$V_s(\boldsymbol{r}, t) = E_s(t) \cdot \boldsymbol{r}, \tag{3.24}$$

where the common length-gauge is used. Thus, in the present calculations the streaking field is treated on equal footing with the atomic potential. After the forward propagation of the wave function from its initial state and the separation of the bound and ionizing part of the wave function, we then propagate the ionizing part of the wave function backwards in time once within the combination of the atomic potential and the streaking field and once as a free particle.

As a result, we obtain the time delay associated with the ionizing part of the wave function in the combined potential of the short- or long-range interaction and the streaking field as

$$\Delta t^{(\mathrm{IR})}_{\Psi_i,R} = t^{(\mathrm{IR})}_{\Psi_i,R} - t_{\Psi^{(0)},R} \tag{3.25}$$

where $t^{(\mathrm{IR})}_{\Psi_i,R}$ is the time the ionizing wave packet spends in region R in the presence of both the (short- or long-range) atomic potential and the streaking field, and $t_{\Psi^{(0)},R}$ is the time for the corresponding free particle.

Here, the forward propagation of the wave function has to be continued as long as the streaking field is present. As pointed out above, for the long-range Coulomb potential, the time delay depends on the distance that the wave packet is propagated in the forward direction. In order to keep the corresponding error small in our current analysis we use a large grid of -13000 to 13000 and terminate the forward propagation when the expectation value of the ionizing wave packet reaches 8000. We increase the spatial step to $\delta x = 0.1$ and the time step to $\delta t = 0.02$ as compared to the previous calculations to save computation time. Test calculations show that the relative error of the present results is about 1%. In order to be consistent but also without loosing generality, we make use of the Yukawa and the Coulomb potentials with the same parameters as before, but choose the first excited state as the initial state. We have checked that the ionization probability induced by the streaking field is negligible up to an intensity of 1×10^{13} W/cm^2.

We apply the ionizing XUV pulse at two positions of the streaking field: one centers at the maximum point (zero of the vector potential) and the other centers at the central zero point (maximum of the vector potential). In the upper row of Fig. 3.8, the results for the time delays in the presence of the streaking field (green solid lines: XUV centered at zero of the vector potential; blue dashed lines: XUV centered at maximum of vector potential) are shown as a function of the outer boundary x_{outer} of the region R for the Yukawa (left) and the Coulomb (right) potentials. Similar as in the results without streaking field, we see that there is a well-defined limit of time delays for the short-range Yukawa potential as the region R increases, while there is no convergence found for the Coulomb potential.

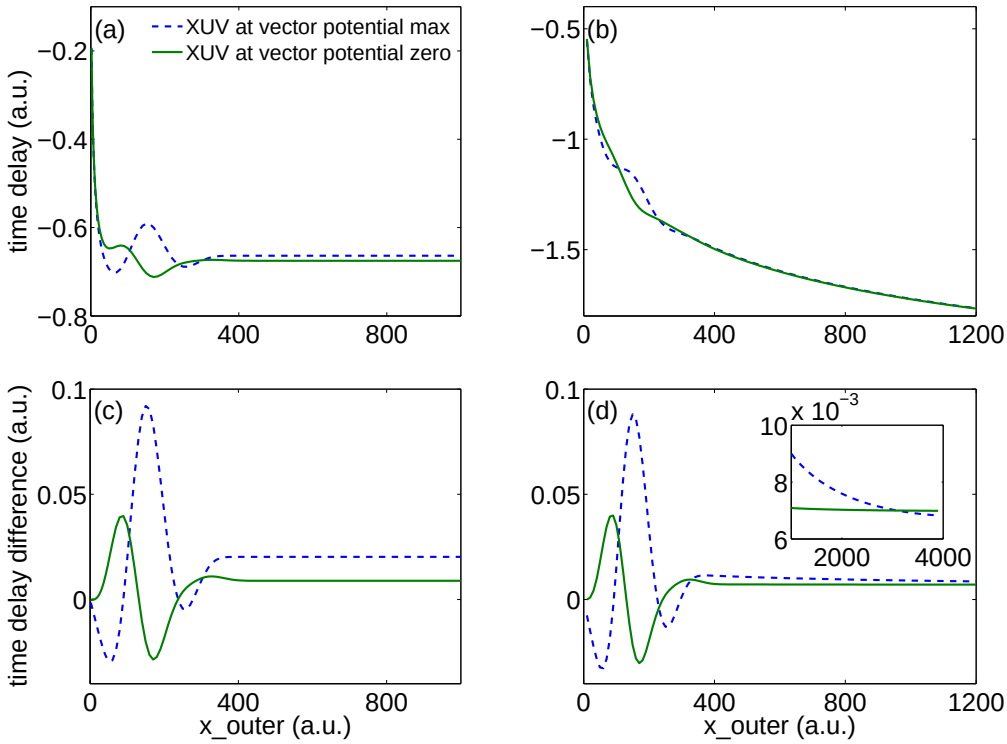

Figure 3.8: Time delays (upper row) and time delay differences (lower row) as a function of the outer boundary x_{outer} of R for Yukawa potential (left column) and Coulomb potential (right column). For each potential we have centered the XUV pulse at two different positions, which correspond to the maximum (blue dash-dotted line) and zero (green solid line) of the vector potential of the streaking field, respectively. The XUV parameters are: $I_{\text{XUV}} = 1 \times 10^{15}$ W/cm^2, $\omega_{\text{XUV}} = 100$ eV, $T_{\text{XUV}} = 400$ as, and $\phi_{\text{XUV}} = -\pi/2$. The streaking parameters are: $I_s = 1 \times 10^{12}$ W/cm^2, $\lambda_s = 800$ nm, $N_s = 3$ cycle, and $\phi_s = -\pi/2$. The small box in (d) shows the long-range behavior of the two curves.

To illustrate the effect of the streaking field, we present in the lower row of Fig. 3.8 the difference between the time delays in the presence of the streaking field to those without streaking field as a function of x_{outer}, i.e.,

$$\Delta T = \Delta t^{(\text{IR})}_{\Psi_i,R} - \Delta t_{\Psi_i,R}, \tag{3.26}$$

Although there is no well-defined limit of the time delays for infinite regions in the Coulomb case, neither with nor without streaking field, for any finite region the time delays introduced here are well-defined and the effect of the streaking field can thus be analyzed. The same argument applies to the weak dependence of the Coulomb results on the distance of forward propagation in our simulations.

For both potentials, we see that the time delay difference ΔT oscillates for $x_{\text{outer}} < 400$. This oscillation is due to the presence of the streaking field, since the ionizing wave packet propagates up to about $x \simeq 400$ before the streaking field ceases in present simulations. We note that the differences ΔT are small, less than 3% for the Yukawa potential and less than the numerical error of 1% for the Coulomb potential, as compared to the time delays induced by the atomic potentials themselves. We therefore do not find a significant effect of the streaking field, neither for a short-range nor for a long-range potential, on the time delays in our present simulations. As pointed out before, this result however does not allow to draw conclusions for the streaking experiment, since time delays introduced here are not equivalent to time delays measured in streaking experiments.

Before we continue to further study the influence of the streaking field, we note a subtle point in the results obtained for the Coulomb potential, which are presented in Fig. 3.8. While neither the time delays with and without streaking field converge as a function of the outer boundary x_{outer}, we find a converged result (within the numerical error) for the time delay difference ΔT, if the XUV pulse is centered at the zero position of the vector potential of the streaking field [see green solid line in Fig. 3.8(d)]. This occurs since in this case the momentum distribution of the ionizing wave packet at the end of the forward propagation is the same as that without streaking field. In contrast, if the XUV pulse is applied at the maximum position of the vector potential, the

final momentum distribution is shifted and thus no convergence of the time delay difference within the range of present boundaries is found [see blue dashed line in the inset of Fig. 3.8(d)].

The conclusion that the streaking field does not influence significantly the time delay introduced here holds over a large range of XUV frequencies as well as for streaking intensities up to about 10^{13} W/cm^2. In Fig. 3.9 we present the results of time delays obtained for (a) the Yukawa potential and (b) the Coulomb potential with (blue lines with squares) and without (blue lines with asterisks) streaking field as a function of the XUV frequency. Since the results are in close agreement, we also show the relative difference between them (green lines with triangles), which does not exceed 5% and 2% in the Yukawa and Coulomb cases, respectively.

As one would expect, the relative difference between the results of time delays obtained with and without streaking field does increase with an increase of the streaking field intensity. This can be clearly seen from the results shown in Fig. 3.10. It appears that for streaking intensities up to 10^{12} W/cm^2 the relative difference between the results is small enough such that there is no significant effect on the time delay. While the relative difference quickly increases beyond 10% in the case of the Yukawa potential with a further increase of the streaking intensity, the 10%-limit is not reached for a streaking intensity of 10^{13} W/cm^2 in the case of the Coulomb potential.

3.2 Interpretation of time delays measured in streaking experiments[2]

The photoemission time delay experiment in neon atom using the attosecond streaking technique has initiated a lot of theoretical discussions about understanding this experiment, especially how one should interpret the measured time delay (e.g., [37–39, 44, 81]). As mentioned in the introduction, it was proposed that this measured time delay consists of two contributions [37, 38]: one is the WS time delay, which is calculated as the energy derivative with respect to the scattering phase shift induced by the electrostatic Coulomb potential, and the other one is the propagation time delay that the photoelectron accumulates during its propagation in the combined potential of

[2] The results of this section are presented in J. Su, H. Ni, A. Becker, and A. Jaroń-Becker, Phys. Rev. A **88**, 023413 (2013), J. Su, H. Ni, A. Becker, and A. Jaroń-Becker, Phys. Rev. A **89**, 013404 (2014), and J. Su, H. Ni, A. Becker, and A. Jaroń-Becker, Chin. J. Phys. **52**, 404 (2014).

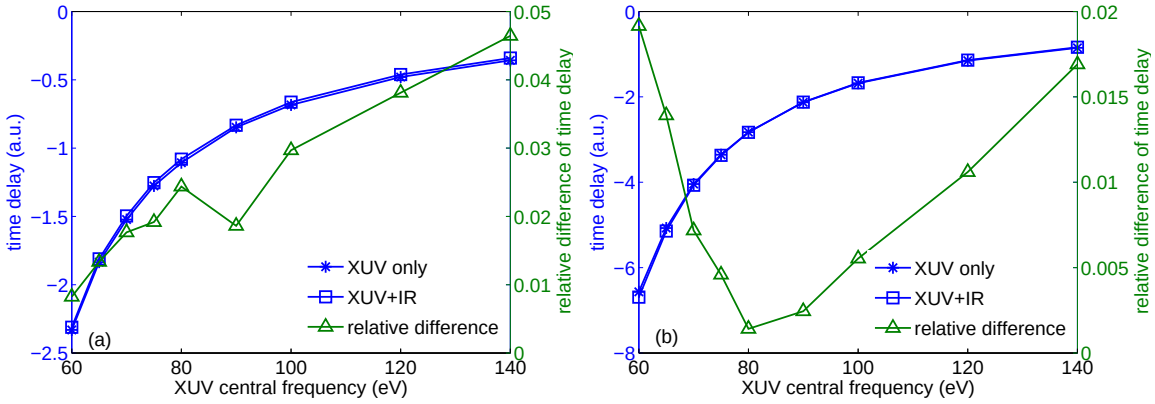

Figure 3.9: Time delays with (blue lines with squares) and without (blue lines with asterisks) streaking field as well as relative differences between the results (green lines with triangles) as a function of XUV central frequency for (a) Yukawa potential and (b) Coulomb potential. The XUV pulse is centered at the central zero point (maximum vector potential point) of the streaking field. Other laser parameters are the same as in Fig. 3.8. For the Coulomb case, the time delays are calculated at $x_{\text{outer}} = 800$.

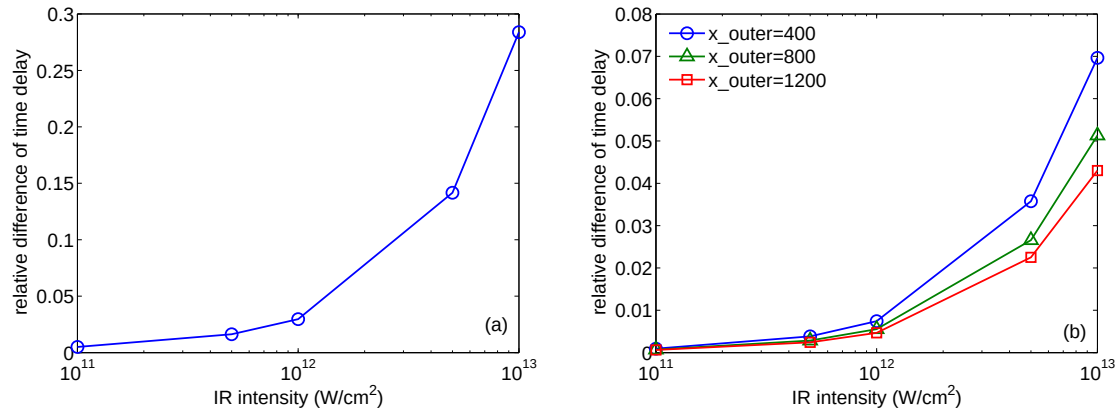

Figure 3.10: Relative differences of time delays as a function of the streaking intensity for (a) Yukawa potential and (b) Coulomb potential. The XUV pulse is centered at the central zero point of the streaking field. Laser parameters are the same as in Fig. 3.8 expect I_{IR} changes. For the Coulomb case, the time delays are taken at $x_{\text{outer}} = 400$, 800 and 1200.

the streaking and the Coulomb fields, which is sometimes also called as the Coulomb-laser coupling time delay. However, the sum rule $\Delta t_s = \Delta t_{\rm WS} + \Delta t_{\rm prop}$ seems to be questionable for the following reasons: First, for a long-range Coulomb interaction, the WS time delay is not a well-defined concept, as originally pointed out by Smith [41] and recently numerically reconfirmed by us [42, 43]. Evaluating it using the energy derivative with respect to the scattering phase shift, as done for a short-range WS delay, only accounts for the short-range part of the Coulomb potential and does not obey the original definition for the WS time delay. Furthermore, while the sum rule appears to be a good empirical formula (e.g., [53]), a rigorous proof was never given. For instance, in Ref. [38] this rule has been derived however based on the eikonal approximation, which is quite questionable for the weak intensities used in streaking experiments. Furthermore, in Ref. [37] the propagation time delay was calculated using the so-called classical-trajectory Monte Carlo method and the results do not support the sum rule. Finally, even within the framework of the sum rule, applications differ in some details: Ivanov *et al.* [38] apply the rule for both short- and long-range potentials, while Nagele *et al.* [37] claim that the sum rule needs to be used for the long-range interaction only. In the latter work, it has been assumed that the propagation time delay is zero. In order to contribute to the ongoing debate, we like to systematically study the streaking experiment in this section.

3.2.1 Extracting streaking time delays in numerical simulations

As introduced in Chapter 1, the streaking time delay is the temporal shift of the real streaking trace with respect to the trace predicted by the original streaking formula, $\boldsymbol{k}_f = \boldsymbol{k}_0 - \boldsymbol{A}_s(t_i)$. To obtain such a delay in numerical simulations, we need to calculate the streaking trace accurately without making any approximations. To this end, we simulate a streaking experiment by numerically solving the following TDSE

$$i\frac{\partial \Psi(\boldsymbol{r},t)}{\partial t} = \left[\frac{\boldsymbol{p}^2}{2} + V(\boldsymbol{r}) + (\boldsymbol{E}_{\rm XUV}(t) + \boldsymbol{E}_s(t))\cdot\boldsymbol{r}\right]\Psi(\boldsymbol{r},t), \tag{3.27}$$

where both the XUV and the streaking fields are assumed to have a $\sin^2$ envelope shape and be linearly polarized in z-direction. We solve the TDSE on a grid in space and time by using

the common Crank-Nicolson method with spatial steps determined by the specific problem. In each simulation we propagate the wave function on the grid for a sufficiently long time until both laser pulses cease and the ionizing wave packet is far from the ionic core. We confirm that in all simulations the outgoing wave packets stay on the grid and do not reach its boundaries.

To obtain the momentum distribution we use one of the two following methods: one is to project the total wave function onto the correct continuum eigenstate, the other is to spatially separate the ionizing wave packet from the total wave function, which is possible due to the long propagation times used in the simulations, and then perform a Fourier transform. For the latter choice, we have to propagate the ionizing wave packet sufficiently far away from the nucleus so that the small error due to the projection onto the plane wave is negligible.

By varying the relative delay τ between the XUV and the streaking pulses, we obtain the streaking trace, in which the momentum of the photoelectron $\boldsymbol{k}_f$ is given as a function of τ. We usually present the streaking trace in the form of the expectation value of the momentum as a function of the relative delay in order to compare with other calculations. For model systems with more than one dimensions, we calculate the expectation value of the momentum in the laser polarization direction (z axis) with an opening angle of 5 to 10 degrees. An example for a streaking trace, over about the central cycle of a 8-cycle streaking pulse at 800 nm and 1×10^{12} W/cm^2, is shown in Fig. 1.7(a). As already pointed out, the streaking time delay relates to a momentum shift Δk and can be understood as the temporal shift of the TDSE trace (blue solid line) with respect to the trace predicted by the original streaking formula (green dashed line). In practice we however do not compare these two traces directly to obtain the streaking time delay. Instead we extract such a delay by fitting the TDSE streaking trace to

$$k_{f,z}(\tau) = k_{0,z} - \alpha A_s(\tau + \Delta t_s) \tag{3.28}$$

with $k_{0,z}$, α, and Δt_s as three fitting parameters, which can be retrieved using the least-square method.

3.2.2 Calculating propagation time delays using classical approaches

In view of the preexisting interpretation of the streaking time delay, it appears to be necessary to reinvestigate the original streaking formula, $\boldsymbol{k}_f \simeq \boldsymbol{k}_0 - \boldsymbol{A}(t_i)$, derived based on strong field approximation (SFA). As motioned in the introduction, the original streaking formula can be derived classically by assuming the photoelectron is set free in the continuum instantaneously at ionization time t_i with momentum $\boldsymbol{k}_0$ and then propagates only in the streaking laser field, i.e., the ionic potential is neglected during the propagation of the photoelectron. While such an approximation has been shown to work well in certain cases (e.g., [34]), however, for a streaking time delay of the order of a few tens of attoseconds, which relates to a momentum shift of the order of 10^{-3} a.u. (for a typical 800 nm streaking pulse with intensity of 10^{12} W/cm^2), a more careful method that also takes account of the ionic potential as well as the interplay between these two fields is of course necessary. In this subsection, we calculate the propagation (or coupling) time delay in a streaking experiment using classical approaches that take account of both fields and then compare this calculated propagation time delay with the streaking time delay obtained in TDSE simulations. The comparison will lead us a new interpretation of the streaking time delay for single-photon ionization.

It is known that in strong-field physics the propagation of an electron in the continuum can be often well described by classical analysis (e.g., [82]). We therefore make use of this method to analyze the time delay obtained in the streaking experiment. After the transition into the continuum due to XUV photon absorption the dynamics of the electron in the general 3D case is given by

$$\frac{d\mathbf{k}}{dt} = -\mathbf{E}_s(t) - \boldsymbol{\nabla} V(\mathbf{r}), \tag{3.29}$$

where $\boldsymbol{k}$ is the momentum of the photoelectron, $E_s(t)$ is the streaking field, and $V(\mathbf{r})$ is the atomic potential. For a linearly polarized field the simultaneous interaction of the electron with the field and the potential takes effect along the direction of the polarization, which we choose as the z-axis:

$$\frac{dk_z}{dt} = -E_s(t) - \frac{dV}{dz}. \tag{3.30}$$

One approach to solve Eq. (3.30) is to use perturbation theory by assuming $|E_s| \gg |\frac{dV}{dz}|$. To first order, the final asymptotic momentum is then given by [assuming $A(t) = 0$ and $V(z) = 0$ for $t \to \infty$]

$$\begin{aligned} k_{f,z}^{(1)}(t_i) &= k_{f,z}^{(0)}(t_i) + \Delta k_{f,z}^{(1)}(t_i) \\ &= k_{i,z} - A_s(t_i) + \frac{V(z_i)}{k_{i,z}} + \int_{t_i}^{\infty} \frac{E_s(t) V\left(z^{(0)}(t)\right)}{k_z^{(0)}(t)^2} dt \\ &\simeq k_{0,z} - A_s(t_i) + \int_{t_i}^{\infty} \frac{E_s(t) V\left(z^{(0)}(t)\right)}{k_z^{(0)}(t)^2} dt, \end{aligned} \tag{3.31}$$

where $k_{0,z} = \sqrt{k_{i,z}^2 + 2V(z_i)} \simeq k_{i,z} + V(z_i)/k_{i,z}$ is the streaking-field-free asymptotic momentum,

$$z^{(0)}(t) = z_i + [k_i - A_s(t_i)]\,(t - t_i) + \int_{t_i}^{t} A_s(t')dt', \tag{3.32}$$

and

$$k_z^{(0)}(t) = k_{i,z} - A_s(t_i) + A_s(t), \tag{3.33}$$

are the zeroth order solutions for the position and momentum of the electron. t_i, z_i, and $k_{i,z}$ are the initial time, position, and momentum of the electron after its transition into the continuum.

We note that Eq. (3.31) is equivalent to Eq. (25) in Ref. [83], in which the authors used a quantum approach to calculate the momentum shift induced by the so-called Coulomb-laser coupling effect in laser-assisted photoionization based on the eikonal approximation. This result was later adopted in Ref. [38] to study the influence of the streaking field on the measured time delay in a streaking experiment. However, one may notice that, similar to what we have done here, the formula derived in Ref. [83] was based on the assumption that the laser field is rather strong (e.g., 1.5×10^{14} W/cm^2 in one of the numerical examples in Ref. [83]), which is usually not applicable for a streaking experiment (streaking intensities are typically in the range of 1×10^{10} W/cm^2 to 1×10^{12} W/cm^2). Below we therefore compare results of the perturbative approach with the numerical solution for the classical electron dynamics in order to test the applicability of the perturbative approach.

The use of perturbation theory can be avoided by integrating Eq. (3.30) directly. By multiplying dz to both sides of Eq. (3.30) and then integrating it, the solution of Eq. (3.30) for the

asymptotic momentum of the electron at $z \to \infty$ can be written as

$$\begin{aligned} k_{f,z}(t_i) &= \sqrt{k_{i,z}^2 + 2V(z_i) - 2\int_{t_i}^{\infty} E_s(t)k_z(t)dt} \\ &= \sqrt{k_{0,z}^2 - 2\int_{t_i}^{\infty} E_s(t)k_z(t)dt}. \end{aligned} \tag{3.34}$$

Making use of this equation requires knowing $k_z(t)$, which is available by numerically solving Eq. (3.30). As we will see later, writing the final momentum in this form is very helpful for interpretation of the propagation time delay.

To relate the final momentum of the electron to the propagation time delay, we set the final momentum from Eq. (3.31) or (3.34) equal to

$$\begin{aligned} k_{f,z}(t_i) &= k_{0,z} - \alpha A_s(t_i + \Delta t_{\text{prop}}) \\ &\simeq k_{0,z} - \alpha A_s(t_i) + \alpha E_s(t_i)\Delta t_{\text{prop}} \end{aligned} \tag{3.35}$$

as used in the fitting of the streaking results. Then the propagation time delay that the electron accumulates in the combined field of the streaking field and the atomic potential is finally given by [for $E_s(t_i) \neq 0$]

$$\Delta t_{\text{prop,pert}} \simeq \frac{(\alpha - 1)A_s(t_i) + \int_{t_i}^{T_s} \frac{E_s(t)V\left(z^{(0)}(t)\right)}{[k_z^{(0)}(t)]^2} dt}{\alpha E_s(t_i)} \tag{3.36}$$

for the perturbative approach, and

$$\Delta t_{\text{prop,exact}} \simeq \frac{\sqrt{k_{0,z}^2 - 2\int_{t_i}^{T_s} E_s(t)k_z(t)dt} - k_{0,z} + \alpha A_s(t_i)}{\alpha E_s(t_i)} \tag{3.37}$$

for the exact solution. One may note that in both formulas the upper limit of the integrals has been replaced by T_s, i.e., the pulse duration of the streaking field, which is valid since $E_s(t) = 0$ for $t \geqslant T_s$.

In order to show the accuracy of the predictions of the two classical approaches and also the relation between the propagation time delay and the streaking time delay, we compare in Fig. 3.11 the results of quantum streaking simulations (black circles) for the streaking time delay Δt_s with the classical predictions, Eq. (3.36) (blue dashed lines) and Eq. (3.37) (red solid lines), for photoionization of an electron in (a) the 1D Coulomb potential $V_{\text{C}}(z)$, Eq. (3.20), with $Z = 3.0$ and

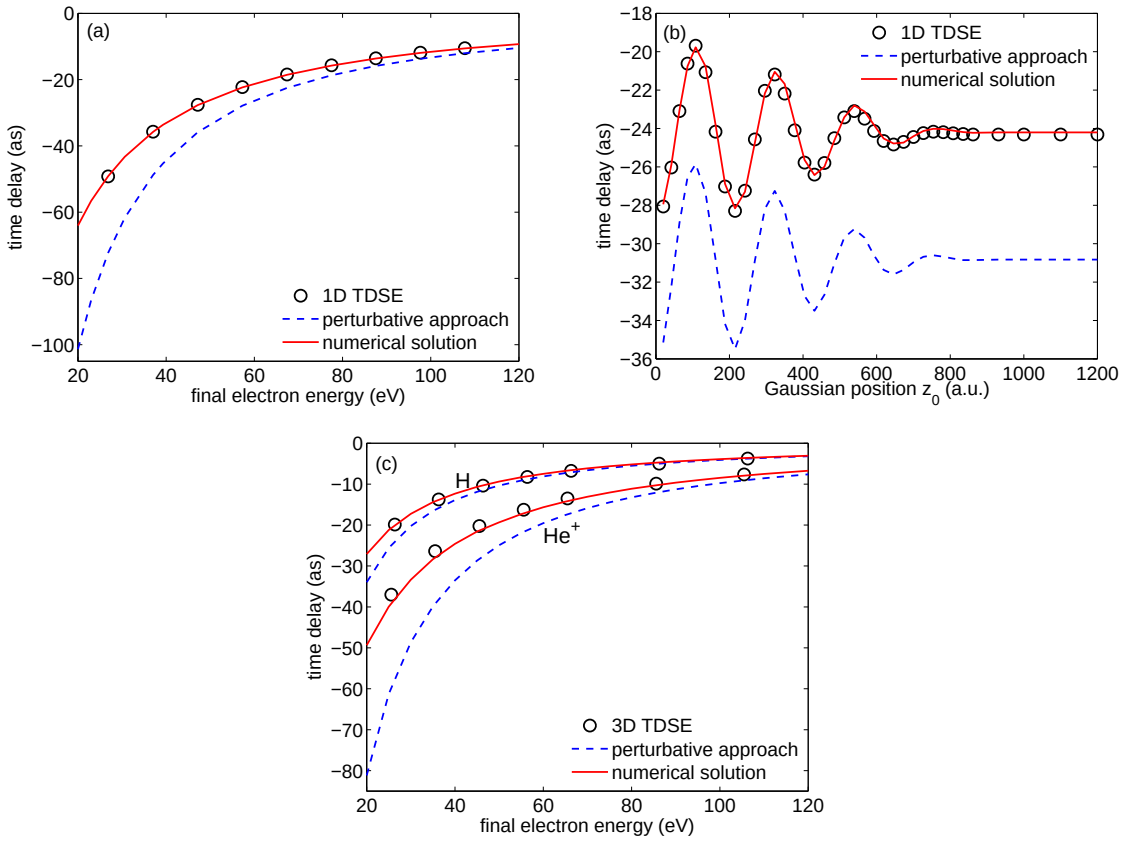

Figure 3.11: Comparison of streaking time delays from quantum streaking simulations (black circles) with classical results from the perturbative approach (blue dashed lines) and the full numerical solution (red solid lines). In our analysis we considered three potentials: (a) 1D Coulomb potential $[V_{\mathrm{C}}(z)]$, (b) the combination of 1D Coulomb and Gaussian potentials $[V_{\mathrm{CG}}(z)]$, (c) 3D Coulomb potential $[V(\boldsymbol{r})]$.

$a = 2.0$, (b) the combination of 1D Coulomb and Gaussian potentials (the electron was initially bound in the ground state of the Coulomb potential)

$$V(z) = V_{\mathrm{CG}}(z) = -\frac{Z}{\sqrt{z^2 + a}} + V_0 e^{-\left(\frac{|z|-z_0}{\sigma}\right)^2}, \tag{3.38}$$

with $Z = 3.0$ and $a = 2.0$ for the Coulomb potential, and $V_0 = -0.5$, $\sigma = 2.0$ for the Gaussian potential centered at z_0, and (c) a 3D Coulomb potential of the form

$$V(\boldsymbol{r}) = -\frac{Z}{r}, \tag{3.39}$$

with $Z = 1.0$ and 2.0 for H atom and He ion, respectively.

The streaking time delays Δt_s in the 1D quantum simulations are obtained by scanning the central cycle of the streaking field and then fitting the trace using Eq. (3.28). To ionize the electron initially bounded in the 1D Coulomb potential, we have used an XUV pulse with $I_{\mathrm{XUV}} = 1 \times 10^{15}$ W/cm^2, $\omega_{\mathrm{XUV}} = 100$ eV, $T_{\mathrm{XUV}} = 600$ as, and $\phi_{\mathrm{XUV}} = -\pi/2$. The parameters of the streaking pulse were $I_s = 1 \times 10^{12}$ W/cm^2, $\lambda_s = 800$ nm, $N_s = 3$ [Fig. 3.11(a)] or 8 [Fig. 3.11(b)], and $\phi_s = -\pi/2$. The 3D quantum results in Fig. 3.11(c) were extracted from Ref. [37]. In the classical calculations we assumed a transition to the continuum at the center of the XUV pulse (i.e., $t_i = \tau = T_{\mathrm{XUV}}/2$).

It has been previously shown (e.g., [37, 38]) that the results of classical streaking simulations depend on the choice of the initial position z_i. We have chosen z_i to be the most probable position of the electron in the initial state [e.g., $x_i = 0$ for $V_{\mathrm{CG}}(z)$]. Alternatively, one can sample the initial conditions in Monte-Carlo calculations (see, e.g., [37]). To make use of the classical analysis we further note that the propagation time delay Δt_{prop} in Eqs. (3.36) and (3.37) depends on the choice of α. We determine α such that Δt_{prop} remains approximately constant while varying t_i over one field cycle (solid line with squares in Fig. 3.12). Please note that, independent of the choice of α, our classical prediction for Δt_{prop} diverges for $E_s = 0$. In practice, we can actually extract the propagation time delay Δt_{prop} directly from the classical streaking trace by using the fitting method. We have tested that this alternative method leads to the same time delays as those using the time delay formula Eq. (3.36) or (3.37).

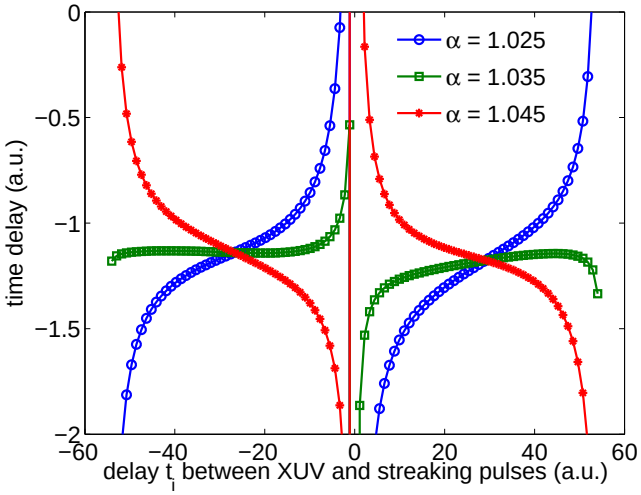

Figure 3.12: Classical predictions for the time delay as a function of the delay t_i between XUV ionizing and IR streaking pulses for different fitting parameter α by using Eq. (3.37). Calculations are performed for the 1D potential $V_{\rm CG}(z)$ in Eq. (3.38) with $Z = 3.0$, $a = 2.0$, $V_0 = -0.5$, $\sigma = 2.0$, and $z_0 = 20$.

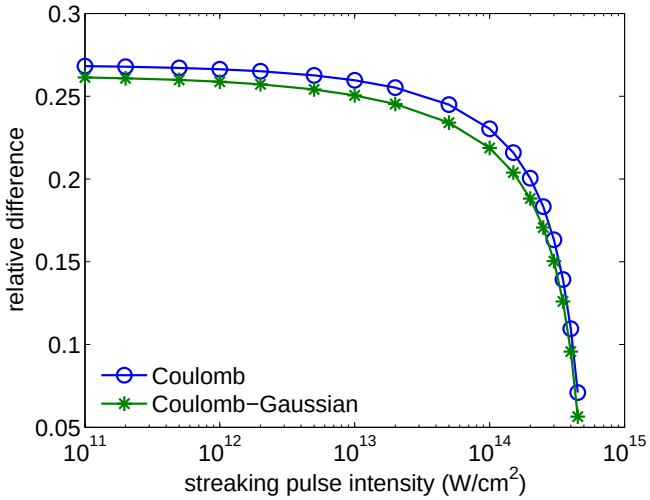

Figure 3.13: Relative difference between momentum shift Δk calculated classically from the perturbative approach and the full numerical solution for $V_{\rm C}(z)$ (blue solid line with circles) and $V_{\rm CG}(z)$ ($z_0 = 200$, green solid line with stars). The relative difference is defined as $|(\Delta k^{(\rm pert)} - \Delta k^{(\rm numerical)})/\Delta k^{(\rm numerical)}|$. We have considered photoemission of an electron with final asymptotic momentum of 2.0, which is streaked by a 3-cycle 800 nm laser pulse.

The comparison in Fig. 3.11 reveals that the results of the quantum streaking simulations (black circles) and the full classical calculations (red solid lines) are in excellent agreement with each other. In the present set of calculations the difference between the quantum and full classical results does not exceed 2 as, which shows that the numerical streaking simulations can be well analyzed and interpreted using a classical approach. Such a conclusion has also been reached based on the results of classical trajectory Monte Carlo calculations in Ref. [37]. This indicates that the transition of the electron from the bound state into the continuum occurs instantaneously upon application of the XUV pulse (i.e., most likely at the center of the XUV pulse) and the observed temporal offset Δt_s, or time delay, arises due to the propagation of the photoelectron in the continuum.

On the other hand the comparison further shows that the results of the perturbative classical approach (blue dashed lines) agree neither with those of the quantum simulations (black circles) nor with the full classical calculations (red solid lines). We find discrepancies of more than 30 as as compared to the quantum results and the full classical results in some of our present calculations [e.g., the low energy part in Fig. 3.11(a)]. This degree of deviation between the two classical approaches persists for intensities of the streaking field up to 10^{14} W/cm^2. We exemplify this by showing in Fig. 3.13 the relative difference between the results for the momentum shift Δk, obtained from the two classical approaches for both $V_{\mathrm{C}}(z)$ (blue solid line with circles) and $V_{\mathrm{CG}}(z)$ (green solid line with stars). We note that, in general, results of the perturbative approach and the full numerical solution only tend to agree for high streaking field intensities, which would induce ionization from the target by the streaking field itself.

We can therefore further conclude that the discrepancy between the results of the perturbative classical approach and the quantum streaking simulations does arise from the first-order approximation of the Coulomb potential, but not from the use of classical theory itself. The transition of the electron from the bound state into the continuum in photoionization occurs at distances at which the perturbation condition $|E_s| \gg |\frac{dV}{dz}|$ is not fulfilled for moderate streaking field strengths. This conclusion is further supported by the results for the combination of Coulomb and Gaussian potentials [$V_{\mathrm{CG}}(z)$]. In this case the final time delay has two contributions, one resulting from the

Coulomb potential and the other from the rather weak Gaussian potential. In test calculations we studied both contributions independently and found that in the present results the deviation between the two classical results arises from the Coulomb potential alone. This can be also seen from the results in Fig. 3.11(b) as the difference between the two classical results is independent of the position of the Gaussian potential.

Before proceeding, we may briefly discuss the option to extend the perturbative classical result for the analysis of streaking calculations. The deviations found for the first-order approximation can be significant. It remains to be studied if higher-order corrections can improve the results sufficiently or a non-perturbative treatment becomes necessary. Instead, it might be more interesting to partition the space into an inner region close to the nucleus and an outer region, in which $|E_s| \gg |\frac{dV}{dz}|$ is fulfilled for the outer one. Then, an application of the perturbative result for the time delay related to the outer region appears to be satisfied. We may point out that the (perturbative) eikonal approximation was indeed initially introduced in the context of strong-field ionization [84]. For strong fields, in contrast to weak-field photoionization, the perturbative condition is usually well satisfied for distances beyond the tunnel exit, at which the electron enters the continuum. Results of previous theoretical calculations [58] indicate that it might be then useful to approximate the time delay in the inner region by the WS time delay for the short-range part of the potential. Of course, the quality of such an approximation should depend on the potential of interest, the streaking field strength and other parameters, which would determine the partition between inner and outer region and the range of short- vs. long-range parts of the potential. We do not further investigate this option, since the full classical solutions are in excellent agreement with the present quantum streaking results and therefore provide a good starting point for our further analysis.

3.2.3 Physical interpretation of streaking time delay in single-photon ionization

We have just shown [81, 85, 86] that for the single-photon ionization process the streaking time delay only arises from the propagation of the photoelectron in the combined potential of the

streaking and the atomic fields, i.e.,

$$\Delta t_s = \Delta t_{\text{prop}}. \tag{3.40}$$

This implies that there is no contribution of the WS time delay Δt_{WS} in the streaking time delay Δt_s, which however does not agree with previous interpretations that claim the streaking experiment is related to an intrinsic Δt_{WS}. In order to seek for an alternative physical interpretation for Δt_s and also see whether or not Δt_s can be related to Δt_{WS}, we make use of the relation in Eq. (3.40) and further simplify the accurate propagation time delay formula, Eq. (3.37). Noting that the second term of the square root in Eq. (3.37) is usually small, we can expand the square root to first order. Assuming $\alpha = 1$, we obtain

$$\Delta t_s = \Delta t_{\text{prop}} \simeq \frac{1}{E_s(t_i)} \int_{t_i}^{T_s} E_s(t) \left[1 - \frac{k_z(t)}{k_{0,z}}\right] dt, \tag{3.41}$$

which still provides accurate results for liberation of the electron at the peak of $E_s(t)$ within its central cycle as found in test calculations.

To avoid evaluating $k_z(t)$ by numerically solving the Newton's equation, we approximate it using

$$k_z(t) \simeq k_z^{(0)}(t) - A_s(t_i) + A_s(t), \tag{3.42}$$

where $k_z^{(0)}(t)$ is the momentum of the electron in the field-free atomic potential. This approximation is based on the assumption that the coupling effect of the streaking field and the atomic potential on the momentum is negligible and its accuracy can be seen from results in Fig. 3.14. Within this approximation, Eq. (3.41) then yields

$$\begin{aligned} \Delta t_s &\simeq \frac{1}{E_s(t_i)} \int_{t_i}^{T_s} E_s(t) \left[1 - \frac{k_z^{(0)}(t)}{k_{0,z}}\right] dt + \frac{A_s(t_i)^2}{2E_s(t_i)k_{0,z}} \\ &\simeq \frac{1}{E_s(t_i)} \int_{t_i}^{T_s} E_s(t) \left[1 - \frac{k_z^{(0)}(t)}{k_{0,z}}\right] dt, \end{aligned} \tag{3.43}$$

where in the second step we have assumed that the electron is liberated at the peak of $E_s(t)$, i.e., at $A_s(t_i) = 0$. It is now instructive to further rewrite Eq. (3.43) as a sum by assuming that the streaking field and the electron momentum are approximately constant in the time interval

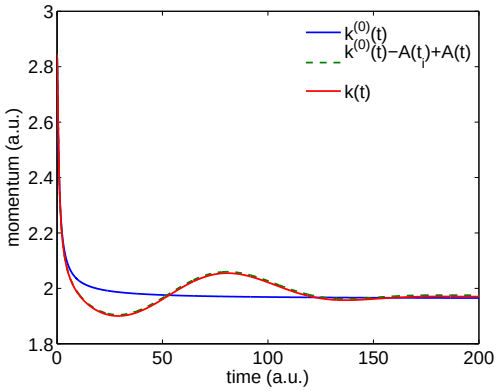

Figure 3.14: Comparison of momenta calculated using different methods: full numerical solution of the Newton's equation (red solid line) and Eq. (3.42) (green dashed line). We have considered an electron propagating in the combined potential of the 1D Coulomb potential $V_{\mathrm{C}}(z)$ and a 3-cycle 800 nm streaking pulse with $I_s = 1 \times 10^{12}$ W/cm^2. As a reference the field-free momentum $k^{(0)}(t)$ of an electron propagating in $V_{\mathrm{C}}(z)$ is also shown as blue solid line.

$[t_j, t_j + \delta t]$, i.e., $E_s(t) \simeq E_s(t_j)$ and $k_z^{(0)}(t) \simeq k_z^{(0)}(t_j)$,

$$\begin{aligned} \Delta t_s &\simeq \frac{1}{E_s(t_i)} \sum_{j=1}^{N} E_s(t_j) \left[1 - \frac{k_z^{(0)}(t_j)}{k_0} \right] \delta t \\ &= \sum_{j=1}^{N} \frac{E_s(t_j)}{E_s(t_i)} \Delta t_{\text{field-free}}^{(j)}, \end{aligned} \tag{3.44}$$

where $\Delta t_{\text{field-free}}^{(j)}$ is a piecewise field-free time delay that the electron accumulates during its propagation in the time interval $[t_j, t_j + \delta t]$ and over a related finite region $[z_j, z_j + \delta z]$ of the potential $V(z)$ as compared to the propagation of a free particle over the same distance in space.

Eq. (3.44) provides us with an interesting interpretation of the streaking time delay: It is neither the WS time delay Δt_{WS} nor the simple sum of finite-range piecewise field-free time delays. Instead, the piecewise field-free time delays are weighted by the streaking field strength present when the electron wavepacket propagates over the corresponding part of the potential. Thus, we can conclude that the streaking time delay strongly depends on the electron dynamics in the coupled atomic and time-varying streaking field potential.

Eq. (3.44) further indicates that in certain theoretical limits Δt_s can approach the WS time delay Δt_{WS}. In particular, for short-range potentials $V(\boldsymbol{r})$, Δt_s is approximately given by the first

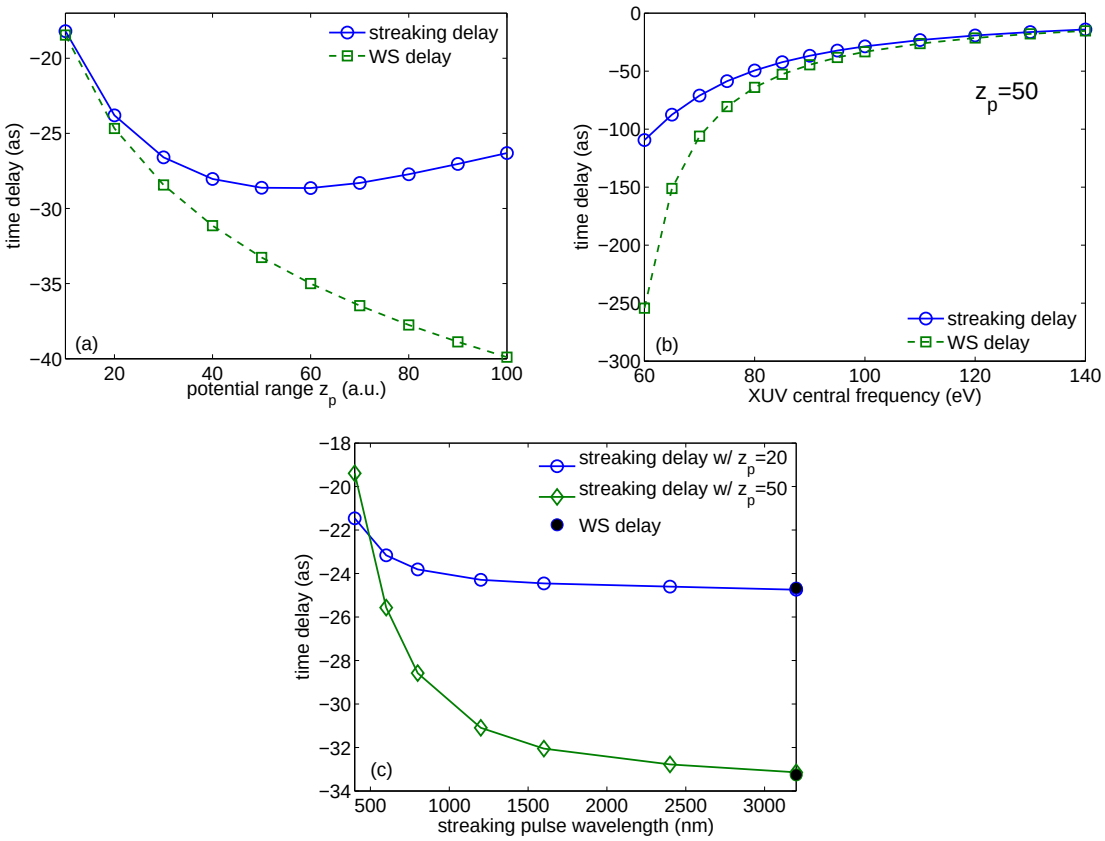

Figure 3.15: Results of numerical simulations for the streaking time delays Δt_s (solid line with circles and diamonds) as a function of (a) the range x_p of a short-range potential, (b) the frequency of the ionizing XUV field, and (c) the wavelength of the streaking pulse are compared with those for the Wigner-Smith time delay [dashed lines with squares in (a) and (b) and solid circles in (c)]. Laser parameters are: $I_{\rm XUV} = 1 \times 10^{15}$ W/cm^2, $T_{\rm XUV} = 600$ as, $\omega_{\rm XUV} = 100$ eV [(a) and (c)], $\phi_{\rm XUV} = -\pi/2$, $I_s = 1 \times 10^{12}$ W/cm^2, $N_s = 3$ cycle [(a) and (b)], $T_s = 32.02$ fs [(c)], $\lambda_s = 800$ nm [(a) and (b)], and $\phi_s = -\pi/2$.

term (i.e., $j = 1$) of the sum in Eq. (3.44) if the electron wavepacket propagates over the full range of the potential during $[t_i, t_i + \delta t]$ while $E_s(t) \simeq E_s(t_i)$. This condition should be fulfilled in the following theoretical limits: (a) the effective range of $V(\boldsymbol{r})$ goes to zero, (b) the momentum of the electron goes to infinity, or (c) the oscillation period of the streaking field goes to infinity. To test our expectations we performed simulations for the following 1D potential:

$$V(z) = V_{\text{C-WS}}(z) = -\frac{Z}{\sqrt{z^2 + a}} \frac{1}{1 + e^{(|z| - z_p)/b}}, \tag{3.45}$$

which is a product of Coulomb and Woods-Saxon potentials, where z_p determines the effective range of the potential. We have chosen $b = 1$ and $z_p \geqslant 10$ such that $V_{\text{C-WS}}(z) \simeq V_{\text{C}}(z)$ for $|z| < z_p$, while $V_{\text{C-WS}}(z)$ approaches zero quickly for $|z| > z_p$. To obtain the WS time delays, we used the back-propagation method introduced in the last section. In Fig. 3.15 we compare the results of the numerical simulations for Δt_s (solid lines with circles and diamonds) as a function of (a) the potential range z_p, (b) the frequency of the ionizing XUV pulse, and (c) the wavelength of the streaking pulse with the WS time delay Δt_{WS} (dashed lines with squares for (a) and (b) and solid circles for (c)). All other parameters of the fields are kept the same in the simulations. As expected, Δt_s approaches Δt_{WS} in each of the three theoretical limits listed above. One may notice that for limit (a) a quantum proof based on the eikonal approximation was given in Ref. [38], in which the authors obtained a similar conclusion that the propagation (or coupling) time delay is equal to the WS time delay for a short-range potential.

As mentioned above, in earlier work (e.g, [38, 53, 58]) for the long-range Coulomb interaction the streaking time delay was often separated into the sum of the field-free WS time delay and a contribution accounting for the coupling. Although we do not derive such a relation, we note that in Eq. (3.44) $E_s(t_1) \simeq E_s(t_i)$ and therefore the first term of the sum is equal to the field-free time delay, which the electron acquires during $[t_i, t_i + \delta t]$. The corresponding 'field-free' delay distance over which the electron travels during this time interval depends on the electron energy (or, XUV frequency) and the wavelength of the streaking field. In Fig. 3.16 we present classical estimations for this distance by assuming that the electron is emitted at the peak of a 3-cycle 800

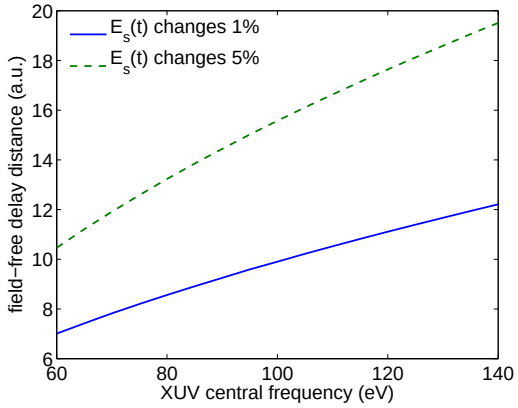

Figure 3.16: Classical estimates for the 'field-free' delay distance of an electron, released at the peak of a three-cycle streaking pulse (wavelength of 800 nm) in the 1D Coulomb potential, as a function of the XUV photon energy. This distance was determined by the position of the electron at the time instant when the streaking field changed to 99% (solid line) and 95% (dashed line) of the peak field strength.

nm laser pulse. We note that the calculated 'field-free' delay distances are approximately equal to short-range distances of atomic potentials.

The sum rule, $\Delta t_s = \Delta t_{\rm WS} + \Delta t_{\rm prop}$, used for the interpretation of the streaking time delays appears to work for many systems and to some extent is related to our present interpretation, Eq. (3.44). However, we want to emphasize that our interpretation is essentially different from the previous one: We have demonstrated that the streaking time delay only arises from the propagation of the electron in the combined continuum of the streaking and ionic potentials, or alternatively the coupling effect, while previously it was believed that an intrinsic WS time delay needs to be added.

With our present interpretation, we are also able to answer the question whether or not for a short-range potential there is a contribution from the field coupling to the streaking time delay. As mentioned above, consistent with our results, Ivanov *et al.* [38] showed that for a short-range potential (e.g., the short-range part of the neon potential) there exists a propagation (coupling) time delay and it is equal to the WS time delay by applying the eikonal approximation. However, in Ref. [53], Nagele *et al.* pointed out that this conclusion cannot be supported by numerical

simulations when comparing Δt_s with $\Delta t_{\rm WS} + \Delta t_{\rm prop}$. The latter quantity was shown to be twice as large as the streaking time delay Δt_s [53]. Based on the sum rule, it was claimed by Nagele *et al.* [53] that $\Delta t_{\rm prop} = 0$, i.e., no contribution due to the field coupling exists for a short-range potential. From our analysis, it is obvious that this incorrect conclusion in Ref. [53] arises due to the use of the sum rule, which is only an assumption and has never been rigorously proven. For such a short-range potential considered in Refs. [38, 53], to reproduce the streaking time delay Δt_s, one can use either the propagation time delay $\Delta t_{\rm prop}$ or the WS time delay $\Delta t_{\rm WS}$, but never both of them because the physical origin of $\Delta t_{\rm WS}$ is the propagation (or coupling) effect, which however approaches the WS time delay for a short-range potential [see Fig. 3.15(a)].

Before proceding, we note that more subtle features in our results, such as the oscillations in Fig. 3.11(b) and the change from a decrease to an increase in Δt_s as a function of z_p in Fig. 3.15(a) can also be well understood with our classical interpretation, Eq. (3.44). The oscillations in Fig. 3.11(b) are caused by the Gaussian potential, which has a very short effective range. The streaking delay contribution due to the Gaussian potential can be therefore written as

$$\Delta t_s^{\rm G}(z_0) \simeq \frac{E_s(t_{\rm G})}{E_s(t_i)} \Delta t_{\rm WS}^{\rm G}, \tag{3.46}$$

where t_i and $t_{\rm G}$ are the instant of ionization and the time instant at which the electron reaches the Gaussian potential respectively. Thus, the streaking time delay induced by the coupling of the streaking field and the Gaussian potential should have an oscillation period proportional to that of the streaking field, which can be easily confirmed from the results in Fig. 3.11(b) by noting that $t_{\rm G} \simeq z_0/k_0$. On the other hand, the non-monotonic behavior of the streaking time delay in Fig. 3.15(a) can be also explained by Eq. (3.43). Assuming that the electron is ionized at the peak of the streaking field, the absolute value of the time delay is expected to increase over the first quarter of the streaking field cycle. However, then the field changes sign and the absolute value should start decreasing. The turning point at $z_p = 50$ agrees well with the classical estimate for the distance the electron travels within the first quarter cycle after its release, namely $z_{\rm wp} = k_0 T_{\rm s}/4 = 54$ at the present parameters.

3.2.4 Finite-range time delay and its application to imaging

Up to now we have established a new physical interpretation for the time delay measured in the streaking experiment, which explains the streaking time delay as a sum of field-weighted field-free time delays. As pointed out above, one important consequence of this interpretation is that, in general, the WS time delay does not present or contribute to the streaking time delay. From Eq. (3.43), one clear sees that the coupling effect is present during the time interval of $[t_i, T_s]$, i.e., between the ionization time and the end of the streaking field, which is in contrast to the original definition of the WS time delay in which the propagation region extends to infinity. In order to further support such a conclusion, we present results of numerical simulations of streaking scenarios for the Coulomb-Gaussian potential, Eq. (3.38), in which the position of the Gaussian potential can be changed to test the effective region that affects the streaking time delay.

We consider photoemission from the ground state of the 1D Coulomb potential $V_{\mathrm{CG}}(z)$ with $Z = 3.0$ and $a = 2.0$ by an XUV pulse with $I_{\mathrm{XUV}} = 1 \times 10^{15}$ W/cm^2, $\omega_{\mathrm{XUV}} = 100$ eV, $T_{\mathrm{XUV}} = 600$ as, and $\phi_{\mathrm{XUV}} = -\pi/2$. The parameters of the streaking pulse are $I_s = 1 \times 10^{12}$ W/cm^2, $\lambda_s = 800$ nm, and $\phi_s = -\pi/2$. In Fig. 3.17(a), we show the extracted values for the streaking time delay Δt_s (stars, squares, and circles) for different positions z_0 of the Gaussian potential and a streaking pulse having 8 cycles. The streaking time delay Δt_s strongly varies when the Gaussian potential is located close to the center of the Coulomb potential and the amplitude of this variation increases with an increase of the depth of the Gaussian potential. However, independent of the strength of the Gaussian potential, Δt_s remains constant for $z_0 > z_{\mathrm{finite}} \simeq 850$, for which we obtain the same numerical result with and without (diamond) the Gaussian potential. Our simulations show that at the end of the streaking pulse the center of the outgoing electron wave packet is located at $z_{\mathrm{finite}} \simeq 850$. Thus, Δt_s accounts for the presence of the Gaussian potential only when the electron wave packet reaches the potential before the interaction with the streaking pulse ceases. This is, as expected, in contrast with the WS time delay that accounts for the potential up to infinity based on its original definition.

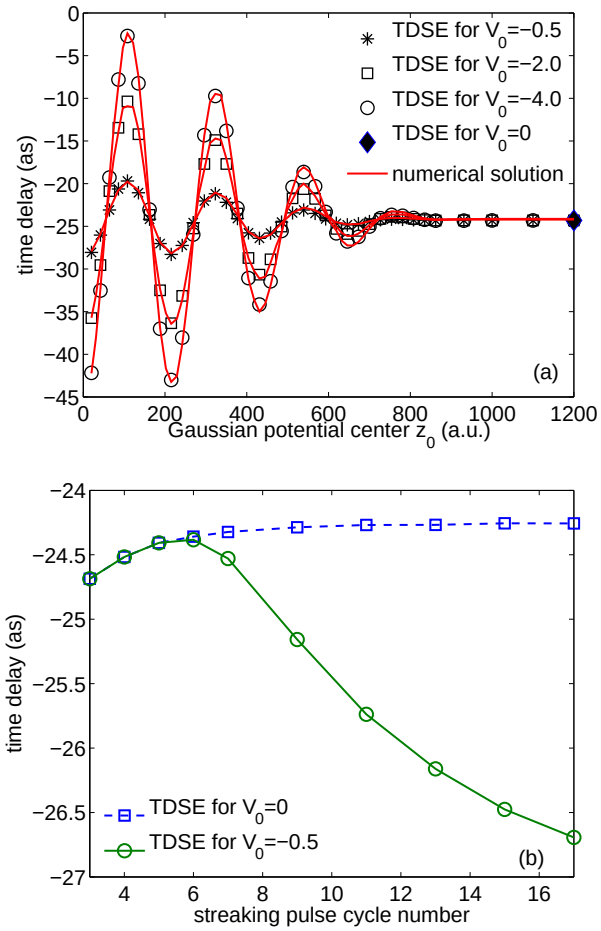

Figure 3.17: (a) Streaking time delay Δt_s as a function of the position z_0 of the Gaussian potential. We compare results of TDSE simulations (stars, squares, and circles for $V_0 = -0.5, -2.0$, and -4.0, respectively) with those of classical calculations, Eq. (3.37) (red solid lines). Also shown is the TDSE result without Gaussian potential (diamond on the right end). In the classical calculations the parameter α varies between 0.985 and 1.084. (b) Comparison of Δt_s from TDSE calculations for different cycle numbers of the streaking pulse with (green solid line with circles) and without (blue dashed line with squares) the Gaussian potential. The Gaussian potential is located at $z_0 = 650$. Other parameters are given in the text.

Table 3.3: Streaking time delays for different time intervals $[t_1, t_2)$ of the streaking trace. An 8-cycle streaking pulse and two 1D potentials [$V_{\rm C}(z)$ and $V_{\rm CG}(z)$ ($z_0 = 650$)], have been used for the TDSE simulations. All values in this table are given in a.u..

$[t_1, t_2)$	Coulomb	Coulomb-Gaussian
$[-400, -200)$	-0.9867	-1.3855
$[-200, 0)$	-0.9985	-1.0765
$[0, 200)$	-1.0085	-1.0130
$[200, 400]$	-1.0250	-1.0250

To further confirm that it is the propagation distance of the electron during the presence of the streaking field that determines the probing distance of the attosecond streak camera, we determine Δt_s for streaking pulses having different durations while the Gaussian potential remains located at $z_0 = 650$. For short streaking pulses ($N_s \leqslant 5$) we again obtain the same results for Δt_s in simulations with [Fig. 3.17(b), green solid line with circles] and without (blue dashed line with squares) the Gaussian potential. In each of these simulations the outgoing wave packet is located at $z < z_0 = 650$ at the end of the streaking pulse. In contrast, as soon as the outgoing wave packet reaches z_0 for $N > 5$, Δt_s deviates from the result obtained in simulations without the Gaussian potential.

According to our analysis the streaking time delay Δt_s depends on the time interval between transition of the electron into the continuum, t_i, and the end of the streaking pulse, T_s. We therefore expect that for a long streaking pulse the time delay, extracted from different cycles of the streaking pulse, varies, since for emission of the electron by the XUV pulse in the raising part of the streaking pulse it will propagate over a larger distance until the streaking pulse ceases as compared to the case when the electron is released in the trailing part of the streaking pulse.

To test our expectations we have performed quantum streaking simulations for the 1D Coulomb potential $V_{\rm C}(z)$, Eq. (3.20), and the combination of 1D Coulomb and Gaussian potentials $V_{\rm CG}(z)$, Eq. (3.38), using an 8-cycle streaking pulse. We then extract the time delay Δt_s by fitting the streaked momentum over different intervals of the streaking pulse using Eq. (3.28). The results are shown in Table 3.3, where negative times in the interval $[t_1, t_2)$ correspond to the raising part

of the pulse, while positive times correspond to the trailing part of the pulse.

As expected, the extracted streaking time delay depends on the interval used for the fitting procedure. In the case of the 1D Coulomb potential the variation of the time delays over the streaking pulse is rather small. This indicates that the major part of the time delay is accumulated shortly after the transition of the electron into the continuum near to the nucleus, where the potential is strongest. In contrast for the combined Coulomb-Gaussian potential we see a strong change of the time delay for application of the XUV pulse at the beginning of the streaking pulse as compared to the other fitting intervals. This can be understood within our interpretation of the time delay. If the electron is ionized early, it reaches the Gaussian potential during its propagation at large streaking pulse field strengths. According to Eq. (3.44), this part of the potential therefore contributes significantly to the accumulated time delay. On the other hand, if the electron is ionized later, it reaches the Gaussian potential either when the streaking pulse is weak or after the end of the streaking pulse (i.e., for the interval $[200, 400]$). In these cases the effect of the Gaussian potential on Δt_s is small or not present at all, in agreement with Eq. (3.44). The results therefore again confirm the finite-range property of the observed time delays. Furthermore, they actually open a possibility to use the streaking technique to image the presence and even the position of an additional potential (here, the Gaussian potential) within a long streaking pulse.

Previously, we have considered 1D examples which already reveal important aspects of the physics behind the streaking measurement technique. We will now investigate the role of the polarization direction in view of the finite-range property of the time delay and the detection of a static potential at a distance from the location of the photoemission. To this end we consider the following 2D potentials

$$V_1(x,y) = \begin{cases} -\frac{Z}{\sqrt{r^2+a}} - V_{0,1} e^{-\frac{(r-r_0)^2}{\sigma^2}} & \text{for } |x| \leqslant 100, \\ -\frac{Z}{\sqrt{r^2+a}} & \text{for } |x| > 100, \end{cases} \tag{3.47}$$

$$V_2(x,y) = -\frac{Z}{\sqrt{r^2+a}} - V_{0,2} e^{-\frac{(r-r_0)^2}{\sigma^2}} \frac{y^2}{r^2}, \tag{3.48}$$

where $r = \sqrt{x^2+y^2}$. Both potentials are shown in Fig. 3.18 for $Z = 2.0$, $a = 0.164$, $V_{0,1} = 0.5$,

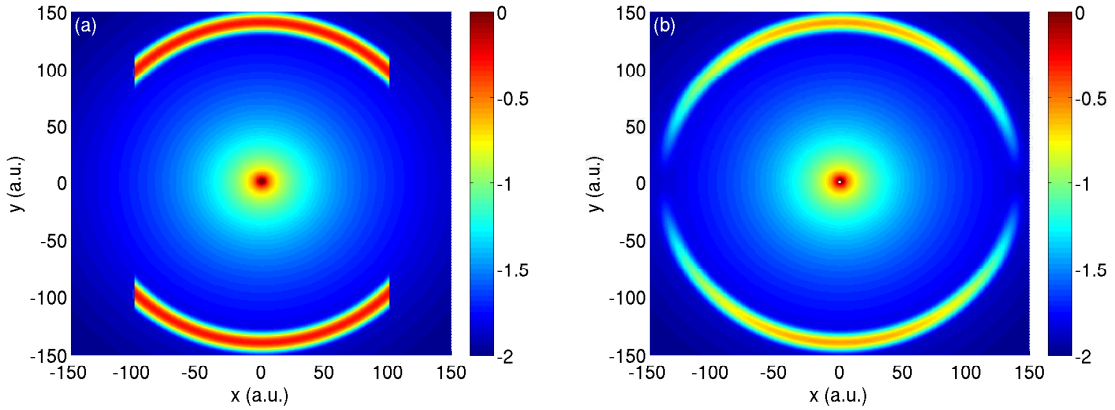

Figure 3.18: 2D model potentials, as defined in Eq. (3.47) [(a)] and Eq. (3.48) [(b)], plotted on a logarithmic scale as $\log[-V(x,y)]$.

$V_{0,2} = 0.25$, $r_0 = 140$, and $\sigma = 5.0$. In our calculations the electron is initially bounded in the ground state of the Coulomb potential with an eigenenergy of -2.0. We then used an XUV pulse with $I_{\rm XUV} = 1 \times 10^{14}$ W/cm^2, $\omega_{\rm XUV} = 68$ eV, $N_{\rm XUV} = 10$, and $\phi_{\rm XUV} = -\pi/2$ and a 3-cycle 400 nm streaking pulse with $I_s = 1 \times 10^{12}$ W/cm^2 and $\phi_s = -\pi/2$ to streak the momentum of the photoelectron. The TDSE is solved using a space-time grid with $\Delta x = \Delta y = 0.3$, $N_x = N_y = 5000$, and $\Delta t = 0.05$ in 2D Cartesian coordinates. The polarization of ionizing and streaking pulses are kept parallel, but the polarization direction with respect to the orientation of the potentials is varied.

To obtain the streaking trace as a single curve as in Fig. 1.7(a), we first perform a 2D Fourier transform of the ionizing part of the wave function at the end of each simulation for a given time delay between the XUV and streaking pulses. This 2D momentum distribution is then integrated over a small opening angle ($\pm 5^\circ$) with respect to the polarization direction of the co-aligned ionizing and streaking pulses, since the streaking effect is expected to be strongest along the polarization direction of the streaking pulse [37]. Next, we obtain the expectation value of the resulting momentum distribution for a given time delay τ. Finally, by repeating the calculations for application of the XUV ionizing pulse over the central cycle of the streaking pulse we obtain the desired streaking trace as a function of the time delay between the two pulses and determine

the temporal offsets by comparison with the vector potential as before in the 1D cases. We have propagated all wave packets for different XUV-streaking delays to the same distance in space, therefore the conclusions based on the qualitative behavior of the results presented below do not depend on the particular choice of wave function used for calculating the momentum distributions.

In Fig. 3.19(a) we present streaking time delays as a function of the number of cycles in the streaking pulse for the 2D potential defined in Eq. (3.47). We compare results obtained for the full potential in which the pulses are either polarized in x- (green line with stars) or in y-direction (red line with squares) with those in which we neglect the additional Gaussian potential at a distance from the Coulomb potential (blue line with circles). Due to the spherical symmetry of the pure 2D Coulomb potential, in the latter case the results are independent of the choice of the polarization direction and we therefore show the results obtained for polarization along the x-direction only. In contrast, with the additional Gaussian potential the results strongly depend on the polarization direction. While the streaking time delays with and without additional potential agree with each other for polarization of the streaking field along the x-direction, they start to deviate from $N = 6$ on for polarization in y-direction. The latter behavior is similar to the 1D example studied before. The difference in the results is due to the fact that the time delay is determined by the photoelectron dynamics in the coupled field of the atomic potential and the streaking field along the polarization direction. For short streaking pulses the photoelectron does not reach the location of the additional Gaussian potential and the effect of the latter is therefore negligible, while for longer pulses the coupling effect between the streaking field and the additional Gaussian potential becomes present. The additional model potential is present along the y-polarization but not in x-direction in agreement with our observations for the different polarization directions of the field.

Next, in Fig. 3.19(b) we show the results obtained for the second 2D potential, Eq. (3.48). Time delays for the full potential and different polarizations of the co-aligned ionizing and streaking pulses (polarization in x-direction: green line with stars, at 45°: cyan line with crosses, and in y-direction: red line with squares) are compared with those obtained without additional potential

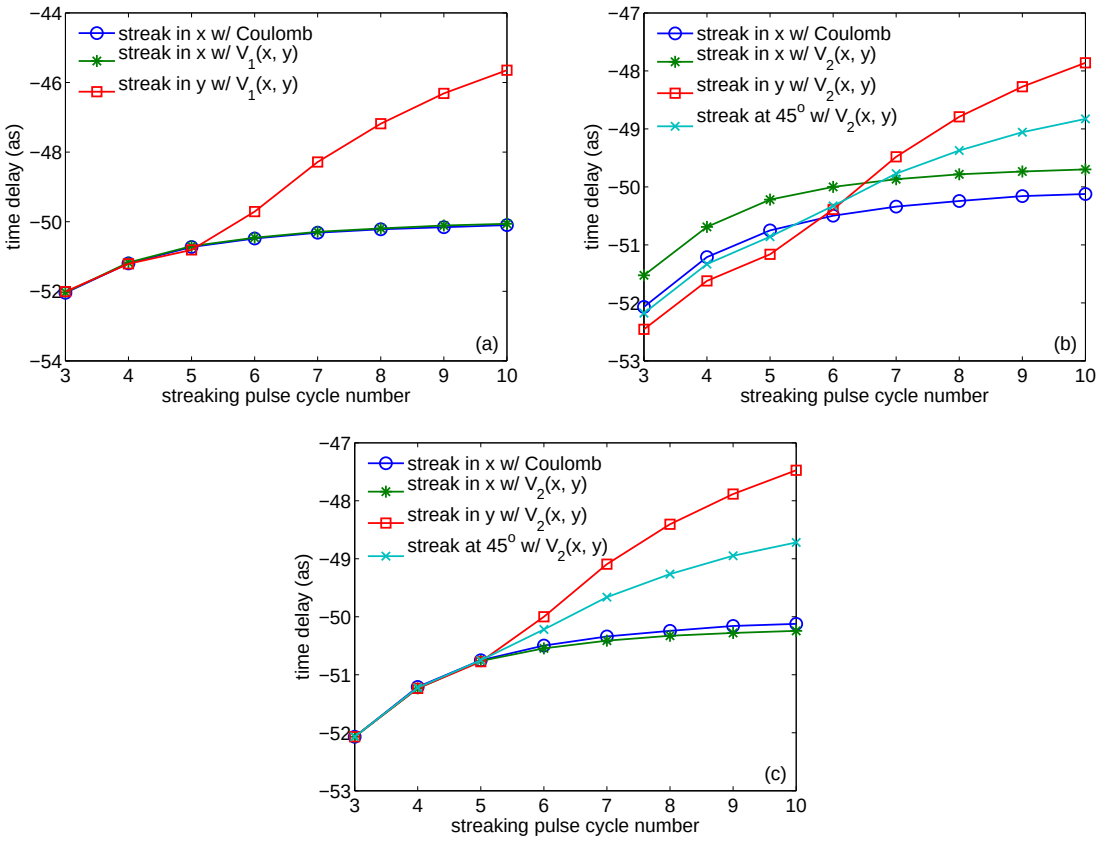

Figure 3.19: Time delay as a function of streaking pulse cycle number for the 2D potentials defined in Eq. (3.47) [(a)] and Eq. (3.48) [(b) and (c)] and polarizations of the streaking (and co-aligned XUV ionizing) field in x-direction (green line with stars), at 45° (cyan line with crosses), and in y-direction (red line with squares). The results are compared with those for the pure 2D Coulomb potential without the additional potential (blue line with circles) and a streaking field polarized in x-direction. In (c), the original streaking time delays for the 2D potential, Eq. (3.48) as shown in (b), have been shifted to match the result for the shortest streaking pulse for the pure 2D Coulomb potential.

(blue line with circles). We note that in this case the time delays do not coincide with each other, even for short streaking pulses, for which the photoelectron wave packet does not reach the additional potential when the streaking pulse ceases. Further analysis reveals that this discrepancy can be explained as due to the scattering of the photoelectron at the additional potential, which leads to different final momentum distributions as compared to that of the pure 2D Coulomb potential case. In order to remove this scattering effect, we shift all time delay curves such that the results match for the shortest streaking pulse. The resulting modified time delays, shown in Fig. 3.19(c), then reveal again the finite-range property since the curves deviate for $N > 5$. We furthermore observe that the degree of deviation increases as the additional potential along the polarization direction gets stronger.

3.2.5 Influences of pedestal and additional static field

So far, we have considered streaking pulses with a $\sin^2$-envelope, which is only an ideal assumption for theoretical convenience. In practice the shape of the streaking pulse is usually not regular and sometimes has an oscillating tail. According to the classical analysis, Eq. (3.44), the streaking time delay however depends on the instantaneous field strength during the propagation of the electron in the continuum. It is therefore interesting to study if and how the shape of the streaking field envelope influences the observed time delays. In order to study this aspect we make use of the following pulse envelope

$$E_{\mathrm{env}}(\beta_p, T_p) =$$

$$\begin{cases} E_0 \sin^2(\pi t/T_s) & \text{for} \quad 0 \le t \le T_s/2, \\ (1-\beta_p) E_0 \sin^2(\pi t/T_s) + \beta_p E_0 \cos^2[\pi(t - T_s/2)/(T_s + 2T_p)] & \text{for} \quad T_s/2 \le t \le T_s, \\ \beta_p E_0 \cos^2[\pi(t - T_s/2)/(T_s + 2T_p)] & \text{for} \quad T_s \le t \le T_s + T_p, \\ 0 & \text{else.} \end{cases} \tag{3.49}$$

As shown in Fig. 3.20 the corresponding field has a pedestal in the trailing part of the pulse, which depends on the parameters β_p and T_p. For $\beta_p \to 0$ and/or $T_p \to 0$, E_{env} equals the commonly used

$\sin^2$-form of the envelope with duration T_s.

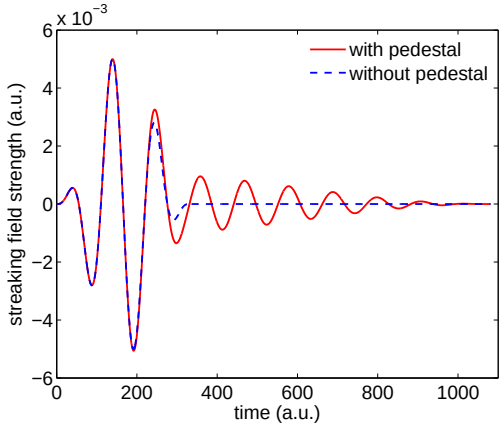

Figure 3.20: Streaking field with a pedestal (red solid line): $E_0 = 5.34 \times 10^{-3}$ (i.e., $I_s = 1 \times 10^{12}$ W/cm^2), $T_s = 331$, $\beta_p = 0.2$, and $T_p = 750$. As a comparison a basic 3-cycle 800 nm streaking pulse (blue dashed line) is also shown.

We perform quantum streaking simulations for different values of the parameters β_p and T_p for the 1D Coulomb potential $V_{\rm C}(z)$ with effective charges, $Z = 1.0$ and $Z = 3.0$ respectively, and a streaking pulse with $T_s = 331$ at a wavelength of 800 nm and a peak intensity of $I_s = 1 \times 10^{12}$ W/cm^2. To ionize the electron from the ground state of each potential, we have used an XUV pulse with $I_{\rm XUV} = 1 \times 10^{15}$ W/cm^2, $\omega_{\rm XUV} = 60$ eV ($Z = 1.0$) or 100 eV ($Z = 3.0$), $N_{\rm XUV} = 10$ ($Z = 1.0$) or 15 ($Z = 3.0$), and $\phi_{\rm XUV} = -\pi/2$. In each of these simulations we extract the time delay by applying the XUV over the interval $[0, T_s]$ of the corresponding pulse. The results are shown in Fig. 3.21 [blue solid line with circles in (a) and (c), blue solid line with squares in (b) and (d)].

We observe that the time delays obtained for the pedestals deviate from those for the $\sin^2$-pulse shape ($T_p = 0$ or $\beta_p = 0$) for both potentials. This is in agreement with our interpretation of a finite-range time delay and the dependence on the instantaneous streaking field strength during the propagation of the electron [Eq. (3.44)], since the deviation increases as β_p or T_p increases. Quantitatively, our results however further show that the deviations due to the presence of the pedestal are rather small [e.g., about 1% for $Z = 3.0$ and $\beta_p = 1.0$, see Fig. 3.21(d)]. This is due to the fact that the effect of the pedestal comes into play when the electron is at rather large distances

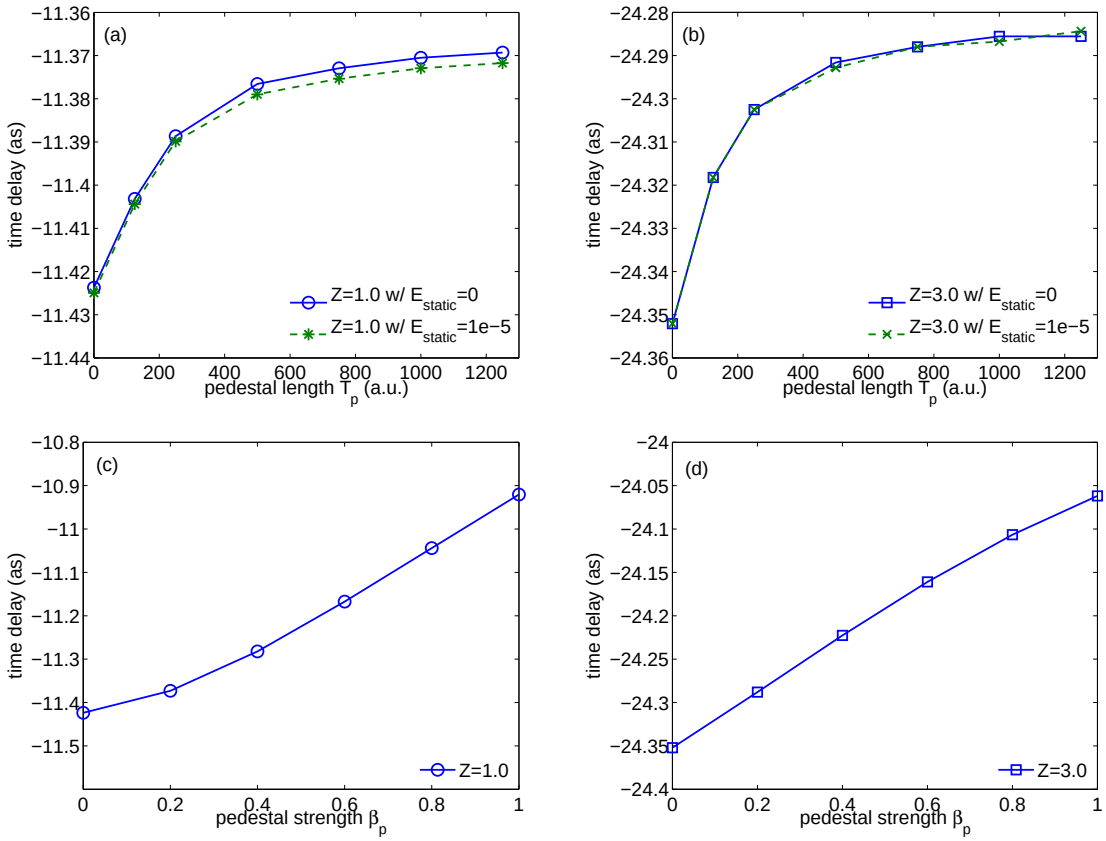

Figure 3.21: Streaking time delay as a function of (a) and (b) the pedestal length T_p ($\beta_p = 0.2$), and (c) and (d) the pedestal strength β_p ($T_p = 750$). The left column shows the results for $Z = 1.0$, while the right column is for $Z = 3.0$. The influence of an additional static field on the streaking time delay is also present (green dashed lines with asterisks and crosses) in (a) and (b).

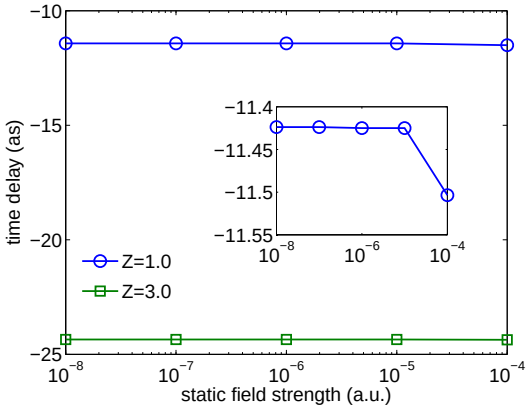

Figure 3.22: Streaking time delays as a function of the strength of the additional static field for a basic 3-cycle 800 nm streaking field for two potentials: blue solid line with circles for $Z = 1.0$ and green solid line with squares for $Z = 3.0$.

from the nucleus, at which the Coulomb potential is weak. Thus, we expect that for an atomic-like system pedestals and other deviations from a $\sin^2$ or Gaussian streaking pulse shape should not have a large effect on the observed time delays.

Finally, we also investigate the influence of additional static electric fields on the attosecond streaking time delay. In an experiment the presence of such additional fields may be used in order to direct the photoelectrons towards a detector. We therefore include an additional static field term E_{static} in Eq. (2.32) and performed quantum streaking simulations for streaking pulses with and without pedestal. As before, we consider two 1D Coulomb potentials $V_{\text{C}}(z)$ with different effective charges of $Z = 1.0$ and $Z = 3.0$ respectively. From the results presented in Fig. 3.22 we conclude that the presence of additional static electric fields up to field strengths of $E_{\text{static}} = 10^{-5}$ do not have a significant effect on the extracted time delays. The same conclusion can be also drawn for streaking pulses with a pedestal, which can be seen by comparing the green dashed lines (for $E_{\text{static}} = 10^{-5}$, stars for $Z = 1.0$ and crosses for $Z = 3.0$) with the blue solid lines (for $E_{\text{static}} = 0$, circles for $Z = 1.0$ and squares for $Z = 3.0$) in Fig. 3.21 (a) and (b).

Chapter 4

Time Delays in Two-Photon Ionization

The advances in laser technology, in particular the ability to generate more and more intense ultrashort XUV pulses, have provided us the possibilities to study high-order nonlinear processes, such as the two-photon ionization (TPI) in XUV photon energy regime. The TPI, especially its angular momentum distribution, has been extensively investigated both experimentally and theoretically recently (e.g., [87–90]). These investigations provide a lot of information about the TPI process, including the phase shifts and the dipole matrix elements for individual partial waves [88, 89]. To continue and also extend our previous work, we however want to study this process from a different perspective, namely time resolving the TPI. Similar to what has been done for single-photon ionization (SPI), we propose to use the attosecond streaking technique to study the TPI and retrieve the instant of transition into the continuum, which would be possible based on our previous understanding of the propagation time delay. This chapter is organized as follows: First, we present numerical results of streaking time delays obtained for TPI from numerical simulations of streaking scenarios. By properly accounting for the measurement induced time delay, i.e., the propagation time delay, we are able to retrieve the absorption time delay, i.e., the instant of ionization with respect to the center of the XUV pulse, for both resonant and nonresonant TPI as well as its dependence on XUV laser parameters. Next, to further support our interpretation of the absorption time delay, we use two independent studies, namely the trajectory analysis and the phase analysis, to reproduce our numerical results for the absorption time delay. Finally, we review some of our previous work on two-photon coherent control that may relate to the potential

applications of the TPI delay.

4.1 Time delays extracted in two-photon ionization using streak camera[1]

The application of the attosecond streaking technique in studying SPI process has already given us interesting time information about this process and also initiated many fruitful discussions about the origin of the time delay measured in the experiment. We therefore want to further apply this technique to some more complex ultrafast processes, such as the resonant and nonresonant TPI, in which "resonant" means that the central frequency of the XUV ionizing pulse is in resonance with the energy difference of the initial ground state and one intermediate state. We will first report our numerical results of time delays extracted in simulations of the streaking experiment, from which we identify an apparent difference of the streaking time delay dependence on the XUV pulse duration for these two types of TPI (Fig. 4.1). We then use our previously proposed classical approaches to calculate the propagation time delay, which needs to be subtracted from the streaking time delay to obtain the real photonionization instant with respect to the center of the XUV pulse. We are then finally able to show that the nonresonant TPI occurs at the center of the XUV pulse while the resonant TPI occurs with a positive delay with respect to the center and this delay changes linearly with the duration of the XUV pulse.

4.1.1 Streaking time delay

As before, we use the standard Crank-Nicolson method to numerically solve the TDSE on a grid in space and time,

$$i\frac{\partial\Psi(\boldsymbol{r},t)}{\partial t} = \left[\frac{\boldsymbol{p}^2}{2} + V(\boldsymbol{r}) + (\boldsymbol{E}_{\mathrm{XUV}}(t) + \boldsymbol{E}_s(t))\cdot\boldsymbol{r}\right]\Psi(\boldsymbol{r},t), \tag{4.1}$$

where $\boldsymbol{p}$ is the momentum operator and $\boldsymbol{E}(t) = E_0\sin^2(\pi t/T)\cos(\omega t+\phi)\hat{\boldsymbol{z}}$ for both laser fields with peak amplitude E_0, pulse duration T, central frequency ω, and carrier-envelope phase ϕ of the respective field. In all simulations we propagate the wave function on the grid for a sufficiently

[1] The results of this section are presented in J. Su, H. Ni, A. Jaroń-Becker, and A. Becker, *Time Delays in Two-Photon Ionization*, submitted.

long time until both laser pulses cease and the ionizing wave packet can be clearly separated from the bound wave function. We also confirm that the outgoing wave packets stay on the grid and do not reach its boundaries. To obtain the momentum distribution, we either project the ionizing wave packet onto the continuum eigenstates of the potential, or perform a Fourier transform. For the latter choice, we have propagated the wave packet far enough from the core part such that the error due to the planewave approximation is negligible.

We simulate the two-photon ionization process dressed by a streaking field for a helium (He) atom in the 3D Cylindrical coordinates as well as a 1D Coulomb model potential. The latter one allows us to systematically study the dependence of the measured time delays on the laser parameters. For the 3D He atom, due to its azimuthal symmetry, we are able to solve this problem in the 2D (ρ, z) coordinates. With spatial steps of $\Delta\rho = \Delta z = 0.2$ and a time step of $\Delta t = 0.02$, we obtain eigenenergies of the three lowest states as $E_{1s} = -0.90$, $E_{2s} = -0.16$, and $E_{2p} = -0.13$, using the single-active-electron model potential introduced in Ref. [71]. To ionize the electron initially bound in 1s state, we choose the central frequency of the XUV field to be $\omega_{\rm XUV} = 15.63$ and 21.07 eV, with the latter one corresponding to the energy difference between 1s and 2p states. The 1D Coulomb potential is chosen to have the form of $V(x) = -Z/\sqrt{x^2 + a}$, with $Z = 3.0$ and $a = 0.15$, which gives the energies of the three lowest states as $E_0 = -5.32$, $E_1 = -2.31$, and $E_2 = -1.30$, for $\Delta x = 0.05$ and $\Delta t = 0.01$. These three states are chosen to be well-separated such that usually only the first excited state is involved in the resonant TPI. Accordingly, we choose $\omega_{\rm XUV} = 95.62$ and 81.81 eV, corresponding to nonresonant and resonant TPI processes. Other parameters for the XUV pulse are the same for the two potentials: $I_{\rm XUV} = 1.0 \times 10^{14}$ (nonresonant) or 1.0×10^{13} W/cm^2 (resonant), and $\phi_{\rm XUV} = -\pi/2$. To streak the photoelectron in the continuum, we have used a 3-cycle 2400 nm streaking field with $I_{\rm s} = 1.0 \times 10^{11}$ W/cm^2 and $\phi_{\rm s} = -\pi/2$.

Fig. 4.2 presents our numerical results of time delays extracted from streaking traces measured in the streaking experiment [91]. In each subfigure we show the change of the streaking time delay as a function of the XUV pulse duration for resonant (green solid lines with squares) and nonresonant (blue solid lines with circles) ionization. We clearly see that the changing trends of the two processes

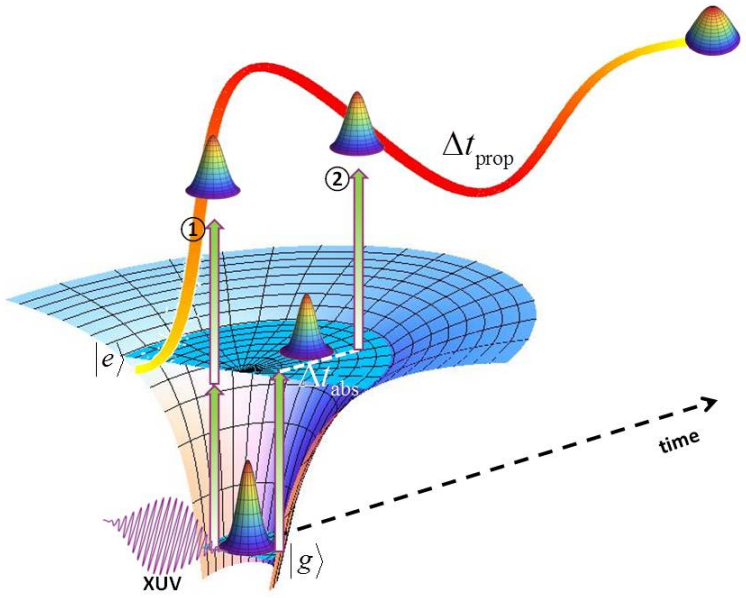

Figure 4.1: Schematic diagram for obtaining time delays in two-photon ionization (TPI) using attosecond streaking technique. An electron initially bound in the ground state $|g\rangle$ is ionized by absorbing two photons from the XUV pulse either through a resonant state $|e\rangle$ (resonant TPI) or not (nonresonant TPI), and then streaked by the long wavelength field in the continuum. By changing the relative delay between the XUV and streaking pulses, one obtains a streaking trace, from which a temporal shift (or streaking time delay Δt_s) can be extracted. After accounting for the propagation time delay Δt_{prop} that the electron accumulates in the continuum, we are able to access the absorption time delay Δt_{abs} of the TPI process.

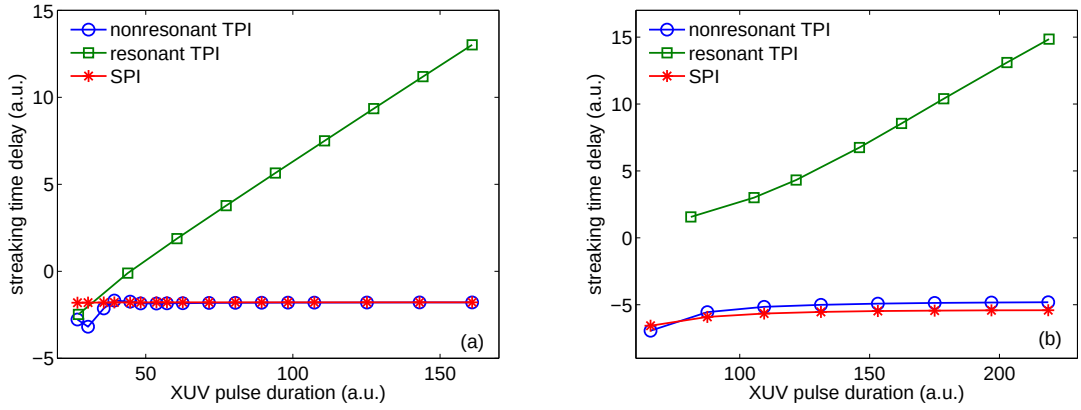

Figure 4.2: Streaking time delay as a function of XUV pulse duration for (a) 1D Coulomb and (b) 3D He potentials. Three ionization processes are considered: nonresonant TPI (blue solid lines with circles), resonant TPI (green solid lines with squares), and one-photon ionization (red solid lines with asterisks). Laser parameters are given in the text.

are different: for the resonant one the time delay increases with XUV duration, however, in the case of the nonresonant one it remains almost unchanged. Even though the streaking time delay may have some other contributions, the significant difference between the trends of the two delay curves already strongly indicates that the intermediate state plays an important role in the temporal dynamics of the TPI process. It appears that, for resonant TPI, after absorption of the first photon, the electron remains in the intermediate state for some time, before it absorbs the second photon and then transfers into the continuum. As we will show below, for long XUV pulses (e.g., $T_{\mathrm{XUV}} \geqslant 150$ for 3D He atom), the time the electron spends in the intermediate state is proportional to the XUV duration. Moreover, this difference between resonant and nonresonant TPI appears to be an universal phenomenon, since it occurs in both 3D He atom and 1D Coulomb potential.

To clearly distinguish our new observations from those in previous well-studied SPI process that also uses attosecond streaking technique, we also show the dependence of the streaking time delay (red solid lines with asterisks) on the XUV duration for SPI that is induced by a 2-ω_{XUV} (nonresonant frequency) XUV pulse. The intensity of the XUV pulse is set to be $I_{\mathrm{XUV}} = 1.0 \times 10^{14}$ W/cm^2 for 1D Coulomb, and $I_{\mathrm{XUV}} = 1.0 \times 10^{12}$ W/cm^2 for 3D He, both of which guarantee that the photoionization process occurs in the perturbative intensity regime. Similar to the nonresonant TPI process, the SPI time delay remains almost unchanged as the XUV pulse duration increases. More interestingly, for the 1D Coulomb potential [Fig. 4.2(a)] the streaking time delay of SPI is exactly the same as that of the nonresonant TPI when the duration of the XUV pulse is long enough (e.g., $T_{\mathrm{XUV}} \geqslant 50$). This implies that the two-photon absorption occurs instantaneously as the one-photon absorption, which occurs most likely at the center of the XUV pulse as it has been shown in Chapter 3. However, in the 3D case [Fig. 4.2(b)], these two time delays are very similar but not exactly equivalent. This may relate to the fact that the photoelectrons have different angular momenta in the continuum (p wave for SPI, and a mixture of s and d waves for TPI). It is well-known that different final states in the continuum result in different streaking time delays (e.g., [37, 58]).

4.1.2 Propagation time delay

It has been well-studied that the propagation of the photoelectron in the combined field of the streaking pulse and the atomic potential can induce an extra shift in its final momentum, which results in an temporal shift (or time delay) in the obtained streaking trace (e.g., [37, 38, 81]). Indeed, one needs to account for this propagation time delay in order to obtain the instant of photoemission as the instant at which the electron is set free in the continuum after the photon absorption. Therefore, to extract a real time delay of a photoabsorption process from a streaking experiment, it is necessary to properly account for the propagation time delay, which is actually a measurement-induced delay. As discussed before [37, 81, 85, 92] for the SPI process, this propagation time delay can be often well-reproduced by classical trajectory calculations. Here we can use the same idea to obtain the propagation time delays for TPI, because once the electron is in the continuum it does not matter if it is ionized via a one- or two-photon process. For our 1D Coulomb case, we use the classical method introduced in Ref. [81], in which we assume the electron is initially at $x = 0$ and simulate its propagation in the combined Coulomb-streaking field by solving 1D Newton's equation directly. By fitting the classical streaking trace to the original streaking formula, we obtain the propagation time delays, which are shown as green solid lines with squares in Fig. 4.3(a) and (c). For the 3D He atom case, we use the classical-trajectory Monte Carlo method introduced in Ref. [37] in order to take into account both the distribution of the initial position of the electron in the bound state and the final shape of the ionized wave packets in the continuum. To be clear, we have sampled the initial position of the electron from the probability distribution of the initial eigenstate, and chosen the distribution of the initial momentum according to the angular shape of the wave packet (either s or d wave). The propagation time delays from different waves are added up coherently and are also shown as green solid lines with squares in Fig. 4.3(b) and (d). One may note that, for both 1D and 3D models, the propagation time delays have very weak dependence on the XUV duration, which is expected, since the final electron energy that determines the propagation time delay barely changes with the XUV duration.

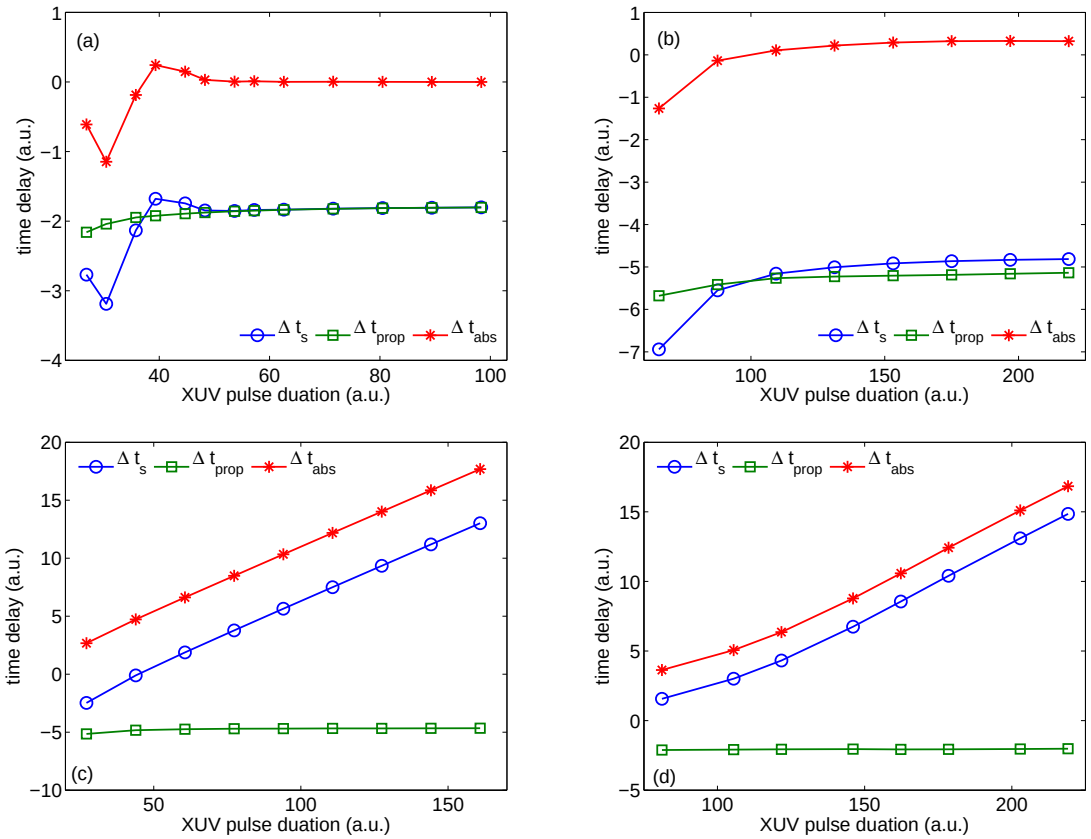

Figure 4.3: Absorption time delay (red solid lines with asterisks) as a function of XUV pulse duration for nonresonant TPI in 1D Coulomb [(a)] and 3D He [(b)] potentials, and resonant TPI in 1D Coulomb [(c)] and 3D He [(d)] potentials. Also shown are the streaking time delays (blue solid lines with circles) and the propagation time delays (green solid lines with squares).

Table 4.1: Time delays for different parameters of the streaking field. We consider resonant TPI in the 1D Coulomb potential streaked by a 3-cycle laser pulse. XUV laser parameters are: $\omega_{\mathrm{XUV}} = 81.81$ eV, $N_{\mathrm{XUV}} = 45$, $I_{\mathrm{XUV}} = 1.0 \times 10^{13}$ W/cm^2, and $\phi_{\mathrm{XUV}} = -\pi/2$.

λ_s(nm)	I_s(W/cm^2)	Δt_s(a.u.)	Δt_{abs}(a.u.)
2400	1.0×10^{11}	5.65	10.34
3200	1.0×10^{11}	5.15	10.34
4800	1.0×10^{11}	4.41	10.33
4800	1.0×10^{10}	4.45	10.36

4.1.3 Absorption time delay

Now we are able to retrieve the absorption time delay (red solid lines with asterisks in Fig. 4.3), a real time delay in the photoabsorption process, after properly accounting for the propagation time delay. For long XUV pulses used in the nonresonant TPI, one sees that the absorption time delay is exactly zero for the 1D simulations and relatively close to zero for the 3D simulations. This is consistant with our previous finding that the nonresonant TPI occurs instantaneously as SPI, which means both processes occur at the center of the XUV, i.e., without time delays. In contrast, the electron appears to take a nonzero time to absorb two photons before it is set free to the continuum in resonant TPI. Moreover, the photon absorption time changes linearly with the XUV duration once the pulse is long enough. One may explain this difference by understanding the TPI process in three very simple steps: First, the electron in the ground state is excited to the excited state by absorbing one photon from the XUV field. Then it spends some time staying in the excited state. Finally, it absorbs another photon and is set free to the continuum. Since there is no intermediate state for the electron to stay for nonresonant TPI, it has to absorb two photons simultaneously, which thus makes no difference to the case of SPI. Here we have to point out that using the attosecond streaking technique we only have the time information when the electron is set free in the continuum, i.e., the instant when the second photon is absorbed. The time information about the absorption of the first photon is not available based on the present technique even for the nonresonant TPI.

In order to further support our interpretation, it is of our interest to confirm that the ab-

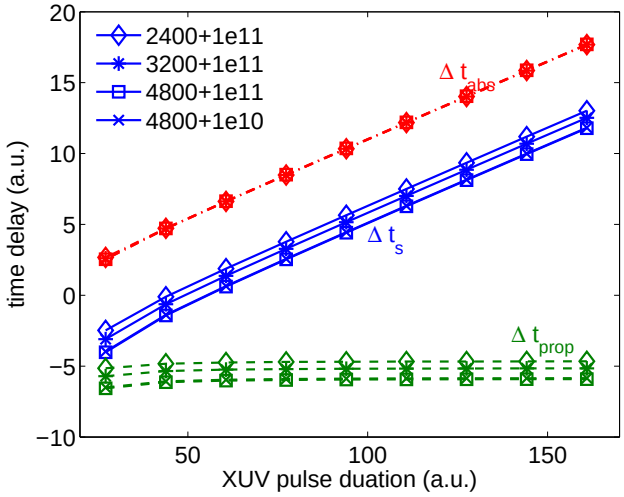

Figure 4.4: Absorption time delay (red dash-dotted lines) as a function of XUV pulse duration for resonant TPI in 1D Coulomb potential for different streaking parameters (diamonds: $\lambda_s = 2400$ nm and $I_s = 1.0 \times 10^{12}$ W/cm^2, asterisks: $\lambda_s = 3200$ nm and $I_s = 1.0 \times 10^{12}$ W/cm^2, squares: $\lambda_s = 4800$ nm and $I_s = 1.0 \times 10^{12}$ W/cm^2, and crosses: $\lambda_s = 4800$ nm and $I_s = 1.0 \times 10^{11}$ W/cm^2). Also shown are the streaking time delays (blue solid lines) and the propagation time delays (green dashed lines).

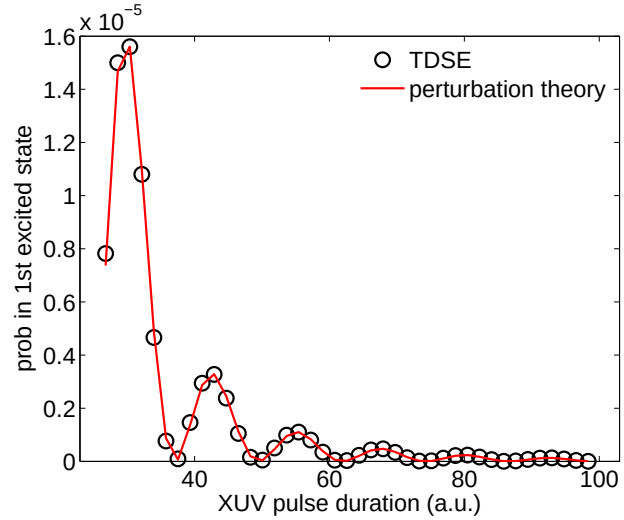

Figure 4.5: Excitation probability as a function of the duration of the XUV pulse for the nonresonant TPI in the 1D Coulomb potential. We have used two methods to calculate the excitation probability in the first excited state: the numerical solution of TDSE (black open circles) and the perturbation theory (red solid line).

sorption time delay we obtained for the TPI process are independent of the measurement, i.e., remains unchanged as the streaking pulse parameters change. In Fig. 4.4, as expected, we see that the absorption time delays (red dashed lines) are identically for different streaking parameters, although the streaking time delays measured directly from the experiment as well as the propagation time delays are quite different in particular when the wavelength of the streaking field changes. This again implies that correctly accounting for the propagation time delay is crucial for obtaining a solid absorption time delay. To clearly show this measurement independence numerically, we further present values of the absorption time delays in Table 4.1 for $N_{\mathrm{XUV}} = 45$ ($T_{\mathrm{XUV}} = 94.05$), from which one sees that the deviation is within 1 as, i.e., a relative difference of 0.3%.

Before we further analyze our results, we want to explain some subtle details in our results, such as the small oscillation in Fig. 4.3(a) and the nonlinear behavior in Fig. 4.3(d) when the duration of the XUV pulse is small. These behaviors can be related to excitations to the excited states. When the XUV pulse is short in time domain, it has a broad bandwidth in frequency domain, which means certain excited states within the energy bandwidth can be involved in the nonresonant TPI. Thus, the nonresonant TPI has a significant resonant contribution as in Fig. 4.3(a) or more than one excited state is involved in the resonant TPI. Each of these may result in a deviation from the expected dependence of the absorption time delay on the XUV pulse duration. As an example, a significant excitation probability in the first excited state of the 1D Coulomb potential is observed when the XUV pulse is short as shown in Fig. 4.5(a), where we have used results from both the TDSE solution and the perturbation theory. We further note that the oscillations in this figure are due to the oscillating structure of the frequency spectrum of the $\sin^2$ XUV field.

4.2 Alternative studies of absorption time delays in two-photon ionization

In the last section, we have shown how one can extract the absorption time delay of the TPI process using the attosecond streak camera and have also studied its dependence on the duration of the XUV pulse. In particular, the linear dependence of the absorption time delay on the XUV pulse duration for the resonant TPI appears to be very useful in potential control applications due

to this simple linear relation. In order to further confirm our new findings and also provide some more understanding of these new results, we make use of two different methods in this section, namely the trajectory analysis and the phase derivative analysis, both of which have already been introduced in the study of the SPI process in section 3.1.3.

4.2.1 Trajectory analysis

It has been shown that the trajectory of the photoelectron in the continuum contains useful time information about the photoabsorption process (e.g., [43, 44, 46, 52]). As introduced before, a typical way to obtain the WS time delay for the SPI process from the trajectory is to extrapolate the linear part of the trajectory back to the time axis, where the trajectory can be obtained by solving the TDSE numerically. The interception of this extrapolated line with the time axis is the desired time delay. However, as emphasized before, this approach only works for ionization from a short-range potential, while for a long-range potential such as the Coulomb potential the nonlinear component in the trajectory makes it impossible to fit the trajectory to a linear line even for the part that is far away from the origin.

For the systems considered in our TPI analysis, e.g., the 1D Coulomb potential, it therefore appears on the first view impossible to make use of the trajectory analysis to obtain the time delay because of the long-range property of the Coulomb potential. However, by noting the fact that each TPI trajectory has a corresponding SPI trajectory that has the same long-range behavior if they have the same final energy, we can obtain the time delay of the TPI trajectory with respect to the SPI trajectory by treating the latter one as a reference instead of the free particle trajectory. Then, the previously mentioned divergence problem of the WS time delay for the Coulomb potential does not occur since the divergent contributions of the two trajectories cancel out. A similar idea has been used to understand the physical meaning of the energy derivative of the Coulomb phase shift in Ref. [93], where the quantum and classical scattering trajectories are compared.

To illustrate this idea, we consider the TPI and SPI processes in the 1D Coulomb potential with $Z = 3.0$ and $a = 0.15$, the same that we used in the last section. As usual the TDSE that

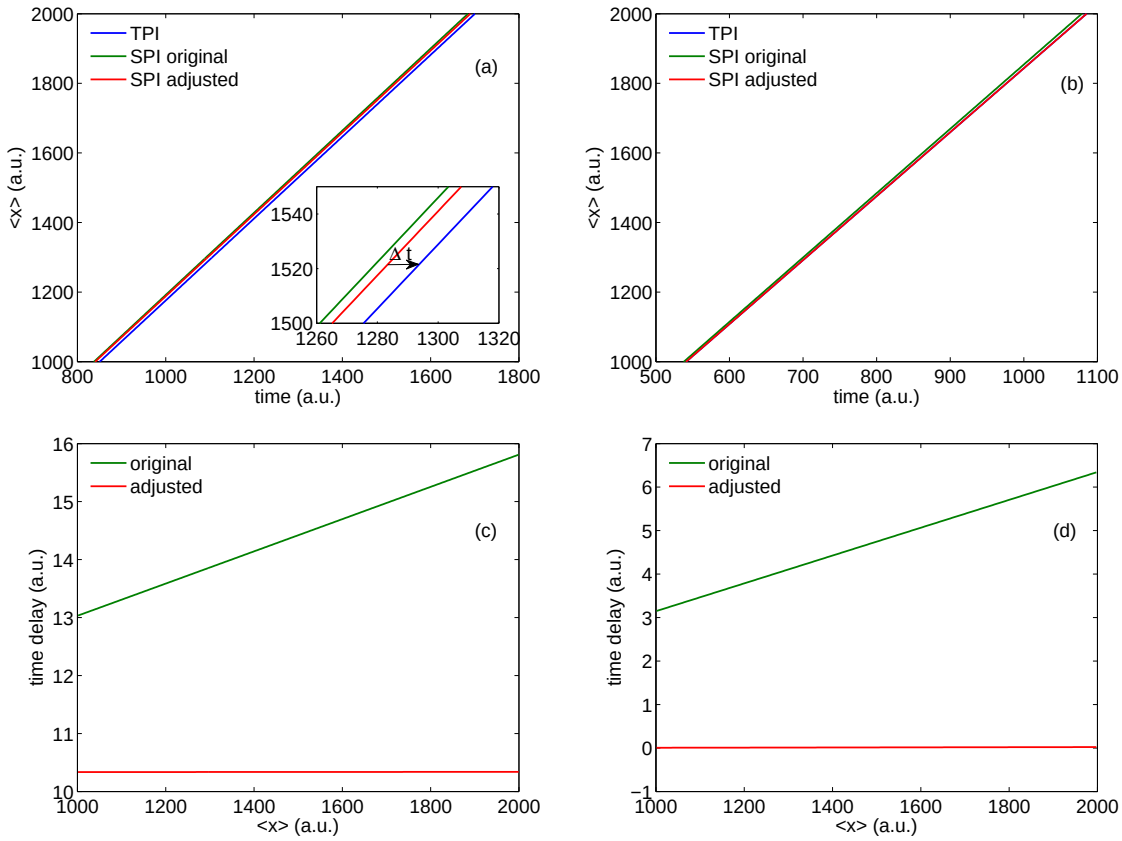

Figure 4.6: Trajectory analysis of time delays in TPI. We have shown the trajectories of the photoelectron for three processes [(a) and (b), blue lines for TPI, green lines for original SPI, and red lines for adjusted SPI] and the time delay as a function of the position of the photoelectron [(c) and (d), green lines for original SPI, red lines for adjusted SPI]. The trajectory is calculated using the expectation value $\langle x \rangle$ of the electron position as a function of time by solving TDSE. The time delay is obtained as the time difference for the same $\langle x \rangle$ between the TPI and SPI trajectories. We have considered both resonant (left column) and nonresonant (right column) TPI. Here the original SPI means the SPI process initiated by an XUV pulse with $\omega_{\mathrm{SPI}} = 2\omega_{\mathrm{TPI}}$ while the adjusted SPI stands for using an XUV pulse with $\omega_{\mathrm{SPI}} = 2\omega_{\mathrm{TPI}} + \Delta\omega$, which makes the final energy of the SPI wave packet exactly the same as that of the TPI wave packet. The inset in (a) shows how we obtain the time delay between the TPI and SPI trajectories.

describes the interaction of the electron with the XUV pulse in length gauge is numerically solved on a space-time grid. When the XUV pulse ceases and the ionizing wave packet can be clearly separated from the bound wave function, we are able to obtain the trajectory of the photoelectron, i.e., the expectation value $\langle x \rangle$ of the position of the ionizing wave packet as a function of time. In order to generate the corresponding SPI trajectory for a TPI process, we use an XUV pulse with a doubled central frequency to ionize the electron from the ground state, i.e., $\omega_{\mathrm{SPI}} = 2\omega_{\mathrm{TPI}}$. We choose the pulse duration of the XUV pulses for TPI and SPI to be equal, which yields $N_{\mathrm{SPI}} = 2N_{\mathrm{TPI}}$, and the intensities of the XUV pulses are the same as given in the last section for the individual cases. Once we have obtained the trajectories, the time delay between the TPI and SPI processes is given by the time difference between the two trajectories for the same electron position $\langle x \rangle$.

The trajectories of the TPI (blue lines) and SPI (green lines) are presented in the upper panel of Fig. 4.6 for (a) for the nonresonant TPI with $N_{\mathrm{TPI}} = 45$ ($T_{\mathrm{TPI}} = 94.05$) and (b) the resonant TPI with $N_{\mathrm{TPI}} = 50$ ($T_{\mathrm{TPI}} = 89.40$). Since the time delay is small (a few a.u.) as compared to the time scale (a few thousands a.u.) on the horizontal axis, we use a small inset in (a) to show the definition of the time delay between TPI and SPI. To analyze this time delay, we show the time delay (green lines) as a function of electron position $\langle x \rangle$ in the lower panel of Fig. 4.6 with (c) and (d) for the resonant and nonresonant TPI, respectively. The time delay does not remain constant as $\langle x \rangle$ changes, which means that measuring the time delay at different positions of the electron gives with different results. Of course, such a time delay is not well-defined and hence cannot be useful to support our previous results obtained in streaking scenarios. However, the linear change of the time delay with $\langle x \rangle$ is caused by the fact that the final energies of the TPI and SPI are not exactly equivalent for finite duration XUV pulses by choosing $\omega_{\mathrm{SPI}} = 2\omega_{\mathrm{TPI}}$. Indeed, the relation for the expectation value of the final energy of the photoelectron $\langle E_f \rangle = N\omega_{\mathrm{XUV}} - I_p$, is strictly valid only in the limit of an infinite long pulse, for which its energy spectrum is a delta function. For a typical attosecond XUV pulse this relation is only an approximation, which may sometimes cause on the attosecond time scale large errors, e.g., for the present time delay study.

To clearly show the impact of this error on the time delay, let us recall the analytical formula

for the ionizing wave function of the photoelectron in a Coulomb potential (e.g., [92, 93]), which for the present 1D Coulomb potential is

$$\Psi(x,t) \propto \exp\left[ikx - i\frac{k^2}{2}t + i\frac{Z\ln(2kx)}{k} + i\varphi_c(k) + i\varphi_{\rm abs}(k)\right] \tag{4.2}$$

where k is the momentum of the electron, φ_c is the 1D Coulomb scattering phase shift, and $\varphi_{\rm abs}$ is the phase acquired by the electron in the photoabsorption process that is in general not present for a common scattering process. Using the stationary phase approximation, similar to our trajectory analysis for SPI, we obtain the trajectory for the photoelectron in a photonionization process as

$$t(x) = \frac{x}{k_0} - \frac{Z\ln(2k_0x)}{k_0^3} + \left.\frac{d\varphi_c}{dE}\right|_{E_0} + \left.\frac{d\varphi_{\rm abs}}{dE}\right|_{E_0}, \tag{4.3}$$

where k_0 is the expectation value of the final asymptotic momentum of the photoelectron and $E_0 = k_0^2/2$. Here the second term is a logarithmic term that changes slowly with x, which is however responsible for the divergence property of the WS time delay for the long-range Coulomb potential. As compared with the corresponding free-particle trajectory, the sum of the second and third terms gives the time delay the photoelectron accumulates during its propagation in the continuum after the photoabsorption, while the last term is the time delay acquired by the electron in the photoabsorption process. We want to emphasize that Eq. (4.3) is general for both SPI and TPI with the only difference is that the absorption time delay, i.e., the last term, is zero for SPI.

Considering the time delay between the TPI and SPI trajectories, we get

$$\Delta t = \left[\frac{x}{k_0^{\rm TPI}} - \frac{Z\ln(2k_0^{\rm TPI}x)}{(k_0^{\rm TPI})^3} + \left.\frac{d\varphi_c}{dE}\right|_{E_0^{\rm TPI}} + \left.\frac{d\varphi_{\rm abs}}{dE}\right|_{E_0^{\rm TPI}}\right] - \left[\frac{x}{k_0^{\rm SPI}} - \frac{Z\ln(2k_0^{\rm SPI}x)}{(k_0^{\rm SPI})^3} + \left.\frac{d\varphi_c}{dE}\right|_{E_0^{\rm SPI}}\right], \tag{4.4}$$

where we have dropped the absorption time delay term for SPI since it is zero. By assuming that $k_0^{\rm SPI} = k_0^{\rm TPI} + \Delta k = k_0 + \Delta k$ and Δk is sufficiently small, we can further simplify Eq. (4.4) as

$$\Delta t \simeq \frac{\Delta k}{k_0^2}x - \frac{3\Delta k}{k_0^4}Z\ln(2k_0x) + \left.\frac{d\varphi_{\rm abs}}{dE}\right|_{E_0}, \tag{4.5}$$

which contains a linear term in x that is responsible for the linear trend of the green lines in Fig. 4.6(c) and (d). In this simplification step we have also assumed that the third terms in each

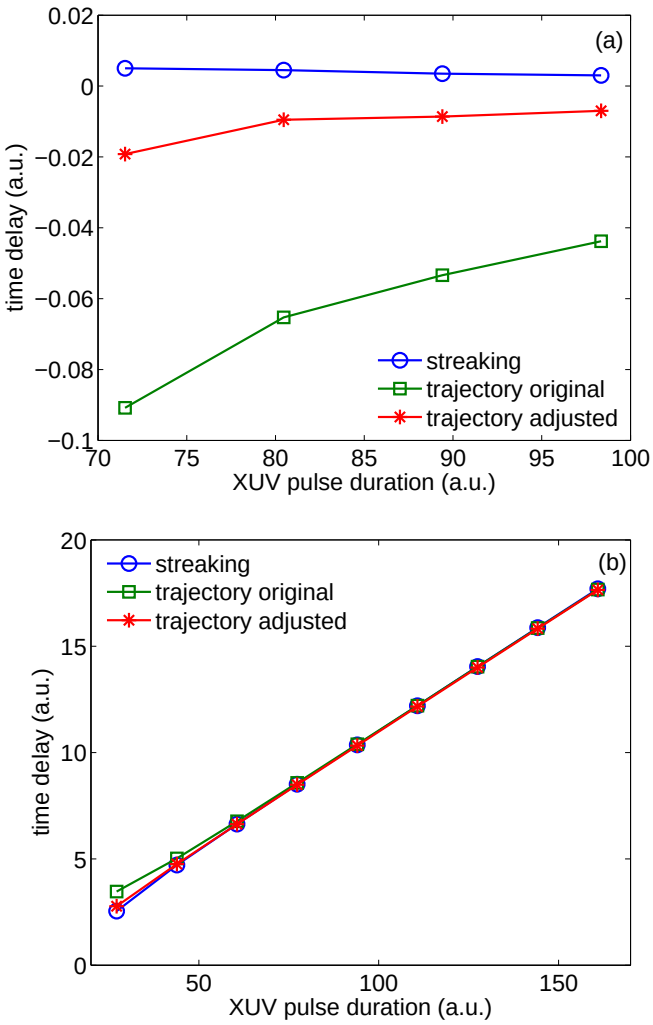

Figure 4.7: Time delay obtained from trajectory analysis as a function of XUV pulse duration. We have used two ways of calculating the time delays from the trajectories: one relies on fitting the original time delay curve [e.g., green lines in Fig. 4.6(c) and (d)] to Eq. (4.5) (green lines with squares), the other one relates the time delay to the constant delay line [e.g., red lines in Fig. 4.6(c) and (d)] (red lines with asterisks). Results for both nonresonant [(a)] and resonant [(b)] TPI are shown. Also shown are the absorption time delays (blue lines with open circles) of TPI extracted from streaking scenarios.

trajectory, i.e., the energy derivative of the scattering phase shift, cancel out. While such an assumption is valid for the 1D Coulomb potential, one needs to take special care for the more general 3D case because different ionization processes will generally result in different final angular momenta (p wave for SPI, s and d waves for TPI) and thus in different scattering phase shifts even though their final momenta are close. In the limit of $\Delta k \to 0$, Eq. (4.5) reveals that the time delay between the TPI and SPI processes is given by

$$\Delta t = \left. \frac{d\varphi_{\rm abs}}{dE} \right|_{E_0} . \tag{4.6}$$

Now, it is apparent that there are two ways to obtain the time delay between TPI and SPI from the trajectory calculation: One is to extract the last constant term in Eq. (4.5) by fitting the time delay curves [green lines in Fig. 4.6(c) and (d)] to Eq. (4.5). The other one is to satisfy the condition of $\Delta k = 0$ by changing the frequency $\omega_{\rm SPI}$ of the SPI XUV pulse. Then the time delay is directly available from the constant time delay curve [red lines in Fig. 4.6(c) and (d)]. In Fig. 4.7 we show results for the time delay obtained using these two methods for different XUV pulse durations. As expected, results from these two methods are in very good agreement for both resonant and nonresonant TPI processes. More importantly, we find that both results also agree well with the absorption time delays (blue lines with circles in Fig. 4.7) extracted from streaking scenarios for TPI. This agreement is not surprising since our present time delay and the previous extracted absorption time delay have the same reference point, namely the SPI process, which occurs at the center of the XUV pulse that is the reference point of the absorption time delay. The trajectory analysis presented here is a completely independent study of the time delay even without the presence of the streaking field and therefore is another strong support of our new findings.

4.2.2 Phase derivative analysis

As widely discussed (e.g., [40, 41]), the time delay in a process can often be related to the energy derivative of the phase that the particle acquires during this process (also see our trajectory analysis in the last subsection). We therefore like to make use of this idea to seek

another independent way to confirm and understand our new findings. Based on second-order time-dependent perturbation theory, the complex amplitude c_f of the ionizing wave packet in the continuum state $|f\rangle$ ionized from initial state $|i\rangle$ after the XUV pulse ceases can be written as [89],

$$c_f = \sum_m \mu_{fm}\mu_{mi} \int_0^T e^{i\Delta_{fm}t} E(t) \left(\int_0^t e^{i\Delta_{mi}t'} E(t')dt' \right) dt, \tag{4.7}$$

where T is the duration of XUV pulse $E(t)$, μ_{jk} and $\Delta_{jk} = E_j - E_k$ are the dipole transition matrix element and the energy difference between states $|j\rangle$ and $|k\rangle$, respectively. For nonresonant TPI, if all resonant states are out of the XUV bandwidth, Eq. (4.7) can be further simplified as [94, 95],

$$c_f \propto a_f = \int_0^T e^{i\Delta_{fi}t} E^2(t)dt, \tag{4.8}$$

where we have dropped the dipole matrix element since its phase is related to the scattering (or propagation) of the electron in the continuum, which is not of our interest. For resonant TPI, we can further rewrite Eq. (4.7) as,

$$c_f \propto a_f = \int_0^T e^{i\Delta_{fr}t} E(t) \left(\int_0^t e^{i\Delta_{ri}t'} E(t')dt' \right) dt, \tag{4.9}$$

by assuming only state $|r\rangle$ is within the field bandwidth. Now it is clear that the absorption time delay can be related to the phase of the complex amplitude as (e.g., [38, 44]),

$$\Delta t_{\text{abs}} = \frac{d}{dE}[\arg(a_f)] - \frac{T}{2}, \tag{4.10}$$

where we need to substract $T/2$ because our pulse starts from 0 instead of $-T/2$.

For a $\sin^2$ XUV profile considered in our simulations, Eq. (4.10) can be evaluated numerically. As illustrated in Fig. 4.8, the agreement between absorption time delays extracted from streaking measurement and those based on the phase analysis is acceptable. In particular, in the case of nonresonant TPI, these two sets of time delays are exactly identical (all equal zero) for a long XUV pulse [e.g., $T \geqslant 60$ in Fig. 4.8(a)]. Furthermore, the perturbation theory also well predicts the linear dependence of the time delay on the XUV duration for the resonant case [see Fig. 4.8(b)]. These successes confirm our expectation that the absorption time delay is directly related to the energy derivative of the phase that the electron acquires during the photon absorption process.

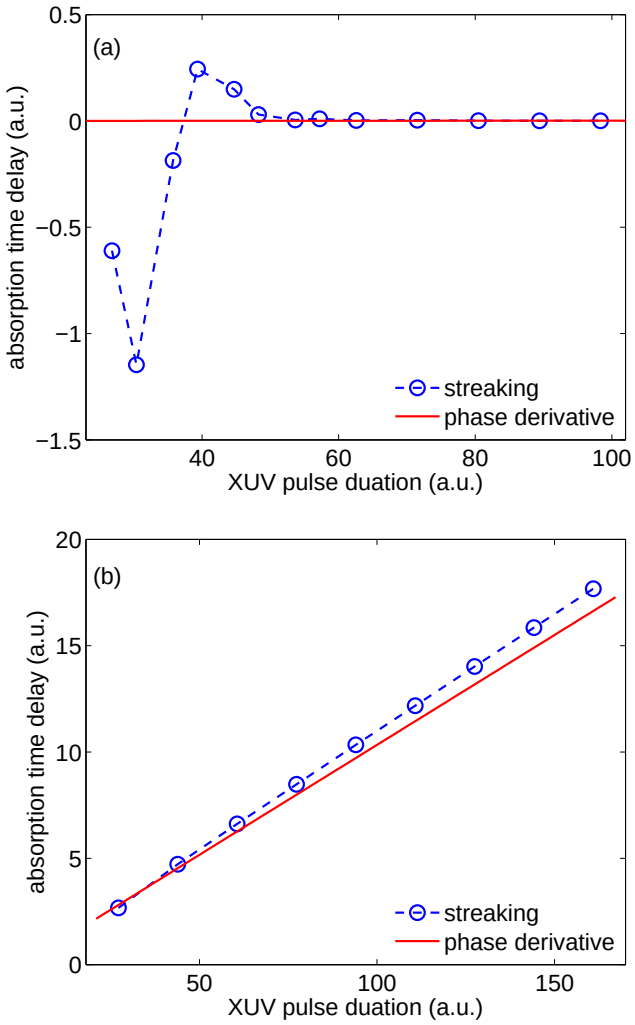

Figure 4.8: Comparison of absorption time delays from different methods: numerical streaking experiment (blue dashed lines with circles) and phase analysis (red solid lines). As before, both nonresonant [(a)] and resonant [(b)] TPI processes are studied.

And, indeed, this phase information is accessible using the attosecond streaking technique once the propagation effect is correctly accounted for. More interestingly, for resonant TPI, the linear dependence of the time delay on the XUV duration actually opens the possibility to use the duration of the ionizing pulse to control the emission time of the photoelectron, which may significantly influence the dynamics of the subsequent processes in a chemical reaction.

4.3 Control of two-photon processes[2]

In the last two sections, we have studied the TPI process in atoms and reported and analyzed new findings about the time delay in such a process. These findings, in particular the linear dependence of the absorption time delay on the XUV pulse duration, provide a new way of controlling electron dynamics in physical and chemical interactions. Similar to this idea, at the beginning of my Ph.D. studies, we have also done some work about coherent control of nonresonant two-photon excitation (TPE) to bound and dissociative states in molecules [96]. Hence in this section we like to briefly review the results of this project. The basic idea of this coherent control work is to utilize a train of laser pulses that is phase modulated in its spectrum using the pulse shaping technique to either enhance, or weaken, or even eliminate transitions between certain states in a molecule. We want to emphasize that this work may not directly relate to the previous time delay work, however, it may give us some intuitive ideas and inspirations about the application of the new findings in TPI. The section is organized as follows: First we like to give a brief introduction to coherent control by introducing some recent work in this area. We then turn to our work by discussing the theoretical models used for describing dissociative and bound states of a molecule in the second subsection. Finally, as the major part of this work, the control of excitations to dissociative and bound states in the model potentials are investigated with the help of numerical simulations.

[2] The results of this section are presented in J. Su, S. H. Chen, A. Jaroń-Becker, and A. Becker, Phys. Rev. A **84**, 065402 (2011).

4.3.1 Short introduction to coherent control

Initial ideas of quantum coherent control were based on quantum path interferences using phase-controlled laser fields [97] and pump-dump (pump-probe) schemes using sequences of laser pulses with tunable delays [98, 99]. At first glance the former technique makes use of coherence properties of light fields in the frequency domain while the latter takes advantage of the temporal evolution of a process. However, converting the respective analysis from one domain to the other often adds a complementary view on a particular control scheme [100]. Recent development of femtosecond pulse shaping techniques extends the variety of schemes in quantum coherent control (for a review, see [101]). Since pulse shaping is usually achieved by manipulating amplitude, phase, and polarization of the frequency spectrum of a laser pulse, applications to coherent control of transitions in atoms and molecules is often analyzed in the frequency domain based on the multi-pathway interference concept. For example, destructive and constructive interference among various pathways can tune few-photon absorption probabilities to zero or maximum by modification of the spectral phase of the pulse (e.g., [94, 102–105]). In particular, the experiment in Ref. [94] has demonstrated a way to control the nonresonant TPE probability between two states in a caesium atom with a femtosecond pulse train that is tailored using the pulse shaping technique.

Theoretically, Chen *et al.* [106] recently investigated some of these control schemes based on spectral phase modulations from the complementary time-dependent perspective via numerical solutions of the TDSE of an atom. The analysis shows that TPE probabilities in an (hydrogen) atom are controlled via destructive or constructive interferences between the amplitudes induced by consecutive subpulses in a pulse train. The results also provide insights into the control of atomic (2+1)-photon ionization processes. Here, we like to supplement these previous theoretical studies by the time-dependent analysis of the control of different types of two-photon transitions in molecules. In particular, we consider two different types of nonresonant excitations, namely bound-to-bound state and bound-to-dissociative state transitions.

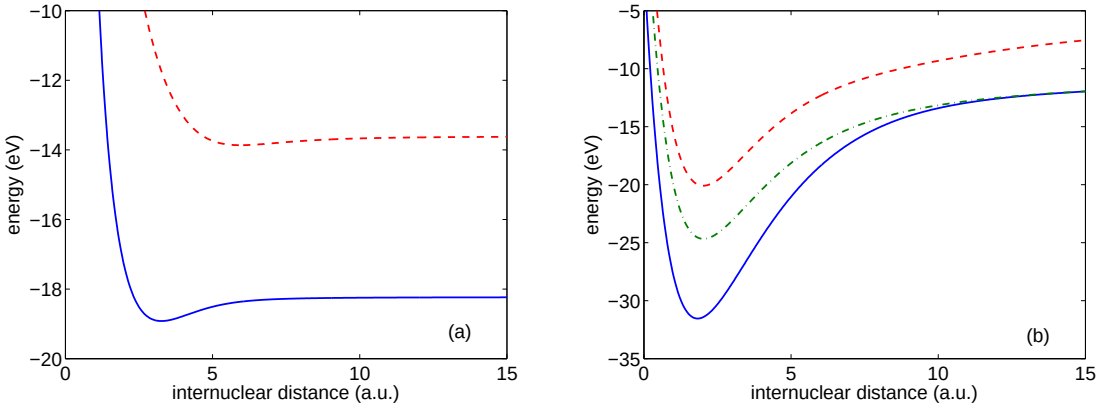

Figure 4.9: Potential energy curves of the ground and lowest lying excited states of our 2D molecular model systems: (a) model with a dissociative excited state [Eq. (4.11)] and (b) model with bound excited states [Eq. (4.12)]. We are interested in controlling excitations between states of the blue and red curves.

4.3.2 Theoretical models

To study the control of excitations in molecules, we make use of two models describing the interaction of a SAE diatomic molecule with an external field. It is well known that the first excited state ($2p\sigma_u$) of the H_2^+ molecule is a dissociative state. The following 2D model, which accounts for the coupled electronic and nuclear dynamics, in a SAE diatomic molecule has been frequently applied in simulations of H_2^+ interacting with a laser field. The field-free Hamiltonian is given by

$$H_1(R,z) = \frac{p_R^2}{2M} + \frac{p_z^2}{2m} - \frac{1}{\sqrt{(z+R/2)^2+a_1}} - \frac{1}{\sqrt{(z-R/2)^2+a_2}} + \frac{1}{\sqrt{R^2+b}}, \tag{4.11}$$

where M and m are the reduced masses of the nuclei and the electron, respectively. R is the internuclear distance, z is the electron position with respect to the center of mass of the nuclei, and a_1, a_2 as well as b are soft-core Coulomb parameters. In the case of H_2^+ one chooses $a_1 = a_2$. However, the symmetry of the corresponding Hamiltonian prohibits a two-photon transition from the electronic ground state to the first dissociative state.

For our goal to study the coherent control of TPE processes, one could instead consider transitions to the second dissociative state. But, in view of the steep decline of the potential energy curve of the first excited state as a function of the internuclear distance, (dominant) one-photon

transitions to the first excited state cannot be neglected for an ultrashort laser pulse having a broad bandwidth. As an alternative, we choose to study a molecular model system with $a_1 \neq a_2$ to break the symmetry of the Hamiltonian. In our studies, we arbitrarily choose $a_1 = 1.0$, $a_2 = 2.0$, and $b = 0.03$. The adiabatic potential energy curves for the ground and first excited state of this system, calculated using ITP of the corresponding TDSE, are shown in Fig. 4.9(a). The equilibrium distance of the two protons is $R_0 = 3.36$, and the energy gap between the states at R_0 is $\Delta E = 6.88$ eV. The curve of the first excited state has a shallow well, which however does not influence the dissociative character of the state for wave packets pumped from the initial ground state close to the equilibrium distance.

To study transitions between bound states, we use a molecular model system, in which the Coulomb repulsion $1/R$ is replaced by a Morse potential in the Hamiltonian, i.e.,

$$H_2(R,z) = \frac{p_R^2}{2M} + \frac{p_z^2}{2m} - \frac{1}{\sqrt{(z+R/2)^2+a_1}} - \frac{1}{\sqrt{(z-R/2)^2+a_2}} + D\left[1 - e^{-\lambda(R-R_0)}\right]^2 - D, \quad (4.12)$$

where D is the depth of the well, R_0 is the equilibrium distance, $\lambda = \sqrt{k/2D}$ with k is the bond force constant, and all the other parameters are the same defined as before. Using $a_1 = a_2 = 4.0$, $D = 0.4$, $\lambda = 0.5$, and $R_0 = 2.0$, the potential energy curves of the ground and first two excited states, shown in Fig. 4.9(b), are well separated. We consider nonresonant two-photon transitions to the second excited state, which is possible in the present model since the energy difference between the ground and the first excited states clearly exceeds the corresponding photon energy required for the two-photon transition.

To investigate the time evolution of the TPE process, we consider the corresponding TDSE of the molecular model systems interacting with a laser pulse linearly polarized along the internuclear axis ($j = 1, 2$),

$$i\frac{\partial}{\partial t}\Psi(R,z;t) = \left[H_j(R,z) + E(t)z\right]\Psi(R,z;t), \quad (4.13)$$

which is solved with $\Delta R = 0.03$, $\Delta z = 0.2$, and $\Delta t = 0.01$ using our common grid method. The population in the ground and excited bound states are obtained by projection on the respective field-free states, which for the laser parameters used in the present study is a reasonable approximation

even during the interaction with the external field. In the case of the excited dissociative state the population is calculated as $P_{\rm exc} = 1 - \sum_{\nu=0}^{n} P_\nu$, where ν denotes the vibrational mode in the electronic ground state and n is the total number of the vibrational states considered. The ionization and dissociation probabilities are calculated as the outgoing probability flux at the respective boundaries of the grid. At the edges we use $\cos^{1/6}$ mask functions to suppress reflections. We have checked that the results are not influenced by remaining small inaccuracies due to the boundary conditions. We use a grid of $N_R \times N_z = 600 \times 200$ points ($N_R \times N_z = 400 \times 600$ points) for the dissociative (bound) state model.

4.3.3 Control of excitation to dissociative state

First, we investigate control of TPE from a bound to a dissociative molecular state. To this end, we consider the dissociative state model and a spectral phase modulated laser field of the form

$$E\left(\frac{\omega}{2}+\Omega\right) = E_0 \mathrm{sech}\left(\frac{1.76\Omega}{\Delta\omega}\right) \exp\left[i\alpha\cos(\beta\Omega+\phi)\right]. \tag{4.14}$$

Such fields have been used recently by Silberberg and coworkers [94] to study the control of two-photon transitions in atoms. For our numerical simulations we choose the central frequency $\omega/2 = 3.44$ eV (half of the energy gap of the desired transition), the bandwidth $\Delta\omega = 0.2$ eV, the modulation depth $\alpha = 1.2024$, and the modulation frequency $\beta = 35$ fs, while the modulation phase ϕ is varied. A Fourier transform (FT) of these fields yields a pulse train in the temporal domain [e.g., see Fig. 4.10(a)]. In our studies we fix the (overall) peak intensity in the pulse train to $I_0 = 1 \times 10^{12}$ W/cm^2, which for the present frequencies is within the perturbation regime.

In the atomic case it was shown [95] that using $\phi = 0$ a dark pulse is formed and the final population in the excited state at the end of the pulse train vanishes. On the other hand the excitation probability was found to be maximized for pulse with $\phi = \pi/2$, which is therefore called a bright pulse. In contrast, we find that for the two-photon transition to a dissociative state in the present molecular model system that the final excitation probability is independent of the specific value of ϕ, as exemplified by the results for $\phi = 0$ (left column) and $\pi/2$ (right column) in Fig. 4.10.

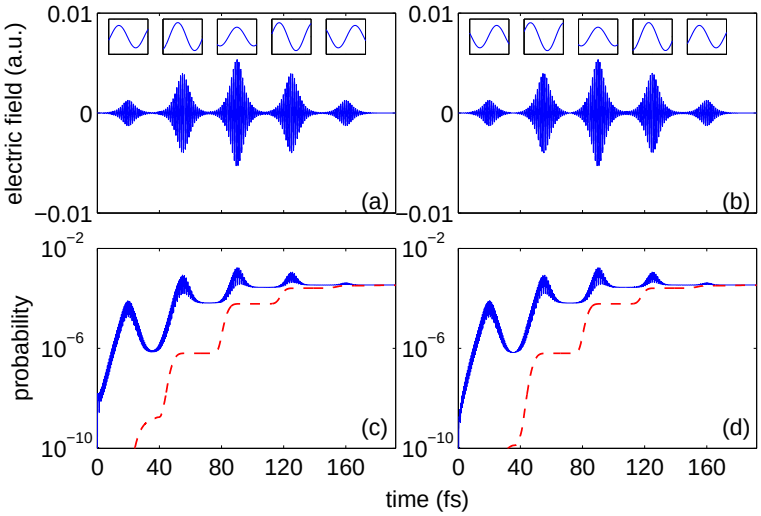

Figure 4.10: Two-photon coherent control of excitation to a dissociative molecular state. The upper panels show that the electric field distribution as a function of time [i.e., the Fourier transform of Eq. (4.14)] for (a) $\phi = 0$ and (b) $\phi = \pi/2$. The insets show the central field cycle and the carrier-envelope phase (CEP) of each subpulse. In the lower panels the time evolution of the probabilities in the first excited state (blue solid line) is presented for (c) $\phi = 0$ and (d) $\phi = \pi/2$. We also show the dissociation probabilities (red dashed lines).

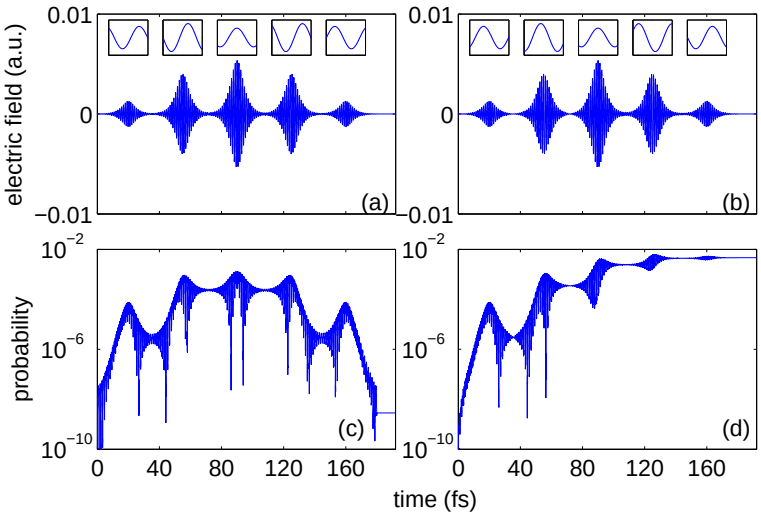

Figure 4.11: Same as Fig. 4.10, but for a molecular model system with fixed internuclear distance $R = R_0$.

The excitation probability increases stepwise as a function of time with the interaction of every subpulse in the train. Moreover, the final excitation probability is equal to the probability for dissociation at the end of the molecular model system (red dashed lines). This indicates it is the nuclear dynamics that causes the breakdown of the coherent control scheme.

In order to confirm this assumption, we perform another series of calculations in which we fixed the internuclear distance $R = R_0$ in Eq. (4.11) to suppress any nuclear dynamics but keep all other parameters unchanged except the central frequency $\omega/2 = 3.48$ eV. The central frequency is slightly increased since the ground state energy of the fixed nuclei model is lower than that of the 2D model. The results of the fixed nuclei model for $\phi = 0$ (Fig. 4.11, left column) and $\phi = \pi/2$ (Fig. 4.11, right column) agree with the findings for the atomic case. For $\phi = 0$ the final excited population is (close to) zero (dark pulse), while for $\phi = \pi/2$ the population is maximized (bright pulse). Thus, from the temporal analysis of the process we conclude that coherent control of the TPE to a dissociative molecular state using a train of pulses [or, a spectral phase modulated pulse of the form given in Eq. (4.14)] fails since each of the wave packets pumped to the excited state by the subpulses in the train quickly propagates to larger internuclear distances. Therefore, concerning the control of the total population in the excited (dissociative) state there is no signature of destructive nor constructive interferences between the wave packets generated from subsequent pulses.

4.3.4 Control of excitation to bound states

Next, we investigate the influence of nuclear dynamics on the control of two-photon excitations to bound molecular states. As shown above, this dynamics becomes effective for the present control scheme over the time delay between two subsequent pulses in a pulse train, since the fundamental control mechanism is based on the interference between two electronic wave packets induced by consecutive subpulses [106]. It is well known from studies in wave packet interferometry [107, 108] that, in the case of a two-pulse scenario, a control of the excitation probability can be achieved via the pulse delay τ and the relative phase ϕ_{rel} of the two pulses. For example, the

effective coherent control of the excitation of a superposition of two vibrational states requires

$$\tau = N\frac{2\pi}{E_{21} - E_{20}} = NT_{\text{revival}} \tag{4.15}$$

and varying ϕ_{rel}. Here, E_{2i} is the energy of the ith vibrational level of the second excited electronic state of our model. The pulse delays have to coincide with the multiples of the revival period T_{revival} of the vibrational wave packet created in the excited electronic state. This enables the control via efficient interference of wave packets generated by subsequent pulses, since the contributions in both vibrational levels of the second excited electronic state are in phase at these times.

The above analysis for the two-pulse sequence can be readily applied to the spectral phase modulated fields used by Silberberg and coworkers by noting that the modulation frequency β in Eq. (4.14) corresponds to the time delay τ between the consecutive subpulses in the train in the temporal domain. Furthermore, the relative phase ϕ_{rel} between the consecutive subpulses is determined by the modulation phase ϕ in Eq. (4.14). Thus, setting $\beta = NT_{\text{revival}}$ we expect to achieve an efficient control pattern by changing ϕ. To test our expectations, we do simulations by choosing $\alpha = 1.2024$, $\beta = 8T_{\text{revival}} = 85.6682$ fs, $\omega/2 = 5.83$ eV, $\Delta\omega = 0.1$ eV, and $I_0 = 1 \times 10^{11}$ W/cm^2. Note that we have chosen such a narrow bandwidth that only the lowest two vibrational levels of the second electronic state can be excited. The results of the simulations (circles and asterisks) for excitation to these two vibrational states as a function of the modulation phase ϕ are shown in Fig. 4.12. The same dependence of the two excitation probabilities on ϕ clearly confirms our expectations. We also show results calculated from the second-order perturbation theory (red dashed lines) in Fig. 4.12. Although the coefficient of the transition amplitude [94, 95] is not taken into account in our perturbation calculations, by normalizing the values from the perturbation theory to the maximum probability from the TDSE, we can see a good agreement of results from these two theories. The temporal analysis of the populations in the vibrational states (Fig. 4.13) clearly exhibits the destructive and constructive interference effects for the subsequent pulses in the train for the spectral phase modulation of a dark (left column) and a bright pulse (right column).

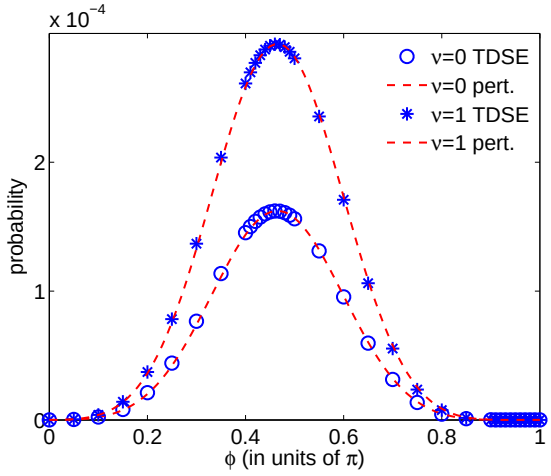

Figure 4.12: Excitation probabilities to the ground vibrational ($\nu_{2\mathrm{nd}} = 0$, circles and dashed line) and the first excited vibrational states ($\nu_{2\mathrm{nd}} = 1$, asterisks and dashed line) as functions of ϕ. A spectral phase modulated field defined in Eq. (4.14) is used with parameters: $\alpha = 1.2024$, $\beta = 8T_{\mathrm{revival}} = 85.6682$ fs, $\omega/2 = 5.83$ eV, $\Delta\omega = 0.1$ eV, and $I_0 = 1 \times 10^{11}$ W/cm^2. The symbols (circles and asterisks) are numerical results obtained by solving the TDSE, while the curves (dashed lines) are obtained using second-order perturbation theory.

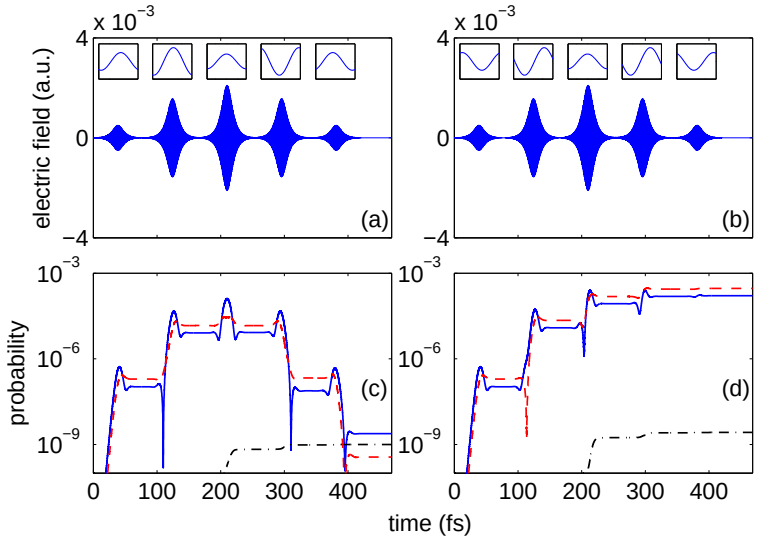

Figure 4.13: Two-photon coherent control of excitations to a superposition of two vibrational states. The upper panels show that the electric field distribution as a function of time [i.e., the Fourier transform of Eq. (4.14)] for (a) $\phi = 0.96\pi$ (dark pulse) and (b) $\phi = 0.46\pi$ (bright pulse). The insets show the central field cycle and the CEP of each subpulse. In the lower panels the time evolution of the probabilities in the ground (blue solid line) and first excited (red dashed line) vibrational state is presented for the (c) dark and (d) bright pulses, respectively. Also shown is the ionization probability (black dashed-dotted line).

Chapter 5

Conclusions

In this thesis we have systematically studied the attosecond time delays in single- and two-photon ionization using theoretical analyses and numerical simulations. For single-photon ionization (SPI) we have developed a new numerical method to calculate the Wigner-Smith-like time delay from a time-dependent perspective and proposed an alternative interpretation for the time delay measured in the streaking experiment. This new interpretation provides a deeper understanding of the attosecond streaking technique and thus allows us to use it to study other ultrafast processes such as the two-photon ionization (TPI) process.

In Chapter 2, we reviewed the numerical model and method used to describe laser-matter interaction. We first reviewed the single-active-electron model, in which only one electron in a multi-electron system is treated as active to reduce costs in numerical simulations. We then presented our numerical approaches to solving the TDSE, including the methods of obtaining initial field-free states, propagating the wave function in time domain, and working with different absorbing boundary conditions.

We carefully studied time delays in SPI in Chapter 3. This chapter consists of two major aspects: On the one hand, we calculated the WS time delay for SPI from its fundamental definition using a new time-dependent method. Such a method provides a time-dependent analysis of the photoionization process and is more general for different potentials than the previous time-independent definition. On the other hand, we investigated the time delay measured in SPI using the attosecond streaking technique and proposed a new interpretation of such a measurement. Our

new interpretation suggests that the streaking time delay arises from the measurement, i.e., the propagation of the electron in the coupled field of the streaking pulse and the ionic potential after the absorption of the photon, and thus can be calculated using classical mechanics. The streaking time delay can be further understood as the sum of piecewise field-free time delays weighted by the relative instantaneous streaking field and only relates to a finite-range part of the ionic potential. The latter finite-range property allows us to use the attosecond streaking technique as an imaging tool.

We further extended our studies to present results on time resolving the TPI process in Chapter 4. Based on our understanding of time delays in SPI, in particular, the new interpretation for the streaking time delay, we are able to make use of the streaking technique to retrieve the time delay of two-photon absorption with respect to the center of the XUV pulse. By accounting for the propagation time delay obtained from classical simulations, we could retrieve the absorption time delay from the streaking time delay extracted from the streaking trace. Our results reveal that the streaking time delay is zero for nonresonant TPI, but it is nonzero and changes linearly with the XUV pulse duration for resonant TPI. We further confirmed our findings using two other independent methods: the trajectory analysis based on quantum simulations and the phase analysis using second-order perturbation theory. Since the TPI time delay results may be further applied to control the later dynamics followed by the photoionization process, we took the opportunity here to review our previous work on coherent control of two-photon excitations in molecular model systems.

Bibliography

[1] F. Krausz and M. Ivanov. Review of Modern Physics, 81:163–234, 2009.

[2] A. L. Cavalieri, N. Muller, T. Uphues, V. S. Yakovlev, A. Baltuska, B. Horvath, B. Schmidt, L. Blumel, R. Holzwarth, S. Hendel, M. Drescher, U. Kleineberg, P. M. Echenique, R. Kienberger, F. Krausz, and U. Heinzmann. Nature, 449:1029–1032, 2007.

[3] M. Schultze, M. Fiess, N. Karpowicz, J. Gagnon, M. Korbman, M. Hofstetter, S. Neppl, A. L. Cavalieri, Y. Komninos, T. Mercouris, C. A. Nicolaides, R. Pazourek, S. Nagele, J. Feist, J. Burgdörfer, A. M. Azzeer, R. Ernstorfer, R. Kienberger, U. Kleineberg, E. Goulielmakis, F. Krausz, and V. S. Yakovlev. Science, 328:1658–1662, 2010.

[4] K. Klünder, J. M. Dahlström, M. Gisselbrecht, T. Fordell, M. Swoboda, D. Guenot, P. Johnsson, J. Caillat, J. Mauritsson, A. Maquet, R. Taïeb, and A. L'Huillier. Physical Review Letters, 106:143002, 2011.

[5] M. Uiberacker, Th. Uphues, M. Schultze, A. J. Verhoef, V. Yakovlev, M. F. Kling, J. Rauschenberger, N. M. Kabachnik, H. Schröder, M. Lezius, K. L. Kompa, H.-G. Muller, M. J. J. Vrakking, S. Hendel, U. Kleineberg, U. Heinzmann, M. Drescher, and F. Krausz. Nature, 446:627–632, 2007.

[6] P. Eckle, A. N. Pfeiffer, C. Cirelli, A. Staudte, R. Dörner, H. G. Muller, M. Büttiker, and U. Keller. Science, 322:1525–1529, 2008.

[7] F. Remacle and R. D. Levine. Proceedings of the National Academy of Sciences of the United States of America, 103:6793–6798, 2006.

[8] P. B. Corkum and F. Krausz. Nature Physics, 3:381–387, 2007.

[9] L. Gallmann, C. Cirelli, and U. Keller. Annual Review of Physical Chemistry, 63:447–469, 2012.

[10] M. Ferray, A. L'Huillier, X. F. Li, L. A. Lompre, G. Mainfray, and C. Manus. Journal of Physics B, 21:L31–L35, 1988.

[11] A. McPherson, G. Gibson, H. Jara, U. Johann, T. S. Luk, I. A. McIntyre, K. Boyer, and C. K. Rhodes. Journal of the Optical Society of America B, 4:595–601, 1987.

[12] J. L. Krause, K. J. Schafer, and K. C. Kulander. Physical Review A, 45:4998–5010, 1992.

[13] J. L. Krause, K. J. Schafer, and K. C. Kulander. Physical Review Letters, 68:3535–3538, 1992.

[14] P. B. Corkum. Physical Review Letters, 71:1994–1997, 1993.

[15] M. Lewenstein, Ph. Balcou, M. Y. Ivanov, A. L'Huillier, and P. B. Corkum. Physical Review A, 49:2117–2132, 1994.

[16] I. P. Christov, J. Zhou, J. Peatross, A. Rundquist, M. M. Murnane, and H. C. Kapteyn. Physical Review Letters, 77:1743–1746, 1996.

[17] J. Zhou, J. Peatross, M. M. Murnane, H. C. Kapteyn, and I. P. Christov. Physical Review Letters, 76:752–755, 1996.

[18] I. P. Christov, M. M. Murnane, and H. C. Kapteyn. Physical Review Letters, 78:1251–1254, 1997.

[19] T. Popmintchev, M.-C. Chen, P. Arpin, M. M. Murnane, and H. C. Kapteyn. Nature Photonics, 4:822–832, 2010.

[20] T. Popmintchev, M.-C. Chen, D. Popmintchev, P. Arpin, S. Brown, S. Ališauskas, G. Andriukaitis, T. Balčiunas, O. D. Mcke, A. Pugzlys, A. Baltuška, B. Shim, S. E. Schrauth, A. Gaeta, C. Hernández-García, L. Plaja, A. Becker, A. Jaroń-Becker, M. M. Murnane, and H. C. Kapteyn. Science, 336:1287–1291, 2012.

[21] V. S. Yakovlev and A. Scrinzi. Physical Review Letters, 91:153901, 2003.

[22] M. Chini, K. Zhao, and Z. Chang. Nature Photonics, 8:178–186, 2014.

[23] M. Hentschel, R. Kienberger, Ch. Spielmann, G. A. Reider, N. Milosevic, T. Brabec, P. Corkum, U. Heinzmann, M. Drescher, and F. Krausz. Nature, 414:509–513, 2001.

[24] E. Goulielmakis, M. Schultze, M. Hofstetter, V. S. Yakovlev, J. Gagnon, M. Uiberacker, A. L. Aquila, E. M. Gullikson, D. T. Attwood, R. Kienberger, F. Krausz, and U. Kleineberg. Science, 320:1614–1617, 2008.

[25] M.-C. Chen, C. Hernández-García, C. Mancuso, F. Dollar, B. Galloway, D. Popmintchev, P.-C. Huang, B. Walker, L. Plaja, A. Jaroń-Becker, A. Becker, T. Popmintchev, M. M. Murnane, and H. C. Kapteyn. Arxiv, http://arxiv.org/abs/1401.0240v1, 2014.

[26] J. A. Armstrong, N. Bloembergen, J. Ducuing, and P. S. Pershan. Physical Review, 127:1918–1939, 1962.

[27] A. Rundquist, C. G. Durfee, Z. Chang, C. Herne, S. Backus, M. M. Murnane, and H. C. Kapteyn. Science, 280:1412–1415, 1998.

[28] C. G. Durfee, A. R. Rundquist, S. Backus, C. Herne, M. M. Murnane, and H. C. Kapteyn. Physical Review Letters, 83:2187–2190, 1999.

[29] E. Constant, D. Garzella, P. Breger, E. Mével, Ch. Dorrer, C. Le Blanc, F. Salin, and P. Agostini. Physical Review Letters, 82:1668–1671, 1999.

[30] T. Popmintchev, M.-C. Chen, A. Bahabad, M. Gerrity, P. Sidorenko, O. Cohen, I. P. Christov, M. M. Murnane, and H. C. Kapteyn. Proceedings of the National Academy of Sciences, 106:10516–10521, 2009.

[31] M. Uiberacker and F. Krausz. SPIE's oemagazine, May:18–22, 2004.

[32] M. Ya. Schelev, M. C. Richardson, and A. J. Alcock. Applied Physics Letters, 18:354–357, 1971.

[33] D. J. Bradley, B. Liddy, and W. E. Sleat. Optics Communications, 2:391–395, 1971.

[34] J. Itatani, F. Quéré, G. L. Yudin, M. Y. Ivanov, F. Krausz, and P. B. Corkum. Physical Review Letter, 88:173903, 2002.

[35] M. Kitzler, N. Milosevic, A. Scrinzi, F. Krausz, and T. Brabec. Physical Review Letters, 88:173904, 2002.

[36] M. Drescher, M. Hentschel, R. Kienberger, G. Tempea, Ch. Spielmann, G. A. Reider, P. B. Corkum, and F. Krausz. Science, 291:1923–1927, 2001.

[37] S. Nagele, R. Pazourek, J. Feist, K. Doblhoff-Dier, C. Lemell, K. Tökési, and J. Burgdörfer. Journal of Physics B, 44:081001, 2011.

[38] M. Ivanov and O. Smirnova. Physical Review Letters, 107:213605, 2011.

[39] C. H. Zhang and U. Thumm. Physical Review A, 82:043405, 2010.

[40] E. P. Wigner. Physical Review, 98:145–147, 1955.

[41] F. T. Smith. Physical Review, 118:349–356, 1960.

[42] J. Su, H. Ni, A. Becker, and A. Jaroń-Becker. Physical Review A, 87:033420, 2013.

[43] J. Su, H. Ni, A. Becker, and A. Jaroń-Becker. Journal of Morden Optics, 60:1484–1491, 2013.

[44] A. S. Kheifets and I. A. Ivanov. Physical Review Letter, 105:233002, 2010.

[45] A. S. Kheifets, I. A. Ivanov, and I. Bray. Journal of Physics B, 44:101003, 2011.

[46] I. A. Ivanov. Physical Review A, 83:023421, 2011.

[47] I. A. Ivanov. Physical Review A, 86:023419, 2012.

[48] I. A. Ivanov, A. S. Kheifets, and V. V. Serov. Physical Review A, 86:063422, 2012.

[49] A. S. Kheifets. Physical Review A, 87:063404, 2013.

[50] V. V. Serov, V. L. Derbov, and T. A. Sergeeva. Physical Review A, 87:063414, 2013.

[51] G. Dixit, H. S. Chakraborty, and M. E. Madjet. Physical Review Letters, 111:203003, 2013.

[52] C. H. Zhang and U. Thumm. Physical Review A, 84:033401, 2011.

[53] S. Nagele, R. Pazourek, J. Feist, and J. Burgdörfer. Physical Review A, 85:033401, 2012.

[54] J. C. Baggesen and L. B. Madsen. Physical Review Letters, 104:043602, 2010.

[55] L. R. Moore, M. A. Lysaght, J. S. Parker, H. W. van der Hart, and K. T. Taylor. Physical Review A, 84:061404, 2011.

[56] R. Pazourek, J. Feist, S. Nagele, and J. Burgdörfer. Physical Review Letters, 108:163001, 2012.

[57] D. Guénot, K. Klünder, C. L. Arnold, D. Kroon, J. M. Dahlström, M. Miranda, T. Fordell, M. Gisselbrecht, P. Johnsson, J. Mauritsson, E. Lindroth, A. Maquet, R. Taïeb, A. L'Huillier, and A. S. Kheifets. Physical Review A, 85:053424, 2012.

[58] J. M. Dahlström, A. L'Huillier, and A. Maquet. Journal of Physics B, 45:183001, 2012.

[59] J. M. Dahlström, D. Guenot, K. Klünder, M. Gisselbrecht, J. Mauritsson, A. L'Huillier, A. Maquet, and R. Taïeb. Chemical Physics, 414:53–64, 2013.

[60] M. Cardona and L. Ley. Photoemission in Solids I: General Principles. Springer-Verlag, Berlin, 1978.

[61] E. Clementi and C. Roetti. Atomic Data and Nuclear Data Tables, 14:177–478, 1974.

[62] J. J. Yeh and I. Lindau. Atomic Data and Nuclear Data Tables, 32:1–155, 1985.

[63] I. N. Levine. Quantum Chemsitry. Prentice Hall, 2000.

[64] J. P. Perdew and A. Zunger. Physical Review B, 23:5048–5079, 1981.

[65] J. B. Krieger, Y. Li, and G. J. Iafrate. Physical Review A, 45:101–126, 1992.

[66] Y. Li, J. B. Krieger, and G. J. Iafrate. Physical Review A, 47:165–181, 1993.

[67] J. Chen, J. B. Krieger, Y. Li, and G. J. Iafrate. Physical Review A, 54:3939–3947, 1996.

[68] R. T. Sharp and G. K. Horton. Physical Review, 90:317–340, 1953.

[69] J. D. Talman and W. F. Shadwick. Physical Review A, 14:36–40, 1976.

[70] X. M. Tong and S. I. Chu. Physical Review A, 55:3406–3416, 1997.

[71] X. M. Tong and C. D. Lin. Journal of Physics B, 38:2593–2600, 2005.

[72] J. Crank and P. Nicolson. Advances in Computational Mathematics, 6:207–226, 1996.

[73] O. A. Sharafeddin, D. J. Kouri, and D. K. Hoffman. Canadian Journal of Chemistry, 70:686–692, 1992.

[74] B. C. Hall. Lie Groups, Lie Algebras, and Representations. Springer New York, 2003.

[75] M. D. Feit, J. A. Fleck Jr., and A. Steiger. Journal of Computational Physics, 47:412–433, 1982.

[76] F. He, C. Ruiz, and A. Becker. Physical Review A, 75:053407, 2007.

[77] C. A. A. de Carvalhoa and H. M. Nussenzveig. Physics Reports, 364:83–174, 2002.

[78] R. G. Newton. Scattering Theory of Waves and Particles. Springer-Verlag, New York, 1982.

[79] J. Itatani, J. Levesque, D. Zeidler, Hiromichi Niikura, H. Ppin, J. C. Kieffer, P. B. Corkum, and D. M. Villeneuve. Nature, 432:867–871, 2004.

[80] S. N. Yurchenko, S. Patchkovskii, I. V. Litvinyuk, P. B. Corkum, and G. L. Yudin. Physical Review Letters, 93:223003, 2004.

[81] J. Su, H. Ni, A. Becker, and A. Jaroń-Becker. Physical Review A, 88:023413, 2013.

[82] P. B. Corkum. Physical Review Letters, 71:1994–1998, 1993.

[83] O. Smirnova, A. S. Mouritzen, S. Patchkovskii, and M. Ivanov. Journal of Physics B, 40:F197–F206, 2007.

[84] O. Smirnova, M. Spanner, and M. Ivanov. Journal of Physics B, 39:S307–S321, 2006.

[85] J. Su, H. Ni, A. Becker, and A. Jaroń-Becker. Physical Review A, 89:013404, 2014.

[86] J. Su, H. Ni, A. Becker, and A. Jaroń-Becker. Chinese Journal of Physics, 52:404–415, 2014.

[87] Y. Nabekawa, T. Shimizu, T. Okino, K. Furusawa, H. Hasegawa, K. Yamanouchi, and K. Midorikawa. Physical Review Letters, 97:153904, 2006.

[88] L. H. Haber, B. Doughty, and S. R. Leone. Physical Review A, 79:031401, 2009.

[89] K. L. Ishikawa and K. Ueda. Physical Review Letters, 108:033003, 2012.

[90] R. Moshammer, Th. Pfeifer, A. Rudenko, Y. H. Jiang, L. Foucar, M. Kurka, K. U. Kühnel, C. D. Schröter, J. Ullrich, O. Herrwerth, M. F. Kling, X.-J. Liu, K. Motomura, H. Fukuzawa, A. Yamada, K. Ueda, K. L. Ishikawa, K. Nagaya, H. Iwayama, A. Sugishima, Y. Mizoguchi, S. Yase, M. Yao, N. Saito, A. Belkacem, M. Nagasono, A. Higashiya, M. Yabashi, T. Ishikawa, H. Ohashi, H. Kimura, and T. Togashi. Optics Express, 19:21698–21706, 2011.

[91] J. Su, H. Ni, A. Jaroń-Becker, and A. Becker. *Time Delays in Two-Photon Ionization.* submitted.

[92] R. Pazourek, S. Nagele, and J. Burgdörfer. Faraday Discussions, 163:353–376, 2013.

[93] C. W. Clark. American Journal of Physics, 47:683–684, 1979.

[94] D. Meshulach and Y. Silberberg. Nature, 396:239–242, 1998.

[95] D. Meshulach and Y. Silberberg. Physical Review A, 60:1287–1292, 1999.

[96] J. Su, S. H. Chen, A. Jaroń-Becker, and A. Becker. Physical Review A, 84:065402, 2011.

[97] P. Brumer and M. Shapiro. Chemical Physics Letters, 126:541–550, 1986.

[98] D. J. Tannor and S. A. Rice. Journal of Chemical Physics, 83:5013–5018, 1985.

[99] D. J. Tannor, R. Kosloff, and S. A. Rice. Journal of Chemical Physics, 85:5805–5820, 1986.

[100] S. A. Rice and M. Zhao. Optical Control of Molecular Dynamics. Wiley-Interscience, New York, 2000.

[101] A. M. Weiner. Optics Communication, 284:3669–3692, 2011.

[102] N. Dudovich, B. Dayan, S. M. Gallagher Faeder, and Y. Silberberg. Physical Review Letters, 86:47–50, 2001.

[103] P. Panek and A. Becker. Physical Review A, 74:023408, 2006.

[104] A. Gandman, L. Chuntonov, L. Rybak, and Z. Amitay. Physical Review A, 75:031401, 2007.

[105] T. Bayer, M. Wollenhaupt, C. Sarpe-Tudoran, and T. Baumert. Physical Review Letters, 102:023004, 2009.

[106] S. H. Chen, A. Jaroń-Becker, and A. Becker. Physical Review A, 82:013414, 2010.

[107] M. M. Salour and C. Cohen-Tannoudji. Physical Review Letters, 38:757–760, 1977.

[108] R. Teets, J. Eckstein, and T. W. Hansch. Physical Review Letters, 38:760–764, 1977.